# INFORMATION TO USERS

This manuscript has been reproduced from the microfilm master. UMI films the text directly from the original or copy submitted. Thus, some thesis and dissertation copies are in typewriter face, while others may be from any type of computer printer.

**The quality of this reproduction is dependent upon the quality of the copy submitted.** Broken or indistinct print, colored or poor quality illustrations and photographs, print bleedthrough, substandard margins, and improper alignment can adversely affect reproduction.

In the unlikely event that the author did not send UMI a complete manuscript and there are missing pages, these will be noted. Also, if unauthorized copyright material had to be removed, a note will indicate the deletion.

Oversize materials (e.g., maps, drawings, charts) are reproduced by sectioning the original, beginning at the upper left-hand corner and continuing from left to right in equal sections with small overlaps. Each original is also photographed in one exposure and is included in reduced form at the back of the book.

Photographs included in the original manuscript have been reproduced xerographically in this copy. Higher quality 6" x 9" black and white photographic prints are available for any photographs or illustrations appearing in this copy for an additional charge. Contact UMI directly to order.

**UMI**

A Bell & Howell Information Company
300 North Zeeb Road, Ann Arbor MI 48106-1346 USA
313/761-4700 800/521-0600

NORTHWESTERN UNIVERSITY

# Gold Induced Si(111) Surface Reconstructions Studied by Ultrahigh Vacuum Transmission Electron Microscopy

A DISSERTATION

SUBMITTED TO THE GRADUATE SCHOOL

IN PARTIAL FULFILLMENT OF THE REQUIREMENTS

for the degree

DOCTOR OF PHILOSOPHY

Field of Materials Science and Engineering

by

Richard Anton Plass, "R. A."

EVANSTON, ILLINOIS "Ph. D."

June 1996

# ABSTRACT

## Gold Induced Si(111) Surface Reconstructions Studied by Ultrahigh Vacuum Transmission Electron Microscopy

Richard Anton Plass

Due to its growing scientific and technical importance in semiconductor metallization, the Au on Si(111) system has recently drawn the attention of many researchers. Therefore, the atomic structures of two gold induced Si(111) surface reconstructions were determined using ultrahigh vacuum transmission electron microscopy.

The Si(111)-(5x2) Au atomic structure was determined using a combination of off-zone HREM imaging, "heavy-atom holography", and $\chi^2$ electron diffraction refinement. It contains two rows of gold atoms between expanded surface arrangements of silicon atoms. Si(111)-(5x2) Au passivates the surface to oxygen attack and room temperature gold deposition onto it indicates surface diffusion is important in its disordering.

Transmission electron diffraction data of the Si(111)-($\sqrt{3}$x$\sqrt{3}$)R30°Au surface support the missing top layer twisted trimer model of this surface in which gold and silicon atoms in the top two layers form rotated like-atom trimers. This gold-silicon

structure is quite similar to part of the Si(111)-(5x2) Au structure. The degree of trimer rotation and the interatomic spacings of the Si(111)-($\sqrt{3}$x$\sqrt{3}$)R30°Au structure vary significantly with the sharpness of the structure's diffraction spots. These variations and large fitted Debye Waller term values indicate substantial static disorder is present. Evidence of subsurface displacements and charge transfer was also found. The presence of gold trimers is confirmed by the local symmetry seen in high resolution micrographs, which also show surface domain morphology differences between diffuse and sharp diffraction spot regions. Based on these images, models for the Si(111)-($\sqrt{3}$x$\sqrt{3}$)R30°Au domain walls are proposed.

Room temperature gold deposition onto the Si(111)-($\sqrt{3}$x$\sqrt{3}$)R30°Au surface shows that higher order surface diffracted beams decay more quickly with coverage than lower order beams. Direct phasing analysis of this result indicates deposited gold occupies unstable $T_4$ like honeycomb sites within the structure. The site could play a key role in the disordering of the Si(111)-($\sqrt{3}$x$\sqrt{3}$)R30° Au surface.

Finally a partial surface phase diagram and driving forces are proposed for the Au on Si(111) system based on these and other literature results.

---

Professor Laurence D. Marks

Department of Materials Science and Engineering

Northwestern University, Evanston IL 60208

# DEDICATION

To my family: past, present, and future, especially to my father, George, whose examples of hard work, self-discipline, self-giving, and dedication to his family were truly heroic.

# ACKNOWLEDGMENTS

First and foremost I want to thank the Big Guy for granting me the first glimpse of the small niche of this world He created which is described in these pages, and for giving me the wits to figure out what I was looking at! Thanks to my family who has had to put up with a lot these last six years. Thanks also to all my friends at NU, especially the guys at the NUC, for helping me stay on an even keel, and my instructors at De Paul University for good preparation.

Not enough thanks can be given to my advisor, Professor Laurence D. Marks. He has been an outstanding instructor and mentor for six years and a true scientific colleague for four, but he has also changed for the better in numerous ways since I first joined the group. I also thank him for his dogged two-year pursuit of the Si(111)-(5x2) Au atomic structure which I doubt I alone would have been able to solve, and yet is a pivotal result of this thesis.

Among my coworkers I first want to thank Dr. Doraiswamy Narayanswamy for sharing crazy dreams, lofty ambitions, advice about a million subjects, and all around good times, (and more than a couple not so good times). Thanks to Dr. Jin Ping (microscopy god) Zhang, Dr. Hong Zhang (VPD group), Dr. Derren Dunn, Scott Savage and all my seniors in the LDM group for sharing their knowledge and for their incredible patience with me. Thanks to my brothers in arms, Dr. Ganesh Jayaram, Dr. Boris Vuchic, and Dr. V. Ravikumar for shared knowledge and camaraderie. Thanks

also to Bradford Storey III and Dr. Hong Zhang (LDM group) for their often unsolicited assistance and thanks to the little people: Chris Collazo, Dan Grozea, and Eric Landree, for putting up with my reign of terror and for their numerous, at times awe inspiring, examples of teamwork.

I'd also like to thank Professor Vinayak P. Dravid and Professor Jun Nogami for the numerous fruitful discussions we have had and Dr. J. Yuhara, Dr. D. O'Mahony, Dr. K. Yagi, Dr. A. Ichimiya, Dr. H. Saka, Dr. M. Gothlied and several other colleagues in the field for stimulating discussions and the literature they have provided (especially to Junji and Des for providing copies of their theses). Thanks to Rob Lukaszewski in the glass shop, Rich Benassi, Ken (instrument maker extraordinare) Lehman and the guys in the instrument shop, and Bob Passeri and all the MSE technicians, past and present.

# LIST OF ABBREVIATIONS

| | |
|---|---|
| 1x1 | Quenched metastable Si(111)-(1x1), unless otherwise noted |
| 2x1 | Metastable Si(111)-(2x1) |
| 3x1 Ag | Si(111)-(3x1) Ag |
| √3 Au | Si(111)-(√3x√3)R30° Au |
| √3 Ag | Si(111)-(√3x√3)R30° Ag |
| 5x2 Au | Si(111)-(5x2) Au |
| 5x3 Au | Si(100)-(5x3) Au |
| 6x6 Au | Si(111)-(6x6) Au |
| 7x7 | Si(111)-(7x7) |
| | |
| AES | Auger Electron Spectroscopy |
| AFM | Atomic Force Microscopy |
| CTF | Contrast Transfer Function |
| DAS | Dimer Adatom Stacking fault (model) |
| DW | Debye Waller (term) |
| HC | Honeycomb (site) |
| HREM | High Resolution Electron Microscopy |
| ICISS | Impact-Collision Ion Scattering Spectroscopy |
| ISS | Ion Scattering Spectroscopy |
| LEED | Low Energy Electron Diffraction |
| LEEM | Low Energy Electron Microscopy |
| PEELS | Parallel Electron Energy Loss Spectroscopy |
| RC | Ring Cluster (structure) |
| RBS | Rutherford Backscattering Spectroscopy |
| REM | Reflection Electron Microscopy |
| RGA | Residual Gas Analyzer |
| RHEED | Reflection High Energy Electron Diffraction |
| SEM | Scanning Electron Microscopy |
| SK | Stranski Krastanov (growth mode) |
| SPEAR | Sample Preparation Evaluation Analysis Reaction (chamber) |
| STEM | Scanning Transmission Electron Microscopy |
| STM | Scanning Tunneling Microscopy |
| TED | Transmission Electron Diffraction |
| TEM | Transmission Electron Microscopy |
| UHV | Ultrahigh Vacuum |
| VW | Volmer Weber (growth mode) |
| XPS | X-ray Photoelectron Spectroscopy |
| XRD | X-ray Diffraction |
| XSW | X-ray Standing Wave (technique) |

# TABLE OF CONTENTS

# LIST OF FIGURES

# LIST OF TABLES

# 1 INTRODUCTION

## 1.1 Semiconductor Metallization

Ever since the invention of the transistor by W. H. Brattain and J. Bardeen of Bell Laboratories in 1947 (Morris 1990), semiconductor based electronic devices have played an ever increasing role in our society and in our lives, as is evident from the sales trends of electronic equipment and devices shown in Figure 1.1 (Valentine 1995). Partially responsible for this astonishing growth of the semiconductor industry has been the steady increase in the complexity of semiconductor devices since their invention, known as Moore's Law (Hazewindus and Tooker 1982, Morris 1990). In the early 1960's Fairchild Electronics industrialist G. E. Moore predicted that the number of components per integrated circuit would double every two years. This prediction, made when there were tens of components per integrated circuit, has turned out to be surprisingly accurate for almost three and a half decades. Recently it took about three years for Intel to double the transistor count of the 486 microprocessor to the Pentium's 3.1 million transistors. As component prices

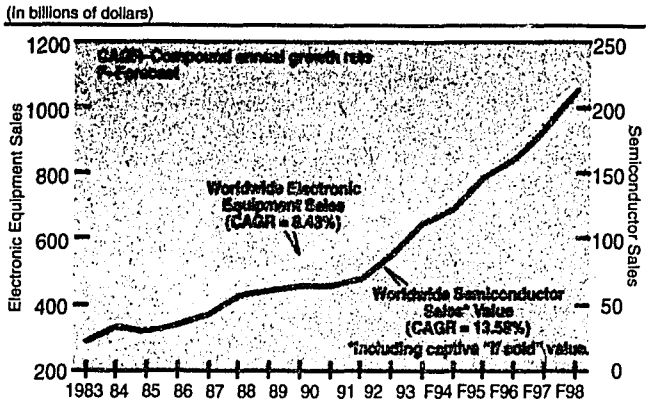


Figure 1.1. Plot of worldwide electronic equipment and device sales trends (after Valentine 1995).

have remained relatively constant (in terms of true purchasing power), during this time the price per device function has steadily decreased making any device that use microelectronic components ever more affordable.

Several factors contribute to the increasing complexity of electronic components characterized by Moore's Law (Hazewindus and Tooker 1982), the most important for the present study being the steady improvement in device fabrication design rules to make ever narrower minimum device features, currently 0.35 microns in state-of-the-art devices. To maintain this steady decrease in minimum feature size, as well as to plan other device improvements, the semiconductor industry as a whole is planning future technological progress through the Semiconductor Industry Association's National Technology Roadmap for Semiconductors (Burger et al. 1995). The 1995 Roadmap represents the industry's goals and guidelines for meeting the projected technological needs of the global semiconductor market through the year 2010.

In addition to specifying several projected RAM and microprocessor parameters of the future, the Roadmap's key parameter for the present study is the minimum chip feature size (Figure 1.2), which it projects will be 70 nm by the year 2010. This value is only tens of typical surface unit cells across yet is expected to be achieved reliably in device fabrication plants only 14 years from now. I would emphasis that this is not a number projected by some futurist but a specific goal of the entire semiconductor industry.

While our understanding of the surface science of key atomic structures and

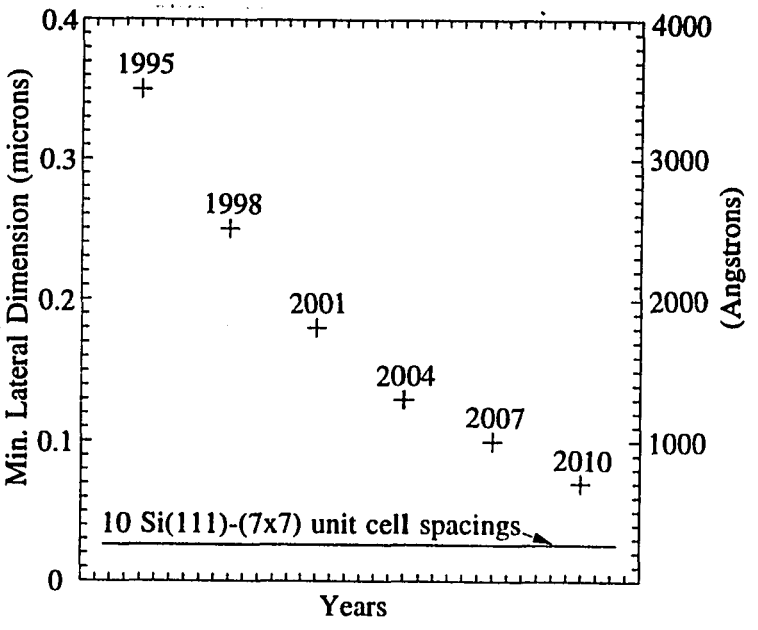


Figure 1.2. Semiconductor industry association Roadmap minimum lateral device dimensions through 2010 (after Burger et al. 1995).

processes related to semiconductor device fabrication has been increasing rapidly in the last few years, as is evident from the already large and growing body of literature on the subject, we are not currently in a position to meet the minimum device dimension goal specified by the Roadmap. For example, while the native silicon reconstructions on the (100) and (111) surfaces have been determined conclusively (Jayaram, Xu, and Marks 1995, Twesten and Gibson 1995), the driving forces behind the more complicated Si(111)-(7x7) reconstruction are still a matter of debate (Qian and Chadi 1987, Robinson et al. 1988, Vanderbilt 1987a). In the vital process of semiconductor metallization, the atomic structures of many metal induced surface reconstruction are still not known conclusively, much less their driving forces, and plan view atomistic study of semiconductor / metal interfaces is in its infancy (Kasier and Bell 1988, Kimura and Takayanagi 1992). Without a detailed knowledge of the driving forces of these atomic structures, developing future device design recipes will be next to impossible. Problems such as electromigration will need to be understood

and controlled at the atomic scale for such small device dimensions, requiring not just a detailed knowledge of the atomic structures but also a detailed knowledge of the energetics that create the structure.

Also, as is evident from the interesting work being done on quantum size devices (e.g., Weisbuch 1991), a detailed knowledge of nanometer scale atomic structures and their associated electron orbital structures can provide a wealth of new device types if they can be fabricated reliably. Thus the Roadmap's goals may be exceeded.

The approach of materials science in improving the performance of materials will prove quite useful in the achievement of the semiconductor industry's goals. This approach is to:

1) characterize a starting material structurally and chemically,

2) develop an understanding of the microstructure of the material,

3) determine what microscopic properties are key to the macroscopic property in question and propose a model to improve these properties and,

4) prepare an improved material based on this model.

The first two steps of this approach have been implemented in the present study to determine the processes and microstructures involved in the early stages of gold metallization of silicon (111).

## 1.2 Choice of the Material to Study

One may wonder why should gold metallization of silicon be studied in depth

since the fast diffusion of gold into silicon and its formation of deep traps in the electronic band structure severely limit gold's use as a contact material (Milnes 1973). In this regard it is interesting to note the growing debate with regard to the use of copper rather than aluminum in semiconductor device vias for immediate device applications (e.g. Murarka and 1995), and the associated care needed in constructing barriers to copper diffusion. But the types of future devices for which this study was done will require all the atoms of a structure to be strongly bound. If the active region of a device is only 70 nm wide, the electronic disruptions associated with the loss of just a couple atoms from the structure can degrade the device's performance by at least a few percent, enough to cause failure. Hence, we can see this research aims at a much higher level of device reliability for which fundamental scientific understanding is more important than current device design rules.

With this in mind we should, in principle, look into the entire metallic periodic table to fully understand the nature of metal bonding to silicon (111). While substantial, interesting research has been done by depositing just about every readily available metal onto Si(111) a comprehensive review of all this literature does not yet exist and falls far outside the scope of this text. Instead I will briefly discuss the metal induced reconstructions of the near noble transition metals on Si(111) to provide a scientific "backdrop" for the unique behavior of the noble metals on Si(111).

### *1.2.1 Transition Metals on Si(111)*

The most common metal induced reconstruction across the periodic table is the

ring cluster (RC) structure formed when several transition metals are deposited onto Si(111) (Parikh, Lee, and Bennett 1995 and references therein). (The common $\sqrt{3}x\sqrt{3}$ type metal induced reconstruction can come from a surprisingly large variety of fundamentally different surface structures.) The RC structure, shown in Figure 1.3, bears a striking resemblance to the metal atom's coordination in $NiSi_2$, as well as having interesting dynamics. Careful temperature and Ni on Si(111) coverage low energy electron microscopy (LEEM) studies of the appearance of ordered ($\sqrt{7}x\sqrt{7}$-RC) and disordered (1x1-RC) arrangements of the RC structure show a eutectic relation between the phases (Bennett et al. 1995). The study of the ring cluster structure is of growing importance in the semiconductor field owing to the conductivity of the transition metal silicides. Of even more interest scientifically, though, are the noble metals. The noble metals display a large variety of metal induced surface reconstructions with temperature and coverage. If we can understand these more complex systems we will have a better understanding of simpler systems.

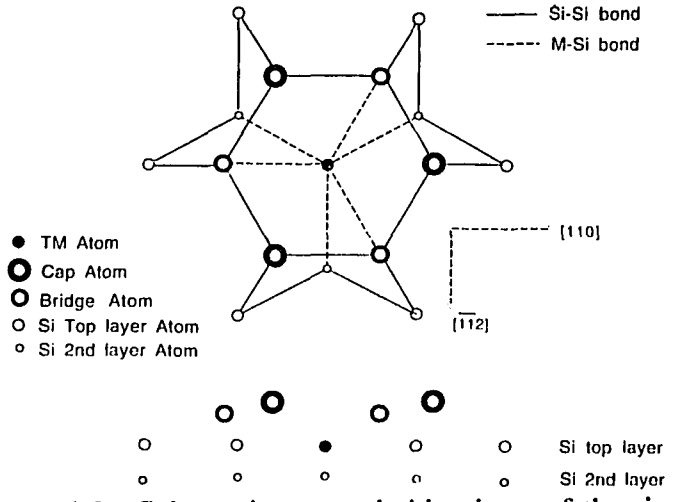


Figure 1.3. Schematic top and side views of the ring cluster structure common to transition and near noble metals on Si(111) (after Parikh, Lee, and Bennett 1995).

### *1.2.2 Noble Metals on Si(111)*

The metals which display the largest variety of surface structures are the noble metals: Cu, Ag, and especially Au. These metals do not fit the "pattern" of many transition metals in forming ring clusters.

Copper on silicon forms an incommensurate Si(111)-(5x5) structure (Koshikawa et al. 1995 and references therein), incommensurate in that the surface unit cell is about 5.5 Si(111) 1x1 surface unit cells across. The structure appears to consist of copper atoms packing on an ideally terminated 1x1 surface (see Section 3.1) indicating weak bonding between copper and silicon atoms at the surface despite the fact that several copper silicides exist. But much more work needs to be done on this system to fully understand it.

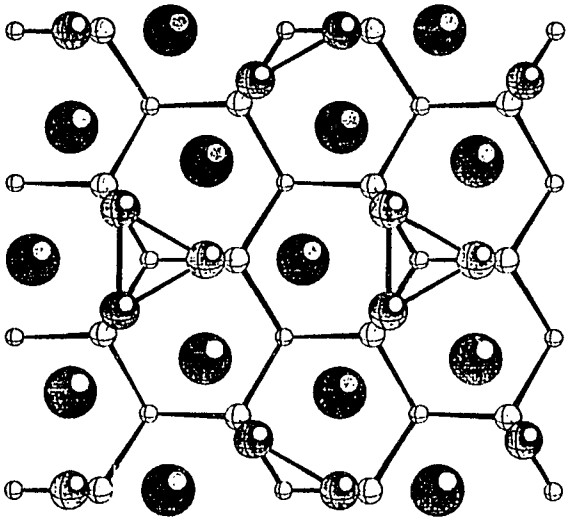

Figure 1.4. Top view schematic of the Si(111)-($\sqrt{3}$x$\sqrt{3}$)R30° Ag surface (after Ding, Chan, and Ho 1992). Large atoms represent silver, smaller ones silicon.

Next to the Si(111)-(7x7) surface reconstruction, discussed in Chapter 3, the most well studied metal on semiconductor surface structure is Si(111)-($\sqrt{3}$x$\sqrt{3}$) Ag, or simply $\sqrt{3}$ Ag. Both Takahashi and Nakatani (1993) and Jia, Zhao, and Yang (1993) provide good partial reviews of this structure's extensive body of literature. As shown in Figure 1.4 the structure consists of a Ag-Si double layer in which the silicon

atoms trimerize and silver atoms form a distorted honeycomb pattern (Takahashi et al. 1991). While a consensus has been reached on the $\sqrt{3}$ Ag structure, another structure that appears in the Ag on Si(111) system, the Si(111)-(3x1) Ag, or 3x1 Ag, (e.g., Wan, Lin, and Nogami 1995), has yet to be determined conclusively. Still, neither the copper nor silver on Si(111) systems display the variety of surface structures and behavior that are seen in the gold on Si(111) system.

### *1.2.3 Motivation to Study Gold on Si(111)*

Despite the scientific and technical interest of the above mentioned metal on Si(111) systems, we choose to study gold on Si(111) for three reasons: Au-Si's bulk behavior, almost perfect gold induced Si(111) homoepitaxy, and one of the most complicated surface phase diagrams.

The gold silicon binary alloy system has four interesting properties. First, although this system has no stable phases, it has a surprisingly low eutectic temperature, 353°C, (Andersen et al. 1971). Second, several metastable phases (e.g., Andersen et al. 1971, Tsaur and Mayer 1981) have been reported. Third, gold and silicon rapidly interdiffuse (Hiraki 1984, Green and Bauer 1976), and, fourth, gold decorates (Wong-Leung et al. 1995) and sometimes creates (Morooka, Takahashi, and Hasimoto 1992) silicon bulk defects. These four bulk properties show some unusual things are going on in the Au-Si system.

The initial studies of the growth of silicon whiskers through the vapor-liquid-solid mechanism using chemical vapor deposition showed that gold created better

silicon whiskers then other metals tested (Bootsma and Gassen 1971). This research foreshadowed the pivotal result of Wilk et al. (1994) in which 0.4 to 1.0 ML of gold, acting as a true surfactant( not diffusing into the bulk), led to essentially perfect electron beam Si on Si(111) homoepitaxy between 450°C and 500°C (Figure 1.5). In this figure $\chi_{min}$ is the RBS aligned yield, lower values indicate more perfect crystalinity.

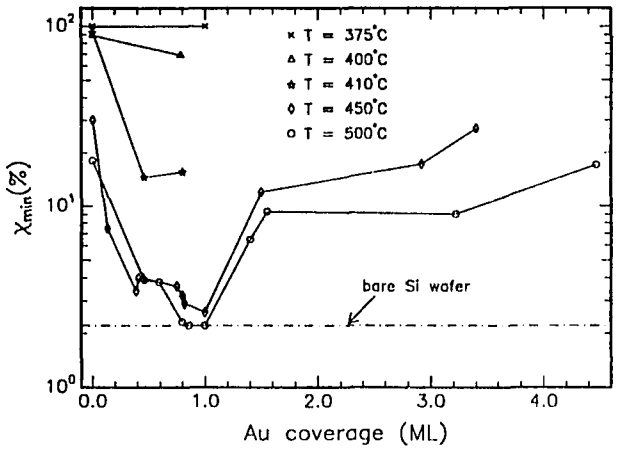


Figure 1.5. Plot of RBS aligned spectrum $\chi_{min}$ values of different homoepitaxial silicon thin films grown with various initial Au surfactant coverages and preparation temperatures. (after Wilk et al. 1994).

Finally the literature on this surface system published prior to the start of this study (e.g. Lelay 1983, Ino 1988, Takahashi, Tanishiro, and Takayanagi 1991) displays some intriguing features: no less than three possible surface symmetries (5x2, $\sqrt{3}$x$\sqrt{3}$, and 6x6), a very stable yet inherently defective linear structure (Si(111)-(5x2) Au or simply 5x2 Au), and a surface that apparently displays a wide range of short range order (Si(111)-($\sqrt{3}$x$\sqrt{3}$)R30° Au, or $\sqrt{3}$ Au). Despite the possibility of rapid diffusion of gold into silicon about one monolyer of gold remains on the Si(111) surface and other silicon surfaces over a wide temperature range, as shown convincingly by the high temperature surface profile images of Kamino et al. (1996) (Figure 1.6). This illustrates the unique bonding environment that silicon surfaces present to gold atoms. All these factors make the Au-Si surface system both intriguing and ideal for TEM

imaging analysis which is especially sensitive to defects.

## 1.3 Surface Science Techniques

A discussion and comparison of the different diffraction and imaging techniques used to study the Au on Si(111) system to date follows. The next chapter

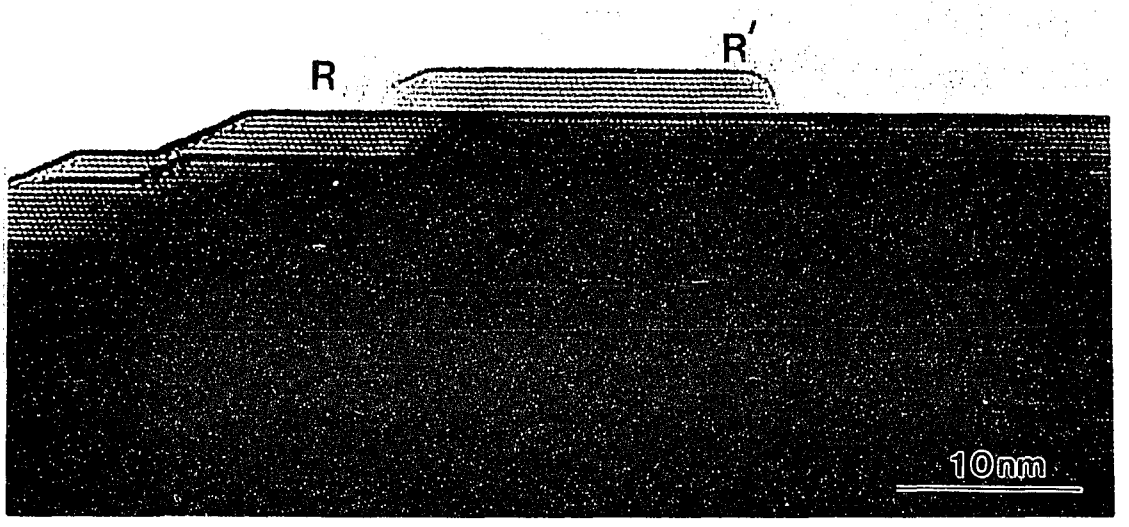


Figure 1.6. High temperature HREM profile image of different gold induced silicon surface facets (after Kamino et al. 1996).

describes experimental techniques used in this study in detail.

### *1.3.1 Diffraction Techniques*

Just as in bulk crystal characterization, surface diffraction data can be used to determine average atomic positions within the surface structure. This data can come from X-ray or electron interactions with the structure. As a result, diffraction techniques have always held a pioneering role in the investigation of surfaces.

Among the diffraction based surface science techniques, synchrotron radiation

based X-ray diffraction (XRD) is preeminent in (usually) being directly interpretable and accurately determining surface structure parameters under good conditions. This technique usually uses a grazing incidence beam angle and a reflection geometry to minimize bulk signal. The related technique of X-ray standing wave (XSW) diffraction can determine vertical atomic displacements very accurately. But as a "translation" of classic bulk XRD, surface XRD requires very bright X-ray sources to compensate for the low probability of the surface structure diffracting X-rays. Even with synchrotron sources, data collection times can be quite lengthy, limiting this techniques usefulness in in-situ experiments. Aside from availability of beam time, another other major drawback of XRD is that it has no associated imaging mode and hence is limited to studying fairly well ordered average surface structures.

Low energy electron diffraction (LEED) was one of the first techniques used to study surfaces (Davisson and Germer 1927, Zangwill 1988), and most new surfaces are first identified through LEED by their surface symmetry. Compared to synchrotron based surface XRD, LEED is a relatively straightforward and economical technique which readily and quickly provides very sensitive surface symmetry information. It is therefore quite useful for in-situ studies. However, due to the complex multiple scattering interaction of low energy electrons with surface structures, using LEED intensities to determine atomic positions is complicated, though substantial progress has been made recently (Van Hove et al. 1993).

If one uses higher-energy electron beams to diffract off the surface in reflection mode the resulting technique, reflection high-energy electron diffraction (RHEED)

eliminates many of the problems of electron-substrate interactions since high energy electrons diffract more simply from structures. However, using reflection mode causes problems of its own. Progress is being made in using RHEED to determine surface structures (e.g., Ma, Lordi, and Eades 1994), but where RHEED has found its special niche is in in-situ monitoring of molecular beam epitaxy where its unique experimental setup provides ready access to the growth surface.

While transmission electron diffraction (TED) will be discussed more fully in the next chapter, it is worth noting here that this technique, employed extensively in this study, has its own advantages and disadvantages compared to the other diffraction techniques. TED has the well established data interpretation and subsurface sensitivity characteristics of XRD and the sample accessibility and data collection speed of LEED and RHEED. Its drawbacks include the need for thin samples and unique UHV-TEM instruments.

A subtle limitation of all diffraction techniques was revealed in our analysis of 5x2 Au (Marks and Plass 1995) discussed in Chapter 4. It is possible that an important diffracted beam of the surface structure can be coincident with a bulk related beam. In such a "pathological" situation diffraction data can be misleading and, ultimately, one will have to rely on data from surface imaging techniques to obtain a complete picture of the surface structure.

Loosely related to the surface diffraction techniques are the ion scattering spectroscopy techniques. These techniques use the scattering of low atomic weight ions from a surface at various angles to compute the lateral and vertical location of the

surface atoms. These techniques have greater sensitivity to high atomic weight atoms and will be discussed more fully in Section 1.3.3.

All of the above techniques measure average structure parameters only, and are essentially blind to defect structures. These defects often play an important role in surface structures and processes. Complementing diffraction and ion scattering data with imaging techniques removes this limitation.

### *1.3.2 Imaging Techniques*

Surface imaging techniques can be split into two general categories: scanning techniques, where a fine probe of electrons scans the surface in a raster pattern, and parallel exposure, where a wide beam "bathes" the surface with illumination and the resulting diffracted beams are focused to form an image, as in a camera or an optical microscope. While the scanning techniques generally, in practice, have slightly greater resolution than comparable energy parallel techniques, they suffer from requiring longer image acquisition times. (According to the principle of reciprocity, comparable scanning and parallel techniques, such as low energy electron microscopy (LEEM) and scanning electron microscopy (SEM) or high resolution electron microscopy (HREM) and scanning transmission electron microscopy (STEM), should have identical resolution.)

By far the most common surface imaging technique used today is scanning tunneling microscopy (STM) (e.g., Binning and Rohrer 1987). These instruments are relatively inexpensive and quite versatile. STM uses a feedback loop based on the

tunneling current to surface electronic states to keep a sharp metal tip at a constant height above the surface as the tip is rastered over the surface laterally. STM has very good lateral resolution ( < 1 Å) and excellent height resolution ( < 0.01 Å) but one immediately has to ask: resolution of what? Surface electronic states is the answer which is both an advantage and a disadvantage. Imaging surface states is an advantage in that by changing the tunnelling current's applied bias one can, in principle, obtain a spatially resolved view of the surface density of states, both filled and unfilled. It is a disadvantage in that one is not imaging the locations of nuclei. Also STM requires a flat, reasonably conductive sample for good images, and surface roughness and charging greatly reduce image quality. Because of limitations in the piezoelectric elements used in rastering the tip, STM has an inherent tradeoff between lateral resolution and scanning range which limits the field of view of these techniques.

The imaging mode of LEED, low-energy electron microscopy has only been perfected relatively recently (Bauer 1985,1994, Telieps and Bauer 1985). While LEEM suffers from rather poor resolution (200 Å), its diffraction based contrast mechanism allows it to distinguish most surface structure by differences in contrast. Since LEEM has a wide field of view and (with drift correction) no limitation on sample heating, it is an ideal tool for acquiring mesoscopic, statistically significant, in-situ data (e.g, Sweich, Bauer, and Mundschau 1991).

Two research groups have been the main pioneers in the use of scanning electron microscopy SEM in surface science (e.g., Endo and Ino 1993, Azim et al.

1993), which has similar capabilities to LEEM. Here a finely focused electron beam impinging on the sample and secondary electrons are collected. While the image contrast mechanism of this mode is still under debate (Endo and Ino 1993, 1996) it would seem the work function of different surface structures play an important role.

The imaging complement of RHEED, reflection electron microscopy (REM) has good resolution ( < 3 Å) in the surface direction parallel to the beam but foreshortening severely limits the resolution ( < 40 Å, varying across the field of view) in the direction perpendicular to the beam (e.g., Osakabe et al. 1980). REM is especially sensitive to surface steps and their motion (e.g., Inoue, Tanishiro, and Yagi 1987, Latyshev et al. 1995).

When discussing transmission electron microscopy (TEM) one must realize that, as with REM, one is actually discussing a family of techniques based on different imaging modes and conditions (as will be discussed in Chapter 2). But for comparison to other techniques we can focus on HREM. As the name suggests high resolution electron microscopy has atomic resolution of surfaces, especially for high atomic number adsorbates on low atomic number substrates (Hana and Takayanagi 1992, Marks and Plass 1995). HREM has fairly good image acquisition speed, and one can image subsurface and bulk effects, but one needs thin (100-300 Å at most) samples and a good instrument. As will be discussed in detail in Chapter 2, in the process of analyzing TEM/TED data from the Au on Si(111) system, as well as the Si(100)-(2x1) and Ir(100)-(5x1) surfaces, Prof. Marks has adapted techniques from other fields to create a powerful set of tools for the structural characterization of

surfaces.

### *1.3.3 Chemically Sensitive Techniques*

Diffraction and imaging techniques both provide information on the structure of a surface from which chemical information can be inferred. But for a complete understanding of a surface structure it is preferable to obtain chemical information directly to complement the structure data.

Auger electron spectroscopy (AES) relies on the Auger effect to obtain surface sensitive chemical information to about 1% of a monolayer (Zangwill 1988). In the Auger effect a 1s electron is initially ejected by an incident 1 keV or greater electron then as, for instance, a 2s electron drops to fill the hole, a photon (X-ray) is normally released to conserve energy. Occasionally however a 2p, Auger, electron is ejected instead which then has an energy (50 to 1000 eV) characteristic of the atom it came from. If this event occurs deep in the crystal, the Auger electron will be absorbed due to a limited mean free path. This gives AES its surface sensitivity but also means some chemical signal can come from the selvedge region (the three or four crystal layers under the surface). A closely related technique is X-ray Photoelectron Spectroscopy (XPS) in which monochromatic incident X-rays are used to eject a primary electron which has a characteristic kinetic energy related to the chemical species, an Auger event can occur as well. While XPS and AES have similar surface chemical sensitivities, AES has the advantage of using focussed incident electron beam to allow for limited resolution, chemical imaging in a scanning mode (Scanning Auger

Microscopy or SAM).

Rutherford backscattering spectroscopy (RBS), or more specifically high energy ion scattering, also has unique chemical sensitivity that will be relevant in Chapter 7 (Zangwill 1988). In RBS a beam of high energy ions is directed along the atomic columns when the crystal is perfectly aligned on a low order zone axis. The directly backscattered low atomic weight ions have an energy of:

$$E = E_o ((M_1-M_2)/(M_1+M_2))^2 \qquad (1.1)$$

where $E_o$ is the incident ion energy, $M_1$ is the mass of the nucleus that was hit, and $M_2$ is the ion mass. This yields a surface peak in an energy spectrum whose intensity changes relative to changes in the surface adsorbate concentration. The ions that channel between the atomic columns and eventually backscatter out again will always have a lower energy than the directly scattered ions for clean bulk crystal surfaces, forming low energy tails. However the ions that have scattered characteristically from a surface adsorbate will not have a low energy tail unless some of the surface adsorbate has diffused into the bulk. Thus the low energy tail in RBS can serve as a signature of gold diffusion into silicon (Yuhara, Inoue, and Morita 1992a,1992b).

# 2 UHV-TEM

## 2.1 Introduction

The primary information gathering technique used in the present study is transmission electron microscopy (TEM) which actually consists of a variety of techniques. In this chapter I will detail the imaging and diffraction techniques used to obtain the information in the following chapters, many of which have been adapted for the first time for use in transmission electron microscopy. However a bulk TEM sample with the appropriate gold induced surfaces has to be prepared first.

## 2.2 Sample Preparation

### *2.2.1 Ex-situ Preparation*

Sample preparation begins with cutting 3 mm disks from a silicon (111) wafer using an ultrasonic drill. The typical 400 micron thick samples are sanded down to 150 microns from the unpolished side followed by dimpling to about 30 micron thick centers with a #3 dimpling wheel and final polishing with Syton. Etching to electron transparent thickness (100-200 Å) is done with a fresh solution of 90% $HNO_3$ 10% HF. Since this solution will etch sharp edges faster than flat surfaces the edges of the sample must be protected with a Teflon sample holder. If fresh chemicals are used the solution will usually etch the sample quickly enough so that bubbles form on

either surface. This bubbling action is good since the bubbles intermittently protect parts of the surface from etching. Intermittent protection of the surface creates a "Swiss cheese" perforated sample which is ideal since there will be several regions of thin material, though the sample will have varying thickness. This thinning procedure is our method of choice unless very large regions of electron transparent material have to be prepared with uniform thickness.

To monitor the sample thickness during the etch, a powerful point white light source is placed behind the sample. The sample will change from opaque to translucent red, orange, and yellow. Remove the sample from the etching solution just as it turns yellow-white and wash the sample in a solution of 90% pure $H_2O$, 10% HF. After optical inspection the sample should be placed in the vacuum chamber and pumped down as quickly as possible to minimize carbon contamination.

### *2.2.2. UHV Sample Cleaning and Thinning*

UHV sample preparation in this study was carried out in two different chambers; initially with a microscope side chamber equipped with an Ar ion gun and an electron gun, and later with the sample preparation evaluation analysis and reaction (SPEAR) system (Section 2.2.4). The following procedure describes the slightly different procedures used in either chamber.

Under UHV conditions the samples are cleaned of carbon and oxygen contamination and further thinned by cycles of 2.5 to 3.0 kV $Ar^+$ ion milling and electron beam annealing. Usually no or very low contamination (mainly C and O)

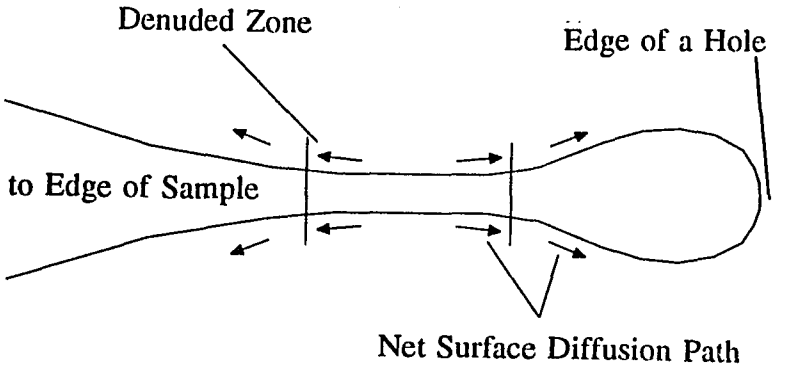


Figure 2.1. Schematic illustration of how net surface diffusion from a thin region slowly makes it thinner.

peaks are visible using parallel energy electron loss spectroscopy (PEELS) or, in later experiments, XPS and there generally are a very low number of impurity islands in the images. It is best to defocus the annealing electron beam as much as possible during the anneal. In the SPEAR system sample temperature during an anneal is monitored using an infrared pyrometer. The annealing treatment, in activating silicon surface diffusion, actually thins a thin area further though an effect first noted by Srolovitz and Safran (1986), explored further by Wong et al. (1996), and illustrated in Figure 2.1. This gives the sample characteristic "fingered" edges with thin areas between the fingers (Figure 2.2). A problem with electron beam annealing is that the thin regions generally are hotter than thicker areas setting up thermal gradients in the sample, which silicon does not seem to mind but other materials may. This procedure tends to form bulk stacking faults unless

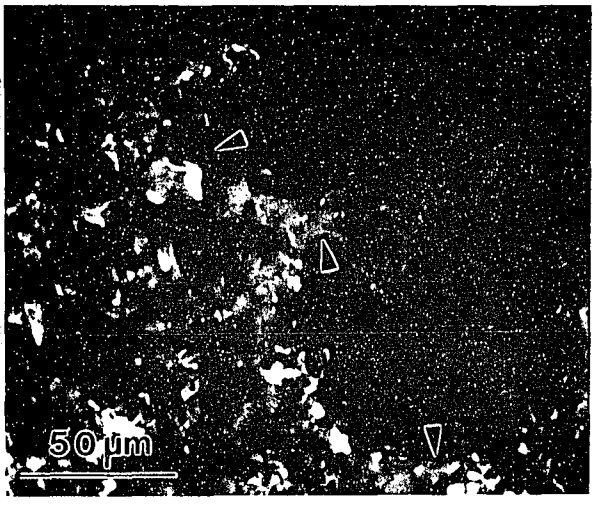


Figure 2.2. Low magnification dark field image of a typical bulk Si(111) sample after cleaning and thinning. Thinner regions are indicated with arrows.

substantial care is taken. This UHV sample cleaning and thinning procedure is superior to straight thermal etching (essentially 1000°C-1200°C Si sublimation, Takayanagi et al. 1985) which requires a good amount of luck and even then does not produce much satisfactorily thin material. (800°C $O_2$ etching, e.g. Twesten and Gibson (1994), was not attempted.) Well defined 7x7 diffraction patterns are visible but point defects, created by ion milling, coalesce into stacking fault tetrahedra whose size distribution depends on annealing temperature (Dunn, Xu, and, Marks 1992).

### *2.2.3 Gold Deposition and Coverage Calibration*

Once a strong 7x7 pattern is formed, the desired amount of gold is deposited onto one surface (the top for the imaging studies, the bottom for the diffraction studies) with the samples held at room temperature. Appendix B goes into more detail on the design of the evaporator system. The gold deposition was measured with a quartz crystal microbalance thickness monitor and during deposition the base pressure usually does not exceed $1x10^{-9}$ Torr. The appearance of various surface structures in the Au on Si(111) system at different coverages, measured by the change in microbalance beat frequency, was used to determine the "absolute" coverage versus beat frequency change calibration curve for the microscope's evaporator system. The fitting of this calibration curve is shown in Figure 2.3 and results in a value of 19 ± 1 beats per monolayer which agrees fairly well with the value of 22 ± 4 beats per monolayer obtained from stereology of gold islands deposited on amorphous carbon in a similar setup. After deposition the samples are lightly electron beam annealed to

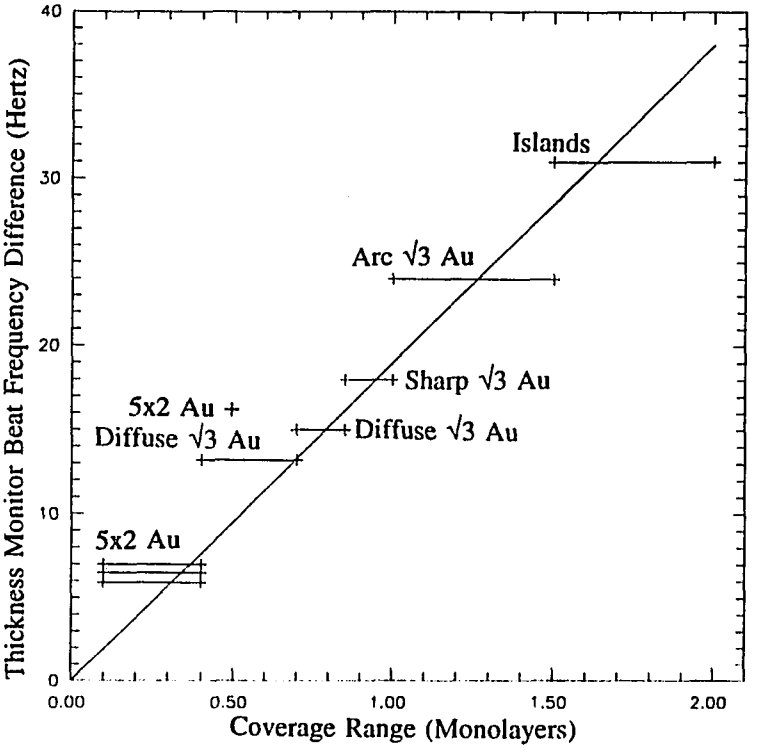


Figure 2.3. Plot of the crystal thickness monitor beat frequency change (the raw coverage reading) versus the range of possible coverages for the resulting surface structures seen. The calibration line has a slope of 19 beats per monolayer

form the surface structure of interest.

### *2.2.4 SPEAR*

While the specifics of the two sample preparation chambers used in the present study have been discussed in the literature (Marks et al. 1991, Collazo et al. 1996), it is relevant to discuss their different capabilities in sample preparation. The original UHV-H9000 sample preparation chamber was equipped with a 2 kV to 5 kV argon ion gun with an approximately 2 mm beam diameter and a 0 to 10 kV electron gun. There was no way to precisely measure sample temperature during anneals. This older

combination allowed clean samples to be prepared, but not very efficiently.

The key difference in using the SPEAR system (which has the same annealing electron gun as well as resistive sample heating) is a duoplasmatron ion gun with its 5

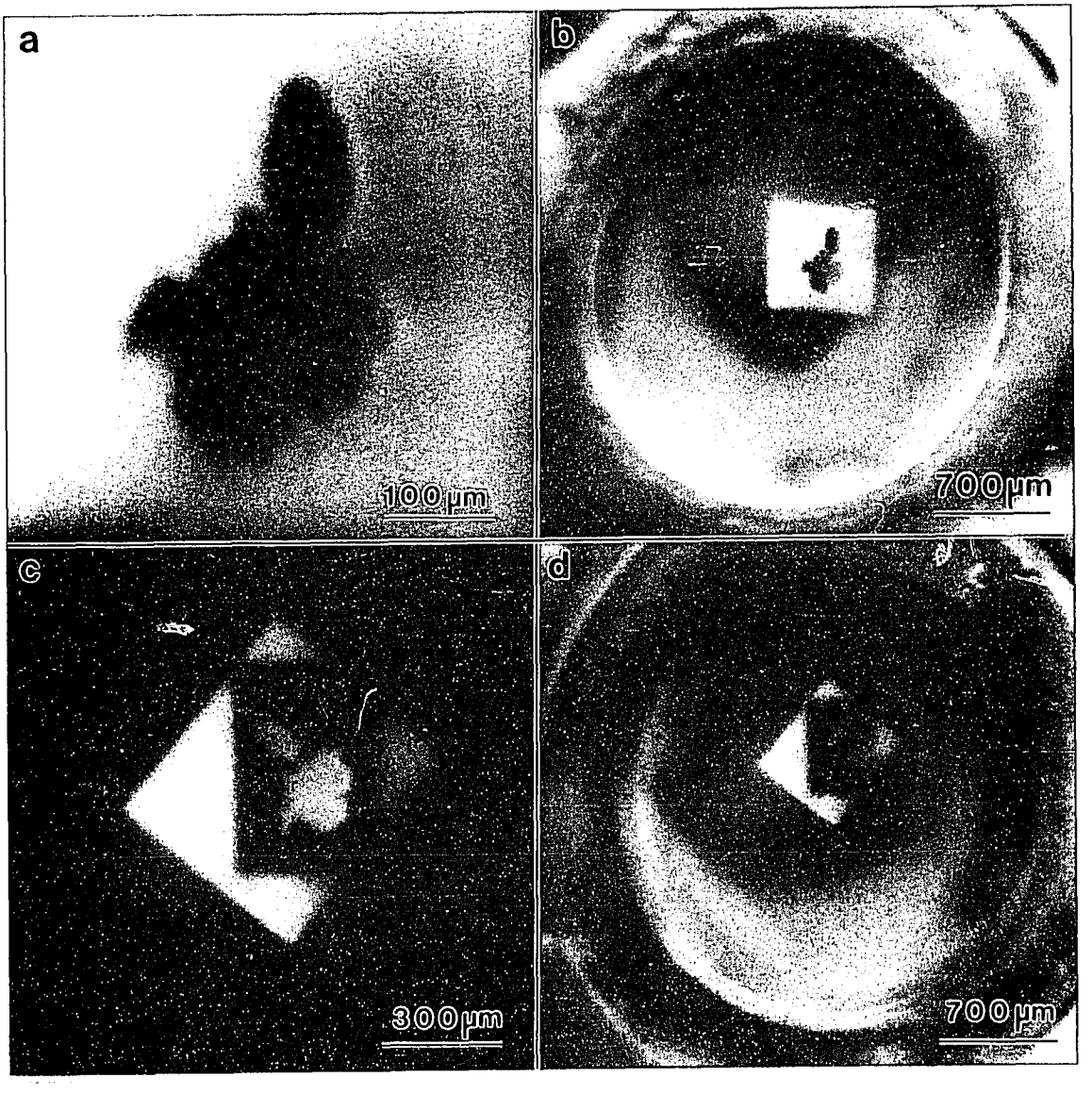


Figure 2.4. Secondary electron images formed from electrons ejected from the sample during ion milling. a) Close up of the hole region during oxygen ion milling. b) Lower magnification image showing the Mo sample holding ring and the unmilled sample areas. c) Close up of the hole after argon ion milling in the central rectangle. d) Lower magnification image after argon ion milling in the center.

micron minimum beam diameter. This ion gun allows the sample to be imaged with the secondary electrons emitted as the scanning ion beam mills the sample. Another key feature of this gun is that it can mill using oxygen ions which readily removes residual carbon contamination before the first anneal. In the old system argon ion milling tended to drive carbon into the sample where it would form SiC that required several more milling cycles to remove. To remove the oxide layer created by the 4 kV oxygen milling, a second milling of both surfaces with 3kV Ar ions is performed. An unexpected benefit of the secondary electron imaging is that pristine sample regions appear gray, oxygen milled regions appear white, and argon milled regions appear black as in Figure 2.4. Thus one can be sure all the different regions of the sample have been cleaned without accidentally milling of the Mo sample holder ring. The pyrometer allows for good reproduction of annealing cycles as well as much better control of the annealing cycle, important for long anneals. The XPS and AES capabilities of SPEAR ensure that the sample is initially clean.

## 2.3 General TEM Imaging Techniques

Now that we have gone through the agony, er..., the rate limiting step of sample preparation we are ready to employ TEM techniques to study the surface.

### *2.3.1 Imaging Theory*

The basic principles involved in transmission electron imaging are very similar to those involved in transmission optical microscopy, i.e., resolution limitation,

aberrations, sample limitations, noise effects, etc. A microscope's resolving power for imaging certain features separated by a distance, x, is determined primarily by the wave length, $\lambda$, of the waves used for imaging (e.g., Cowley 1990, Born and Wolf 1980).

$$x = 1.22 \lambda / \alpha \qquad (2.1)$$

where $\alpha$ is the convergence. To image atoms one needs wave lengths substantially smaller than the typical spacing between atoms. These can be provided either by X-rays or 50kV plus electrons. Then, just as in light microscopes, what is needed to obtain the magnification that images atoms is a wave source with a reasonably narrow energy spread, a means of focusing the waves, a thin enough sample so that most of the wave scatters off features only a few times at most, and a means of recording the scattered wave. In the case of X-rays the low scattering probability requires X-ray sources that are brighter than the current synchrotron sources to obtain an image in a reasonable time. (X-ray focusing is accomplished with zone plates and the low scattering probability could allow samples to be fairly thick.) In the case of electrons, scattering probability isn't a problem so a few types of electron sources can provide adequate brightness. In fact, the high scattering cross section poses a problem in that samples generally have to be thinned to less than a few hundred Angstroms for many TEM techniques.

The key resolution limiting problem that arises in electron imaging is the inability to create a concave electron lens with magnetic or electrostatic lenses. Therefore spherical and chromatic aberration cannot be compensated for with

combinations of concave and convex lenses as is done in optical microscopy.

### *2.3.2 Electron Microscope Aberrations*

Given the relativistic wave length of a 300kV electron beam, 0.0197 Å (Hirsch et al. 1977), it should be simple to resolve and readily interpret high resolution electron microscopy images since typical interatomic distances are of the order of 2 Å. However, several features of an electron microscope limit image resolution and interpretability. Electron microscopy aberrations are classified into two categories, incoherent and coherent. Chromatic aberration (which depends on lens design), focal spread (which comes from source and lens instabilities), vibration, and drift (sample or current) are all examples of incoherent aberrations which together limit the actual resolution of the instrument. Spherical aberration (higher order beams are not focused to the same point as lower order ones), beam tilt (the transmitted electron beam passes through the column off axis causing one plane of the sample to be focused at different vertical locations), and astigmatism (arising from lens imperfections, beams on one horizontal axis are focused differently than those on a different horizontal axis) are examples of coherent aberrations. While coherent aberrations do not limit the microscope's true resolution, they "scramble" the higher resolution information by causing contrast reversals and contrast zeros for different spatial frequencies making the higher resolution information useless. But a more subtle effect involves the sample thickness.

The sample is usually much thicker than the focused electron beam

"crossover"; therefore, one images different slices of the sample with different defocus. This is similar to sweeping through a thick semi-transparent sample at high magnification in an optical microscope: one can see different layers of the sample while the other layers form a blurred background. Unfortunately, because of the small scattering angle (Spence 1988), electron microscopy has a greater depth of field than optical microscopy. Instead of "blurring out", the images from the different layers, each with a different defocus, sum coherently to form a complex interference pattern. Several authors go into more detail on these aberration effects (e.g., Cowley 1990, Hirsch et al. 1980, Spence 1988) and they will also be discussed in Section 2.3.5. Unraveling this complex situation has traditionally followed two approaches, which will be reviewed next.

### *2.3.3 HREM Through Focal Series Image Matching*

The information missing from, or contrast reversed, in one particular image can, in principle, be captured in another HREM image with a different defocus. This is the principle behind taking HREM through focal series in which HREM images are taken at regular defocus steps. The information in a focal series, which redundantly contains all the high resolution information up to the limit set by the incoherent aberrations, can be recovered in one of two ways. First, using multislice simulation, the effect of a given atomic model's interaction with the electron wave can be simulated fairly well. Second, the measured aberrations can be used to "reconstruct" the original image from a focal series (next section).

First proposed by Cowley and Moodie (1959) and refined by Goodman and Moodie (1974) the multislice algorithm approximates dynamical (multiple event) diffraction by following the electron beam through the crystal and calculating the scattering probabilities at every atomic plane of the crystal. This is done by slicing a crystal into very thin layers along the electron beam direction. Atomic scattering of the beam is assumed to occur through a "phase grating" type transmission function in a single plane containing "flat" atoms. Then the modified beam propagates "in vacuum" along the beam direction, characterized by a propagation function, before it encounters the next slice or plane of 2-D atoms. Then the transmission and propagation cycle is repeated, and so on through the entire crystal. The multislice algorithm has been found to be an excellent approximation to the more proper Bloch wave quantum mechanical treatment of the interaction of high energy electron waves with crystals for several simple cases (Hirsch et al. 1977).

The effects of approximated coherent and incoherent aberrations and shot noise are then added to the multislice generated sample wave by image processing techniques to simulate the microscope's unique optics. One can then prepare a simulated through focal series to compare to the experimental one. If the simulated series matches the experimental one reasonably well then the model is a good match to the crystal structure. A drawback of this image matching approach is that it is not a direct approach; one has to guess at the correct structure. Also it is limited by computer power in simulating defect structures. However, it is still the more "honest" of the two approaches since it contains less pitfalls than the reconstruction approach

discussed next.

### *2.3.4 Through Focal Series Reconstruction and Electron Holography*

Another approach to recovering the information in a through focal series is to "reconstruct" the unaberrated image from the series. This requires guessing the phase and amplitude of the wave at every pixel. The redundant nature of the information in a through focal series allows for consistency checks of these "guesses." While variants of this approach seem to work with bulk structures (e.g., Coene et al. 1992) and work well on small simulated test images of surfaces, when this approach was tried on experimental surface data, it failed to find a satisfactory phase solution.

A better, though experimentally much more complicated, approach is to record the amplitude and phase of the electron wave directly in a hologram and then recover or reconstruct the aberrated object wave. This involves having the wave leaving the sample overlap with an unperturbed "reference wave" in the image plane by bending both waves with an electron biprism (Gabor 1949, Tonomura et al. 1979, Mollenstedt and Druker 1954). The resulting interference pattern is then recorded and, through either optical or numeric reconstruction, both the amplitude and the phase of the original wave can be recovered. With both the wave's amplitude and phase measured, the process of removing the coherent aberration distortions becomes easier (if the aberrations are accurately known) but the resolution is still limited by the incoherent aberrations (Marks and Plass 1994). In addition to providing complete information about the object wave (thus eliminating, in principle, the guesswork involved in

finding atomic positions) electron holography can also simultaneously provide information such as sample thickness, mean inner potential, and internal charging. A serious drawback to electron holography is that obtaining a good electron hologram requires a stable TEM equipped with a field emission electron gun and an electron biprism. Holography also places stringent requirements on the imaging conditions and sample geometries that can be used.

While electron holography was not used to obtain any of the results in this study, our detailed analysis of the effect of microscope aberrations in this mode (Marks and Plass 1994) led Prof. Marks to a simple and elegant mutual coherence analysis of regular HREM imaging mode that has some features worth mentioning (Marks 1995).

### *2.3.5 Mutual Coherence*

Mutual coherence is defined (e.g., Born and Wolf 1975) as:

$$\Gamma(\mathbf{r}_1,\mathbf{r}_2) = \langle\psi^*(\mathbf{r}_1)\psi(\mathbf{r}_2)\rangle \tag{2.2}$$

where $\psi(\mathbf{r})$ is the wave function at two different real space points, $\mathbf{r}_1$ and $\mathbf{r}_2$ (we assume an "ideal" microscope, no magnification) and $\langle\ \rangle$ is an appropriate statistical average. Transformation of this function involves two integrals:

$$\Gamma(\mathbf{u}_1,\mathbf{u}_2) = \langle\psi^*(\mathbf{u}_1)\psi(\mathbf{u}_2)\rangle = \iint \Gamma(\mathbf{r}_1,\mathbf{r}_2)\exp[2\pi i(\mathbf{u}_1\cdot\mathbf{r}_1-\mathbf{u}_2\cdot\mathbf{r}_2)]d\mathbf{r}_1 d\mathbf{r}_2 \tag{2.3}$$

where $\mathbf{u}_1$ and $\mathbf{u}_2$ are the corresponding reciprocal space vectors of $\mathbf{r}_1$ and $\mathbf{r}_2$. In our general analysis (Marks and Plass 1994) we found that prefield optics effects can be neglected in most cases, so we can treat Equation 2.3 as the "wave" impinging on the

sample. (In discussing mutual coherence the average "wave" is only definable in a statistical sense, as is done in quantum field theory, and may not be separable into individual waves.) The diffraction effects of the sample are included as a summation of individual terms:

$$\Gamma(\mathbf{u}_1+\mathbf{g},\mathbf{u}_2+\mathbf{h})\phi^*_{-g}(\mathbf{u}_1)\phi_h(\mathbf{u}_2) \tag{2.4}$$

where $\phi_h(\mathbf{u})$ is the phase change induced by a given crystal reciprocal lattice vector. For thin crystals the effect of the incident beam on diffraction can be ignored, giving a constant phase change for each crystal reciprocal lattice vector. This change plus inclusion of the effects of post specimen coherent aberrations yields:

$$\Gamma(\mathbf{u}_1+\mathbf{g},\mathbf{u}_2+\mathbf{h})\phi^*_{-g}\phi_h\exp[iX(\mathbf{u}_1+\mathbf{g})-iX(\mathbf{u}_2+\mathbf{h})] \tag{2.5}$$

where:

$$X(\mathbf{u})=\pi/\lambda(\Delta z\lambda^2u^2+0.5C_s\lambda^4u^4) \tag{2.6}$$

$\lambda$ is the electron wave length, $\Delta z$ is the defocus and $C_s$ is the spherical aberration. $X(\mathbf{u})$ is the aberration phase shift function.

Since the convergence is assumed to be small we can expand $X(\mathbf{u})$ in a Taylor series to get:

$$\Gamma(\mathbf{u}_1+\mathbf{g},\mathbf{u}_2+\mathbf{h})\phi^*_{ig}\phi_h\exp[iX(\mathbf{g})-iX(\mathbf{h})+i\mathbf{u}_1\cdot\nabla X(\mathbf{g})-i\mathbf{u}_2\cdot\nabla X(\mathbf{h})] \tag{2.7}$$

then back transforming:

$$\sum_{\mathbf{g},\mathbf{h}} \Gamma(\mathbf{r}_1+1/(2\pi)\nabla X(\mathbf{g}),\mathbf{r}_2+1/(2\pi)\nabla X(\mathbf{h}))\phi^*_{-g}\phi_h\exp[iX(\mathbf{g})-iX(\mathbf{h})]\exp(2\pi i(\mathbf{g}\cdot\mathbf{r}_1-\mathbf{h}\cdot\mathbf{r}_2) \tag{2.8}$$

To get the final "intensities" we set $\mathbf{r} = \mathbf{r}_1 = \mathbf{r}_2$ yielding:

$$I(\mathbf{r})=\sum_{\mathbf{g},\mathbf{h}} \Gamma(\mathbf{r}+1/(2\pi)\nabla X(\mathbf{g}),\mathbf{r}+1/(2\pi)\nabla X(\mathbf{h}))\phi^*_{-g}\phi_h\exp[iX(\mathbf{g})-iX(\mathbf{h})]\exp(2\pi i((\mathbf{g}-\mathbf{h})\cdot\mathbf{r}) \tag{2.9}$$

This analysis does not include the chromatic incoherent effects leading to the envelope term ut it inherently includes beam convergence. In a more conventional analysis (e.g., Self and O'Keefe 1988) the final waveform integral would simply be squared to obtain the final intensity; here we see the greater generality of using mutual coherence since the holographic mode can be treated properly (Marks and Plass 1994).

The key benefit from the above analysis comes from looking at what the result means physically, shown in Figure 2.5. In this figure we can see that beams from two different locations on the sample interfere with each other in the image. The spatial phase shift between the two locations is related to the aberration phase shift of the diffracted beams. The integrated interference of all these pairs of diffracted waves leads to the final intensity at that location.

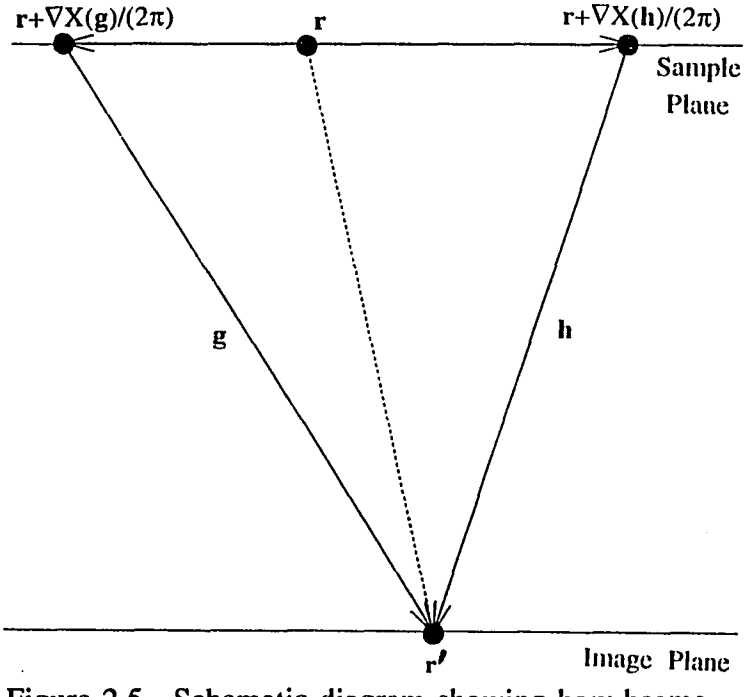


Figure 2.5. Schematic diagram showing how beams from sample locations, related by aberration phase shifts, interfere in the image plane.

The mutual coherence function itself is strongly effected by the incoherent convergence of the beam (Born and Wolf 1975). Convergence sets the full-width half-max width of the averaging function < >, thus directly limiting the width over which

either the **r** or **u** vector's wavefunctions can be summed. This is related to the fact that in holography the "visibility", or true contrast of the interference pattern drops with increasing convergence. Therefore, aside from providing a clear framework for understanding imaging, the mutual coherence function has some bearing on the present study in that it explains a general rule of thumb in taking diffraction patterns. We have found it is better to shoot diffraction patterns at as low a beam intensity (smallest convergence) as possible. Small convergence means that you will maximize the mutual coherence of the object wave with itself and thus enhance the intensity of the higher order beams with respect to the inelastically scattered background intensity.

### *2.3.6 Bright Field / Dark Field Imaging*

While high resolution imaging mode is good for atomic imaging, its limited field of view is a hinderance when collecting statistical image information such as bulk defect concentration or surface domain size distribution. One could simply lower magnification to correct this but the pixel sampling is then not sufficient to adequately record higher resolution features. This problem can be corrected by introducing an objective aperture into the "diffraction plane" just below the sample. With this aperture one can choose to image using only the transmitted beam (bright field imaging), a strong diffracted beam (dark field imaging), or some combination. By blocking other beams with the aperture one greatly enhances the contrast of defect features and thickness contours but at the cost of loosing resolution.

To obtain reasonably good resolution in dark field mode one must take care to

align the imaging beam on the microscope axis and to get the aperture as well centered as possible. This is done by using the beam tilt correction procedure while in dark field mode. One trick that was discovered during the present study is to use an objective aperture that is just large enough to block the Si(111) 220 type diffracted beams when in bright field mode. This allows the maximum number of surface superstructure beams to generate surface cross fringes, enhancing their contrast, while still eliminating the high contrast 220 type bulk fringes. While quantitative image analysis cannot (easily) be performed on such "high resolution" bright field and dark field images, they can provide well resolved surface defect information and, occasionally, surface structure symmetry information.

## 2.4 Surface Sensitive Imaging

With our background discussion of relevant general TEM imaging techniques completed one may ask how, given the strong contrast generated by the bulk, one can hope to isolate information from surface features. Initially conventional wisdom said that a surface, in behaving like a bulk defect, could only be imaged adequately with weak beam techniques. Cherns took the first steps toward Imaging surfaces without using weak beam techniques in 1974. By using an objective aperture to isolate 1x1 beams of well ordered surfaces while near the zone axis, Cherns obtained good images of surface steps. The 1x1 beams are forbidden for an infinitely thick crystal but fractional unit cell termination of a bulk crystal allows these beams to have some intensity, providing a contrast mechanism to distinguish surface terraces of different

relative heights. Later Lehmpfuhl and Uchida (1979) showed that steps could imaged for any crystal symmetry provided the surface is well ordered, i.e., the 1x1 and other surface superstructure spots (or the "surface spots" coincident with bulk spots when there are no forbidden reflections) are strong; otherwise, the surface contrast will be close to the noise level in dark field mode. Modifications of Chern's original technique have been implemented by others (e.g. Gibson, McDonald, and Unterwald 1985, Dunn, Xu, and Marks 1994) and even adapted for in-situ studies of oxygen etching of silicon (111) surfaces (Gibson and Lanzerotti 1989).

### *2.4.1 HREM On-Zone Imaging*

As mentioned in Section 2.3.6, while dark field is good for statistical and in-situ analysis, it is inherently limited in resolution. To image surface atomic structure and small defects one needs HREM for surface imaging (e.g. Nihoul, Abdelmoula, and Metois 1984). HREM of surfaces can be done (with care) either in a near-zone mode or in off-zone mode.

In pioneering work by Dunn, Xu, and Marks (1994) near-zone high resolution images of the Ir(100)-(5x1) surface were image processed to attenuate the bulk lattice fringes and reveal the surface structure's symmetry. a soft aperture was applied to the image numerically. This study also imaged surface steps and 1x1 terraces. But this image processing approach (also used for $\sqrt{3}$ Au) can cause artifacts and limits resolution. In the Ir study images taken further off the zone axis seemed to give better results although the beam intensities were lower (Xu et al. 1993).

### *2.4.2 HREM Off-Zone Imaging*

A systematic PEELS study (Xu and Marks 1992) of the different bulk and surface diffraction spots revealed that, while all the beams were losing intensity in far off-zone conditions, the surface beams were gaining in intensity relative to the bulk beams. This can be expected from an cursitory analysis of the intersection of the Ewald sphere with the reciprocal space relrods. The surface relrods will be longer and more uniform than the bulk crystal ones. The problem with using this to obtain better surface HREM images is that all beams are weak compared to the background noise; noise filtering is needed to extract the relevant surface information from the raw HREM images.

Image noise filtering is a relatively mature field but it has not been used extensively in electron microscopy. Fourier filtering, in which windows are applied to the Fourier transform of an image to reduce or eliminate noise, is commonly used but extreme care must be taken so that artifacts are not introduced into the image. A more objective noise filter comes from the nature of HREM images. Since they are generally periodic, a good estimate of an image's noise spectrum can be made from image power spectrum regions without diffracted spots. This noise spectrum, $\eta$, can then be used to reduce image noise levels by applying a filter, F, to the image, I, in frequency space to estimate the true signal, S., i.e., where:

$$FI = S \tag{2.10}$$

$$I = S + \eta \tag{2.11}$$

The conventional Wiener filter (Wiener 1942), the "optimum" noise filter

mathematically, is found by minimizing:

$$W = \Sigma(FI-S)^2 \tag{2.12}$$

which reduces to:

$$F = \langle S^2 \rangle / I^2 \tag{2.13}$$

with $\langle S^2 \rangle$ being the expectation value of the signal squared, usually:

$$\langle S^2 \rangle = |I^2| - \eta^2 \quad \text{for } |I| > \eta \tag{2.14}$$

$$= 0 \qquad \text{for } |I| < \eta$$

This filter assumes the signal and noise are uncorrelated.

A refined form of the conventional Wiener filter more appropriate for HREM images is the Random-Phase Parametric Wiener Filter (Marks 1996) which minimizes:

$$W = |QS|^2 + \lambda_1\Sigma[(I-S)^2-\eta^2] + \lambda_2\Sigma(I-s) \tag{2.15}$$

where Q is a linear operator, $\lambda_1$ is a Langrangian multiplier that takes into account correlation between the signal and noise, and $\lambda_2$ is another multiplier that effectively removes a background noise based on the assumption that the phase of the noise is random. The resulting filter has good stability and can improve signal to noise ratios by a factor of 5 to 7 (Marks 1996).

There are two practical considerations involved in using these filters: while the fringes of a surface structure may not be readily visible in the raw image, if corresponding surface spots are not readily visible in the power spectrum the image is not usable. Secondly, using too large an initial error estimate will cause the image to be over filtered resulting in loss of information and image artifacts. A properly filtered image still has some residual noise, as seen in Figure 4.3.

## 2.5 Diffraction Techniques

### *2.5.1 Basics*

The use of diffraction data to solve bulk crystal structures has a long history, both through X-ray diffraction and through electron diffraction. Just as in real space where the atomic potential $\rho(\mathbf{r})$ for a certain image vector $\mathbf{r}$ is given by:

$$\rho(\mathbf{r})=[\rho_o(\mathbf{r})\sum_{lmn}\sum\sum\delta(\mathbf{r}-(l\mathbf{a}+m\mathbf{b}+n\mathbf{c}))]s(\mathbf{r}) \qquad (2.16)$$

where **a**,**b**,**c** are the unit cell vectors, $\rho_o(\mathbf{r})$ characterizes the contents of the unit cell (the function of interest), and $s(\mathbf{r})$ is the shape function. Similarly we can write:

$$\rho(\mathbf{r})=\sum_{\mathbf{h}} F(\mathbf{h})\exp(-2\pi i\mathbf{h}\cdot\mathbf{r})s(\mathbf{r}) \qquad (2.17)$$

where $F(\mathbf{h})$ is the complex structure factor (Cowley 1988). The phases and amplitudes of these structure factors need to be determined to provide the location of the atomic potentials in the unit cell. Since diffraction patterns provide only the amplitudes of the structure factors, determining the structure factor phases from supplemental information and structure simulations is where the art of structure determination comes in (e.g., Cowley 1988, Schwartz and Cohen 1987). A key difference in the approach to solving structures with X-ray diffraction and electron diffraction is that the low scattering probability of X-rays allows simpler, single scattering event, kinematical theory to be employed while the much higher scattering probability of electrons require multiple scattering dynamical diffraction theory unless the sample is very thin.

Which of these diffraction theories is appropriate for electron diffraction of

surfaces is a matter of some debate. In principle, electrons in transmission mode pass a surface only once, forcing a kinematical condition. However, this is true only for reconstructed bottom surface; if both surfaces have the same reconstruction the situation is less clear. The very first analysis of the surface electron diffraction problem was by Spence (1983), who proposed that simple kinematical, single scattering theory could be applied. Such an approach was used by Takanayagi et al. (1985) in their analysis of the 7x7 surface employing symmetry averaging to reduce dynamical, multiple scattering effects, an approach which they later justified with calculations (Tanishiro and Takayanagi 1989a). Marks et al. (1991) showed experimentally that a kinematical approach would be reasonable in an off-zone orientation and most recently Twesten and Gibson (1994) demonstrated fairly good agreement between the data they refined using kinematical theory and X-ray diffraction refinements for the 7x7 surface.

Contrary to these papers advocating a kinematical approach, there have been a number of analyses using dynamical diffraction. Analyses of the surface 1x1 diffraction spots date back to the work of Cherns (1974). Full dynamical diffraction is required to accurately simulate the bulk crystal on which the reconstruction resides (Spence 1988). Work by Marks (1992) showed that dynamical effects depend rather strongly upon the registry of the reconstruction with respect to the surface, so generalizations are dangerous. These are just two of several instances which indicate where a kinematical analysis of surface diffraction can break down. But in the final analysis, the appropriate level of diffraction theory required is actually determined by

the experimental measurements. Kinematical theory is at best an approximation to more rigorous dynamical models, and the key issue is whether the experimental errors are larger than the modelling errors. The factors that determine these experimental errors are discussed in the next section.

### *2.5.2 Data Set Preparation*

The guiding principle in shooting through exposure series diffraction patterns is that you want at least two or three exposure sets, preferably more, with each having as large a dynamic range of intensities as possible. The absolute intensity of the transmitted beam and strong bulk beams needs to be recorded so that the bulk crystal can be accurately simulated, while the very weakest, higher order, surface beams, even if poorly measured, are the key to finding precise atomic positions.

There are several conditions involved in collecting good diffraction data; the more closely they are followed the more precise and useful the data set will be. Diffraction patterns should be taken from as well ordered a surface as possible. Often when a superstructure first appears the diffraction spots are weak and diffuse, usually indicating the surface has only small ordered domains. As one would expect, this surface will not provide very precise atomic locations since the weak higher order beams are lost in the background. Subsequent annealing cycles tend to order up the structure, therefore only a couple of exposure series of the initial surface should be taken (to have some documentation if disaster strikes) and focus should be placed on the more well ordered structure.

A crystal tilt well off-zone that does not strongly excite any bulk beams should be chosen while keeping as many surface spots on the zero order Laue zone as possible. Currently the multislice crystal simulations in use do not succeed in accurately simulating higher order zones, thus inherently limiting the data set to providing only x-y projected atomic locations. In the future, however, with increases in computer power and refinement of multislice algorithms, the higher order surface spots could provide atomic height information.

The exposure series should be taken so as to minimize the background as much as possible. This means looking for very thin regions (PEELS greatly facilitates this search) which also have fairly uniform thickness across the selected area aperture. The diffraction defocus should be set so that surface structure spots are about 1 to 2 mm wide on the negatives, usually two or three clicks from sharpest focus. (Use of a CBED like condition gives better precision for strong beams but the weak high order beams get lost in the background.) Brightness is set for about a 60 second metered exposure and checked so that the intensity is stable for at least five minutes. Take at least nine or ten exposures from half a second to 120 or 240 seconds, doubling the exposure time each negative. After shooting the negatives PEELS should be used to get the raw counts of the transmitted beam and the strongest bulk beams, preferably without touching the intensity controls.

The negatives are usually digitized with 25 micron resolution so that the diffracted spots are captured over an area of tens of pixels. Cross-correlation algorithms are then used to quantify the intensities in each negative (Xu, Jayaram, and

Marks 1994, Saxton 1994). In implementing these algorithms first, a motif for the shape of a diffraction spot is generated by averaging a number of stronger surface spots. This motif is then cross-correlated with experimental spots to determine the spots integrated intensity. For a completely unknown surface structure, care must be taken in indexing the diffraction pattern. The indexing process imposes a certain symmetry and set of spacings which, if incorrect, can cause big problems latter.

The data from all the negatives in an exposure series are combined in a three step process to obtain the mean beam intensities and errors. The key to this combining process is determination of appropriate intensity scaling terms which compensate for the differences in exposure times between the negatives. First, initial relative exposure levels of the negatives are determined by a least-squares fit using beams which occur in more than one negative. (These exposure levels are generally close to those determined from the exposure times.) Then these initial exposure values are used to obtain a first estimate of the mean intensity of each beam, and from this, the error from the mean beam intensity in each negative. From previous work (Xu, Jayaram, and Marks 1994) we know that the errors obey counting statistics, so for any given negative the standard deviation of the errors will be some constant scaling term times the intensity of each beam. From the distribution of errors new scaling terms are determined and improved estimates of the weighted mean intensities are then determined. After iterating this process a few times the results converge to give a set of mean relative intensity measurements per negative, each with a known standard deviation. If PEELS measurements were performed then these relative

intensity results can be scaled to absolute beam intensities, allowing more accurate sample thicknesses and absolute surface coverages to be determined later. The approach of determining the intensity scaling factors through each negative's error distribution gets around the rather sticky problem that each of the repeat measurements for one beam has a different error associated with it because each measurement has a different number of counts. This makes the least squares approach to finding the scaling terms invalid since an accurate weight cannot be assigned to each repeat measurement, a chicken and egg problem.

With the bulk and surface beams now quantified the bulk crystal's tilt and thickness are determined by matching simulated diffraction patterns to the experimental ones. Matching is mainly done by eye, only very good candidate thickness and tilt combinations should be considered for an absolute value based final parameter (thickness and tilt) fitting procedure. These procedures often tend to move into local minimum solutions away from a visually correct solution so as to fit strong (low $\sigma$) beams better. The level of accuracy needed in fitting the bulk parameters depends on the precision of the data set. Often a carefully determined, good visual fit will suffice and taking a bulk parameter fit beyond this stage is not easy. The completed TED surface data set includes the intensities and errors of the surface beams and the fitted thickness and tilt of the bulk crystal.

### *2.5.3 Direct Phasing*

Sometimes a situation arises in surface science where a new surface's

symmetry and unit cell have been identified by LEED or a comparable technique but essentially nothing reliable is known about the structure. Without a reasonably good starting structure the traditional X-ray diffraction structure refinement algorithms simply won't converge on a solution; these are good at refining a structure, not finding it. This is exactly what happened in our study of 5x2 Au; we had good TED data sets but no viable starting model of the structure. Therefore I will discuss the process of structure determination and refinement assuming no information on the structure exists in the literature to show how, in principle, the TED data sets and coverage information alone can be used to solve the surface structure. Of course any existing literature data greatly assists in this process. The first and perhaps most powerful technique for finding these starting models is direct phasing.

As was discussed in Section 2.5.1, the reason why diffraction data alone cannot solve an atomic structure is that the structure factor phase information is lost in the recording process. If this were not the case, one could simply take the Fourier transform of the amplitudes and phases of the different beams, and an image corresponding to the atomic potentials of the crystals would result. From the different scattering strengths of the atoms, mirrored in the atomic potentials, one could then easily interpret the image for species and location. While phase information is lost in the diffraction patterns there exist certain probable relationships among the phases. Sayre (1952) formulated these relationships in terms of the complex structure factors:

$$\mathbf{F(h)} = \theta(\mathbf{h}) \sum_{\mathbf{k}} \mathbf{F(k)F(h-k)} \qquad (2.18)$$

of beam **h** where $\theta(\mathbf{h})$ is the ratio of the Atomic Scattering Factor (ASF) to $ASF^2$. This formulation was expressed in terms of the phases by Cochran (1955) as:

$$\phi(\mathbf{h}) \approx \phi(\mathbf{k}) + \phi(\mathbf{h}-\mathbf{k}) \qquad (2.19)$$

Where $\phi(\mathbf{h})$ is the phase of beam **h** and $\approx$ means probably equal to (with an associated distribution). This equation allows one to determine the probable phase of a third weaker beam given initial guesses for two stronger beams. In the process of predicting the phases of all the beams in the diffraction pattern consistency checks allow better initial guesses and the process is repeated. (In practice, for the surface data sets, a brute force approach of mapping many "initial guess" phase combinations and judging the resulting solutions on a "peakiness" figure of merit, i.e., the solution's kurtosis, was more efficient than search algorithms. This is because surface structures are relatively simple compared to the complex organic crystals that direct phasing algorithms are usually solving.) Using the phases of strong beams to determine the phases of weaker beams is the essence of direct phasing (Woolfson 1987 is an excellent review). Despite several reasons one might expect for it not to work for surface structures (Marks, Plass, and Dorset 1996), direct phasing turns out to be surprisingly easy to implement and gives good results for the 5x2 Au and $\sqrt{3}$ Au structures. Presently, "windowing" weight functions and scattering potential information are being tested as additions to our direct phasing algorithm to better adapt it to surface studies.

Still, direct phasing has its limits. Usually beams no farther out than one $Å^{-1}$ are included in data sets, even in bulk analysis, since phase determination errors

increase as the beams get weaker, leading to artifacts. This limits direct phasing resolution drastically. A more subtle problem is that, as with indexing a new surface diffraction pattern, use of direct phasing requires making some assumptions about the surface structure. If the assumptions are wrong the solution will be wrong or, if you are lucky, the solution will not converge. Direct phasing usually comes up with multiple surface structure solutions. These solutions may be lateral translations or inversions of each other. Also, and as we shall see with $\chi^2$ analysis as well, a direct phasing solution may have a very good figure of merit and still be unphysical. All in all, with care, direct phasing is very good at getting potential starting structures for a surface from which we can usually go to $\chi^2$ refinement. But first, another technique employed for complex surface structures is worth discussing.

### *2.5.4 Heavy Atom Holography*

A different approach to finding a starting structure is to utilize known information from high resolution images or direct phasing results to identify other parts of the structure. This involves the principles of in-line holography and has been coined "heavy atom holography" (Marks and Plass 1995) since it is also based on the heavy atom method of X-ray diffraction analysis (e.g., Cowley 1990). Normally electron holography uses unperturbed waves as reference waves since they can be reasonably approximated as either plane or spherical waves, but the mathematical framework of holographic reconstruction can use any reference wave so long as it is well characterized. What heavy atom holography does is treat the diffraction from

known and unknown portions of the sample exit wave as two separate waves that interfere. Then reconstruction is used to isolate the unknown portion of the wave, from which new candidate atomic sites are identified.

Specifically, given an estimate for the wave $\Psi(\mathbf{u})$ generated by a $\chi^2$ minimization of the known atom locations, we look for the unknown wave $w(\mathbf{u})$ which minimizes:

$$R^2 = < (I(\mathbf{u})-\alpha|\Psi(\mathbf{u})+w(\mathbf{u})|^2)^2 > \qquad (2.20)$$

where, in the simplest case, $I(\mathbf{u})$ is the experimental diffraction intensity set of a single domain and $\alpha$ is a scaling constant determined by the $\chi^2$ minimization (discussed in the next section). For the special case of R=0, Equation 2.20 is the general form of in-line holography where both sidebands are invertible. Essentially what we are doing is using the interference between known $\Psi(\mathbf{u})$ and unknown $w(\mathbf{u})$ in the diffraction plane to determine the phase. The Fourier transform of $w(\mathbf{u})$ is then an approximation of the residual wave, and candidate atomic locations can be determined by inspection. These new sites are incorporated in a dynamical $\chi^2$ TED minimization, and the procedure is repeated.

Although this formulation approaches a full solution, a more powerful method including measurement errors is required for final iterations. Extending Equation 2.20 to several domains and including the dynamical diffraction effects before the bottom surface, one can write a more accurate $\chi^2$ minimization form:

$$\chi^2 = \sum_n < (I_n(\mathbf{u})-\alpha_n|\Psi(\mathbf{u})+w(\mathbf{u})*T_n(\mathbf{u})|^2)^2/\sigma_n(\mathbf{u})^2 > \qquad (2.21)$$

where $I_n(\mathbf{u})$ are the intensities of domain n, $T_n(\mathbf{u})$ is the Fourier transform of the wave near the bottom of the sample just prior to the reconstructed layers, and $\sigma_n(\mathbf{u})$ are the intensity measurement errors. Convolving $w(\mathbf{u})$ by $T_n(\mathbf{u})$ adds the bulk effects to the residual wave. We determine $w(\mathbf{u})$ by minimizing $\chi^2$. This form is better, but does not include variations of the scaling constants $\alpha_n$ with $w(\mathbf{u})$. To handle these, we find the smallest possible $w(\mathbf{u})$ (minimum-norm solution) that gives a $\chi^2$ near one by minimizing $\langle w(\mathbf{u})^2 \rangle \exp(-\lambda\chi^2)$ with $\lambda$ an adjustable constant typically in the range 0.1-0.5, and then update the estimates of the scaling terms $\alpha_n$ periodically.

Random errors in the diffraction data sets appears as noise in the potential maps which limits the interpretability of weak sites. Also this method, just like direct phasing, cannot determine how much subsurface atoms relax. Hence neither technique can determine a truly complete solution but they have set the stage for a $\chi^2$ TED analysis.

### *2.5.5 $\chi^2$ TED Analysis*

The basic concepts of $\chi^2$ minimizations are well established, and we will only sketch some of the key points here. Consider a set of experimental intensities $I_e(\mathbf{g})$ for diffraction spots $\mathbf{g}$ and some calculated values $I_c(\mathbf{g})$. Assuming normal errors, the probability of these calculated values being correct is:

$$P = \prod_{\mathbf{g}} \exp(-[I_e(\mathbf{g})-I_c(\mathbf{g})]^2)/\sigma(\mathbf{g})^2) \qquad (2.22)$$

where $\sigma(g)$ is the standard deviation of the error distribution for a given diffracted beam. Maximizing the probability is equivalent to minimizing:

$$F = \sum_{g}[I_e(g)-I_c(g)]^2)/\sigma(g)^2 \qquad (2.23)$$

The reduced $\chi^2$ value is then defined as:

$$\chi^2 = F/(M-N) \qquad (2.24)$$

for M data points and N variables. A $\chi^2$ near one means the model is an adequate solution for the surface structure (not necessarily the correct one though), a value much less than one means the data is being overfitted by the model. a value much greater than one means the model is not correct, there is a serious error in simulating the diffraction pattern, or the data set errors were calculated improperly. $I_c(g)$ comes from a candidate model simulated in a full dynamical simulation including the bulk. A minimization routine (Dennis, Gay, and Welch 1981) is then used to predict better model parameters, the new simulated beam intensities are calculated and the process is repeated. To help the routine converge on a solution care should be taken to "parameterize" the model's free parameters correctly, so that the optimization moves cleanly toward the final solution, i. e., if an atom is likely to relax along the line x=y, the free parameters optimized should be the distance along x=y and the distance from x=y rather than x and y themselves.

At the start of the refinement process $\chi^2$ usually converges to a value in the stratosphere. Getting $\chi^2$ down can be tough, be patient, look for simulation mistakes, data set error mistakes, indexing mistakes, etc.... All possible sources of mistakes

should be checked before rejecting or massively changing a model. As one approaches reasonable $\chi^2$ values, manual data elimination is usually employed to eliminate beams excited by inelastic scattering (Kikuchi lines). Three or four beams per data set are typically excited in this way and should be removed from the set. Also remember a converged solution could still be unphysical and is still based on lattice averaged data. Once one solution is found, several other possible or related models must be checked objectively as well.

Of particular importance in comparing models is the error in the model parameters but for both of the systems studied, calculating model errors was a relatively meaningless exercise. In the 5x2 Au case it would have been too complex a problem and in the case of $\sqrt{3}$ Au the calculated parameter errors are simply a measure of the high static disorder of the structure. Still it is worth discussing the possible methods of obtaining the parameter errors. One standard procedure is to define an error matrix $E_{ij}$:

$$E_{ij} = fR^2/(M-N)H_{ij}^{-1} \tag{2.25}$$

where f depends upon the level of confidence desired, i.e. 0.5 for 68% confidence level, and $H_{ij}$ is the inverse of the second-derivative matrix. The (uncorrelated) error in any parameter can be taken as the $\sqrt{E_{ii}}$. However, this assumes that the minimum is parabolic in character. A more rigorous method which assumes less about the form of the minimum is to define $E_{ij}$ as the change in $x_i$, $x_j$ that leads to a change in the R-factor of $fR^2/(M-N)$. This makes no assumptions about the form of the minimum. Finally, the most rigorous method is to perform a Monte-Carlo simulation applying the

appropriate noise and determine the range of values $x_i$, $x_j$ and the corresponding R factor.

In practice, determining the error is not so simple for a dynamical calculation. The problem is that the calculation is numerical using a regularly spaced grid in both real and reciprocal space. As a consequence displacements smaller than the Nyquist critical frequency may be incorrectly modelled; this is restricted a little further to about 2/3 of the Nyquist frequency to avoid aliasing in the multislice algorithm. It is therefore difficult to evaluate the second derivative matrix correctly, but a search methodology appears to work quite well.

Numerous programs are available for performing such minimization given a subroutine to calculate the values of the residuals at any given point. We have used the program NL2SOL (Dennis, Gay, Welsch 1981) available as part of the public domain port library for the parameter error search as well as the $\chi^2$ refinement itself. This uses forward finite-differences for the differentials. It was necessary to include both a trap to ensure that the step size did not become too small, and an option to use central differences. The latter, although slower, found the minimum rather better.

### *2.5.6 Subsurface Relaxations*

In transmission mode the electron beam samples the entire crystal, and is only weakly sensitive to displacements along the beam direction. Displacing an atom just below the outermost surface is almost equivalent to displacing an atom further down the same distance. There is also a uniqueness issue as to whether the displacements

are physically reasonable versus simply inappropriate attempts to match experimental beam errors. More fundamentally, the subsurface relaxations must be accounted for properly: the typical depth of the reconstruction will, using St. Verdant's principle, be of the same order as the reconstructed unit cell in the x-y plane. Thus accurately simulating these subsurface displacements is an important part of modeling the structure. Two approaches can be used to obtain predicted subsurface strains. A Keating energy analysis (Keating 1966) is more correct but rapidly becomes computationally intensive with increasing surface unit cell size. The relaxation field or selvedge region can be obtained only slightly less accurately using an elastic strain field based on the experimental data. In this approach harmonic functions are matched to the surface symmetry and decay into the bulk. The wave vectors of these harmonic functions are then model parameters. (It is important to note that one should use a minimum number of harmonic functions to limit the number of model parameters.)

For inhomogeneous, isotropic elasticity the displacement field **D** must satisfy

$$(\lambda+\mu)\nabla\cdot\nabla^2\mathbf{D} + \mu\nabla^2\mathbf{D} = \mathbf{0} \tag{2.26}$$

Including the periodic character of the solution (reconstruction) in the x,y plane of the surface, a complete solution can be written as:

$$\mathbf{D} = A\nabla([z+\alpha]\omega) + B\nabla\omega + C\nabla x(\mathbf{n}\omega) \tag{2.27}$$

where $\omega$ is a harmonic function, **n** is the unit vector and A, B and C are constants (here x is curl). Using x and y in units of the unit cell, an appropriate form for $\omega$ is:

$$\omega = \exp(-2\pi q_z z)\exp(-2\pi i[q_x x+q_y y]) \tag{2.28}$$

with

$$q_z^2 = q_x^2 + q_y^2 \tag{2.29}$$

and

$$\alpha = 2(2-\upsilon) \tag{2.30}$$

This form has enough generality to model any subsurface displacements, and also has the correct physical form of decaying into the bulk of the material. The first two terms correspond to longitudinal displacements, the last one to a transverse or shear-type displacement field. Rather than using atomic positions as model parameters one can use the constants A, B and C, if required, with an appropriate choice of sin or cos terms to enforce symmetry requirements.

With precise enough data it should be possible to properly fit to this displacement field form, including the z component. In practice the z-component is very poorly constrained, and there generally are several solutions which differ only in the z-coordinates. For this reason we do not explicitly include the z-displacement in calculations; just a manual check to see they are reasonable. For some systems we have found that all the surface displacements including reordering reconstructions could be modelled by a strain field; an alternative is to use absolute atomic positions for the top layer and only model the subsurface strain field using these multilayer relaxations , as was done in the $\sqrt{3}$ Au case.

## 2.6 Setup of Room Temperature Gold Deposition Experiments

The Hitachi UHV-H9000 has two features which make deposition of gold while viewing the sample in the column possible. First, in the design of the UHV-

H9000 the region above the objective pole piece, designed to house a top loader cartridge transfer mechanism was converted to an empty surface science chamber. Second, a major portion of the pole piece bore is cone shaped allowing for a good view of the sample from various angles. These features allow for the installation of the metal deposition system above the sample shown in Figure 2.6 and detailed in

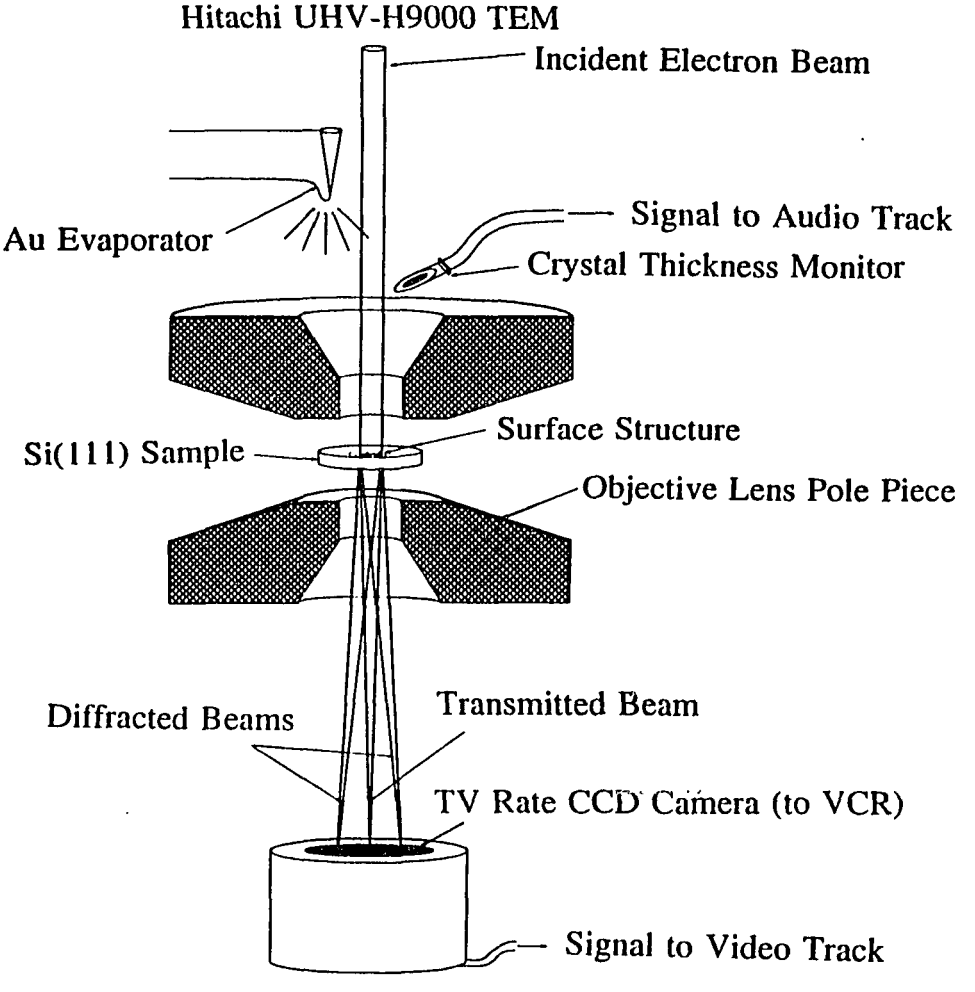


Figure 2.6. Schematic diagram of the room temperature gold deposition experimental setup.

Appendix B. To allow direct kinematical interpretation of the data, off-zone crystal tilt conditions were used as was discussed above. In the gold deposition studies the surface structure's TED pattern was recorded on Hi 8mm video tape. To provide accurate gold thickness calibration on the later deposition runs the audio signal from the quartz crystal thickness monitor was recorded on one of the video tape's audio tracks. Then to obtain the coverage versus time calibration, the beat frequencies on the audio track were measured providing accurate (2%) relative coverage measurements (Figure 2.7).

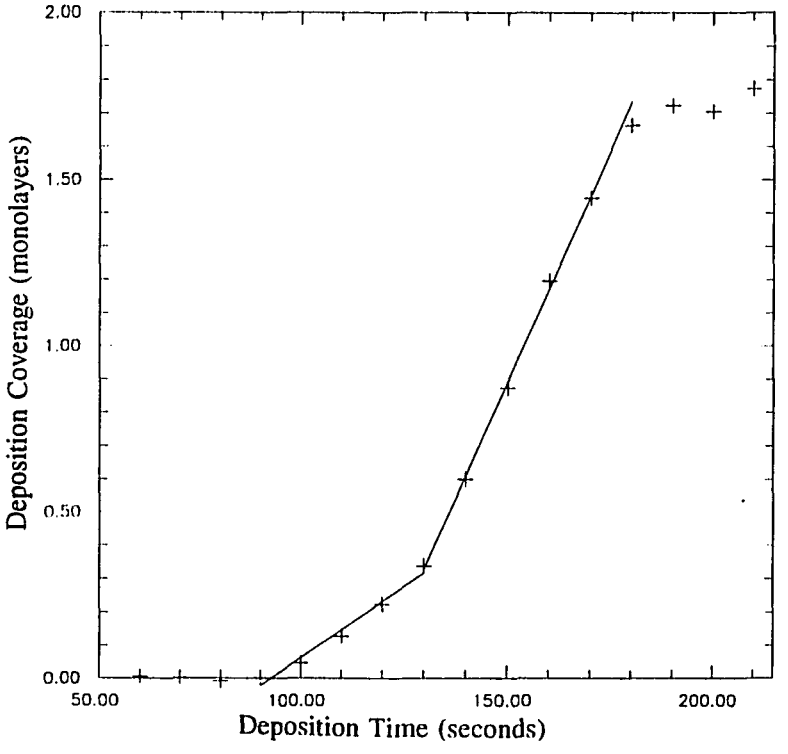


Figure 2.7. Plot of the deposited gold coverage versus deposition time for a typical room temperature deposition run.

Quantification of the diffraction intensities involved digitizing the tape images (summing one second worth of data) then implementing the cross-correlation technique discussed in Section 2.5.2 to obtain the final intensities (including a routine for rotational motif alignment).

# 3 CLEAN Si(111) SURFACE RECONSTRUCTIONS

## 3.1 Bulk Terminated Si(111)

Before discussing the gold induced surface reconstructions it is worthwhile to briefly look at the "native" Si(111) surface reconstructions. Given silicon's diamond type structure the "ideal" bulk terminated (111) surface (shown in Figure 3.1) is characterized by a silicon double layer, two sheets of silicon atoms 3.84 Å apart with p6 symmetry. These atomic sheets are 0.78 Å apart and offset by 2.21 Å which gives the surface p3m1 symmetry. Each upper atom of the top double layer has a dangling bond, the parallelogram formed by four of these is the smallest surface unit and is commonly referred to as the 1x1 surface unit cell. An ideal step on this surface would correspond to a double layer stopping on a set of down atoms with the next silicon double layer's up atoms 2.34 Å below. Finally experimental XRD studies (Robinson et al. 1988) as well as total energy calculations

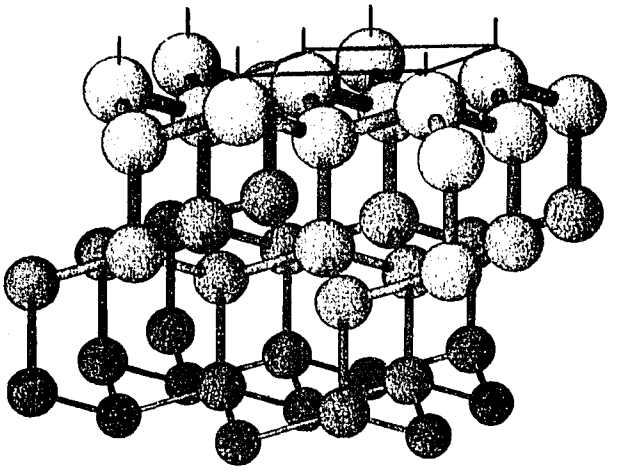

Figure 3.1. Schematic perspective view of the "ideally" terminated Si(111) surface, atoms closer to the surface are larger. The 1x1 unit cell is shown by the rectangle.

(Qian and Chadi 1987) show that since "over" silicon layers that would have been acting to compress the surface silicon double layer are missing, the Si(111) surface is under a net tensile stress.

## 3.2 Si(111)-(2x1)

The (111) orientation is the cleavage plane of silicon but because of the large number of dangling bonds the ideal bulk terminated Si(111) is energetically unfavorable. A more stable configuration, Si(111)-(2x1) or simply 2x1 is shown in Figure 3.2, a schematic of the generally accepted $\pi$ bonded chain model of Pandey (1981) which the surface assumes upon cleavage along (111) planes in UHV conditions. By breaking and then reforming one bond to the next lower silicon double layer, the top double layer rearranges to seven and five member ring combinations between these two double layers. This allows for the formation of chained pi bonds at the surface and thus lowers the number of dangling bonds significantly, but at the expense of increased strain energy. While this configuration is not thermodynamically the most stable, it is interesting to note that even at room temperature one Si-Si bond spontaneously breaks and reattaches elsewhere allowing the $\pi$ bond chain structure to form (Northrup and Cohen 1982).

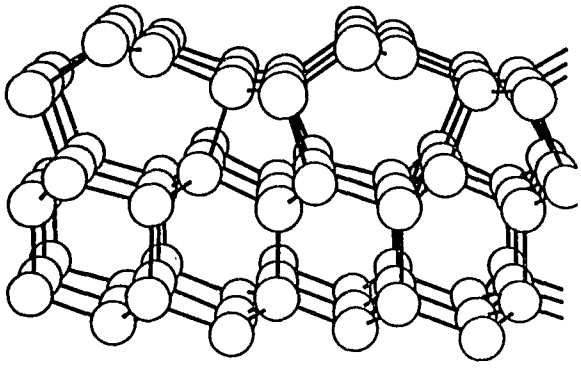

Figure 3.2. Perspective-view schematic of the Si(111)-(2x1) structure model (after LaFemina 1992).

## 3.3 The DAS Family of Structures

Several studies have shown that the 2x1 surface will convert to a structure with a surface periodicity of 5x5 above 350°C which will in turn convert to the thermodynamically stable 7x7 periodicity structure above 600°C (Feenstra and Lutz 1990, 1991 and references therein). The second irreversible transition is facilitated by increased silicon surface diffusion at elevated temperatures (Duke 1995). This is not surprising since the 7x7 structure has 102 silicon atoms in each unit cell that require reshuffling from the original surface.

As first described by Takayanagi et al. (1985) and confirmed by other studies (e.g., Robinson et al. 1988, Qian and Chadi 1987, Twesten and Gibson 1995), the 7x7 surface is found to consist of triangular stacking faults in the top most Si double layer amidst unfaulted regions. The faulted and unfaulted regions are joined by Si dimers and Si adatoms decorate the top surfaces of the faulted and unfaulted regions in a 2x2 periodicity (Figure 3.3). As Becker, Golovchenko, Higashi, and Swartzentruber (1985) have outlined and experimentally confirmed, by changing the size of the faulted region a family of dimer adatom

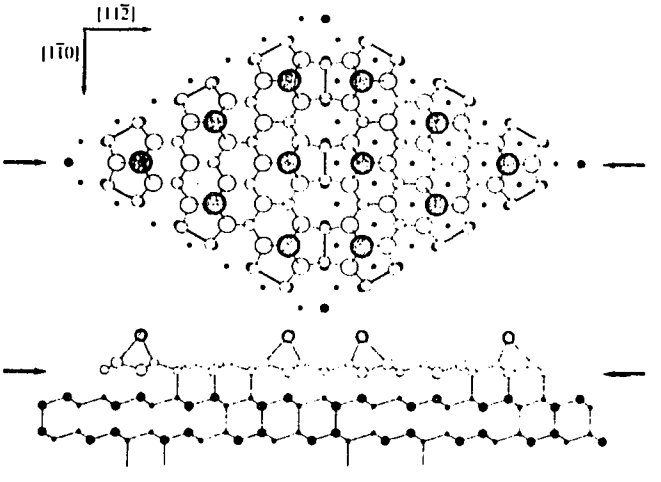


Figure 3.3. Top and side view schematics of the dimer adatom stacking fault model for the Si(111)-(7x7) surface (after Itoh et al. 1993).

stacking fault (DAS) structures is created, i.e. 3x3, 5x5, 7x7, 9x9, 11x11, etc..., of which the 5x5, 7x7, and 9x9 structures have been experimentally reproduced (Yang and Williams 1995a, 1995b) and 11x11 has been reported (Yang and Williams 1995a, 1995b). The detailed results of Yang and Williams indicate that which reconstructions will appear locally depends mainly on the immediate silicon concentration although arguments favoring the compensation of the Si(111) surface's tensile stress have also been put forward (Robinson et al. 1988).

### 3.4 High Temperature Si(111)-(1x1)

The technique Yang and Williams used to prepare the different metastable DAS phases was rapid quenching of a 1x1 periodicity surface from temperatures over 870°C, coupled with a short 650°C anneal if needed. The phase transition between this high temperature 1x1 and 7x7 is reversible and appears to be first order (Miki et al. 1992). This high temperature STM result is quite interesting in demonstrating that equilateral triangular sets of unit cells rapidly grow, briefly stabilize, and rapidly dissipate in the first order phase transition temperature range. A region with six complete 7x7 unit cells needs to be completed to nucleate a 7x7 domain. The atomic structure of the 1x1 phase has yet to be determined, but some authors (Feenstra and Lutz 1990, Yang and Williams 1995a) have speculated that it consists mainly of a disordered array of Si adatoms.

## 3.5 STM of Si(111)-(7x7)

Figure 3.4 shows a typical STM image of the 7x7 surface. Note that only the structures adatoms and corner holes are being strongly imaged. (Subtle feature height differences allow STM to distinguish between faulted and unfaulted regions) Despite imaging adatoms only, STM has been very useful in determining the structures of defects in the 7x7 surface such as steps (Becker, Golovchenko, McRae, and Swartzentruber 1985) and domain walls (Itoh et al. 1993 and references therein) when used in conjunction with the DAS model. These features will be important in the next chapter since they act as nucleation sites for the 5x2 Au structure. But as was noted in Section 3.3, the structure itself was solved using UHV-TED. The success of STM in determining surface structures is limited in these complex cases by the fact that it is only imaging the silicon adatoms, but given the DAS model, much can be surmised from the adatom locations.

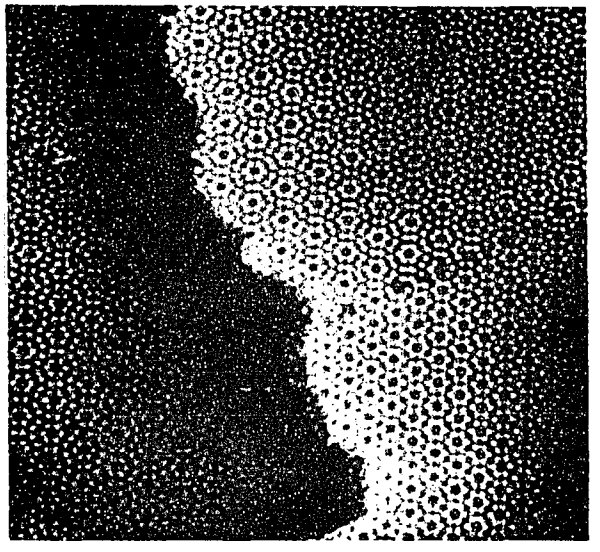

Figure 3.4. Typical STM image of the Si(111)-(7x7) surfaces along with a surface step and a Si(111)-(5x5) domain (after Yang and Williams 1994b).

## 3.6 TEM of Si(111)-(7x7)

In contrast to the now common STM images of 7x7, the noise filtered HREM

image of 7x7 in Figure 3.5 shows very different data. This image was obtained at the NEC Fundamental Research Laboratory by Drs. T. Ichihashi and S. Iijima (1994) and was digitized and transferred to Northwestern for image processing.

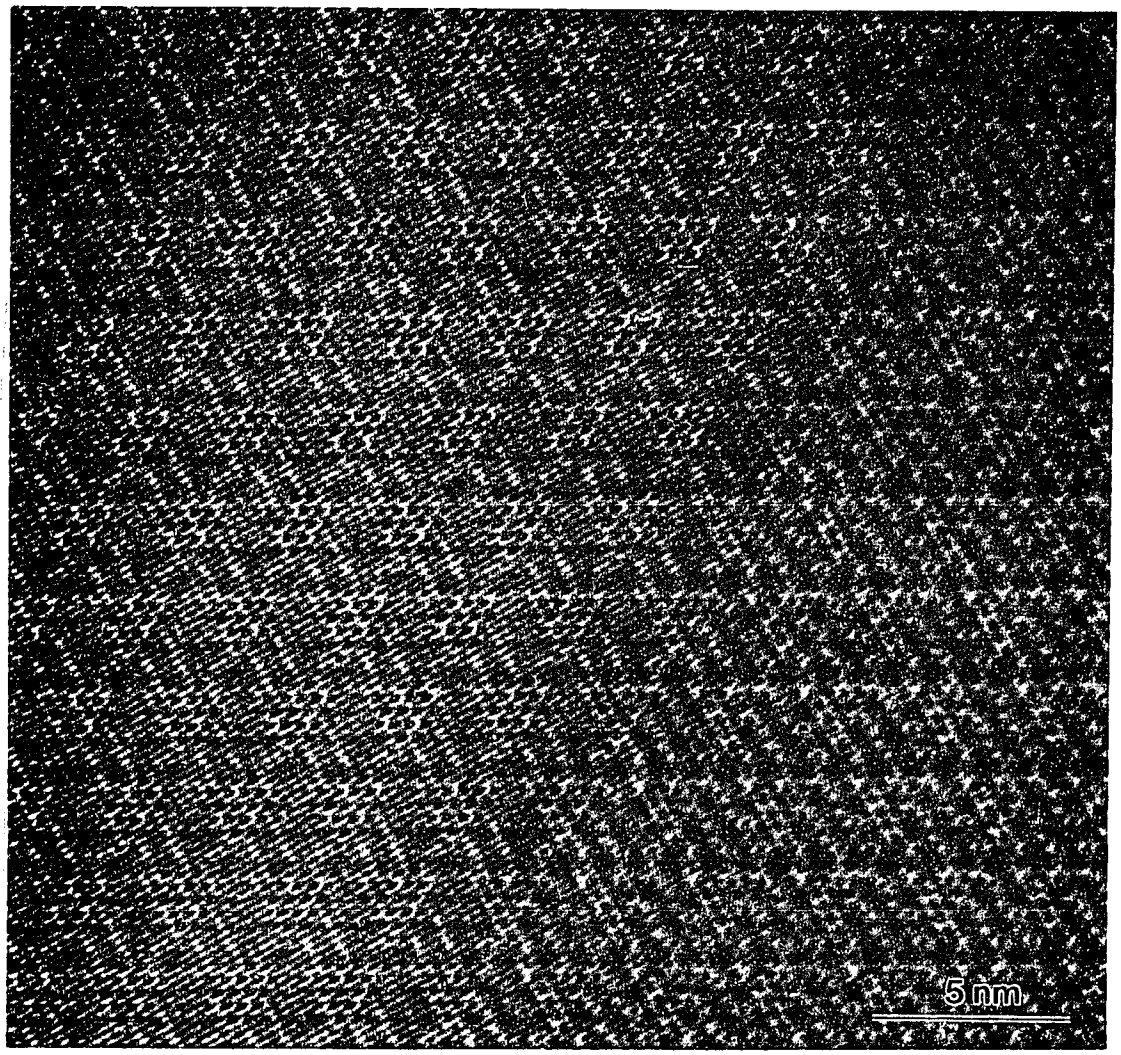


Figure 3.5. Noise filtered HREM image of a Si(111) sample with (7x7) reconstructed surfaces and a surface registry defect running upper right to lower left.

Aside from parametric Wiener noise filtering (Marks 1996) this image has not been modified from the original. While work on this image is in progress, much needs to

be done to fully interpret this and similar images (because of the overlap of the top and bottom surface structures and associated registry shifts). This image was included to illustrate the drastically different nature of HREM imaging versus STM imaging; this difference will be vital in the next chapter.

# 4 Si(111)-(5x2) Au

## 4.1 Introduction

In addition to the reasons mentioned for studying gold deposition on silicon in general, the 5x2 Au surface has several unique features which makes its detailed analysis especially worthwhile. The first feature is that, as discussed in Chapter 1 and along with the $\sqrt{3}$ Au structure, the 5x2 Au structure acts as a surfactant (Minoda et al. 1992) to facilitate almost perfect silicon homoepitaxy (Wilk et al. 1994). A second point of interest is the linear nature of 5x2 Au which clearly manifests itself in this surface's electronic structure (Collins et al. 1995). A full understanding of 5x2 Au's linear electronic nature could provide an avenue toward atomic scale device fabrication. A third aspect, likely related to the first, is that the 5x2 Au structure strongly affects the faceting of vicinal silicon surfaces close to the 111 facet. O'Mahony et al. (1994) have shown that with gold deposition and annealing, 4° miscut samples from (111) toward the (112) direction will form large terraces of 5x2 domains with protrusion (likely gold) decorated step bunches between them. Of even more interest, Seehofer and coworkers (1995) have recently identified gold induced reconstructed (775) and (995) facets which appear to have 5x2 Au like components. Both these results indicate the 5x2 Au atomic structure strongly effects the surface free energy of silicon. Given this motivation this chapter will look into the atomic structure of the 5x2 Au surface in detail.

### *4.1.1 Early Models of 5x2 Au*

First noted by Bishop and Riviere using LEED (1969) the surface structure in the gold coverage regime of 0.4-0.5 monolayers has a basic surface unit cell of 5x2.

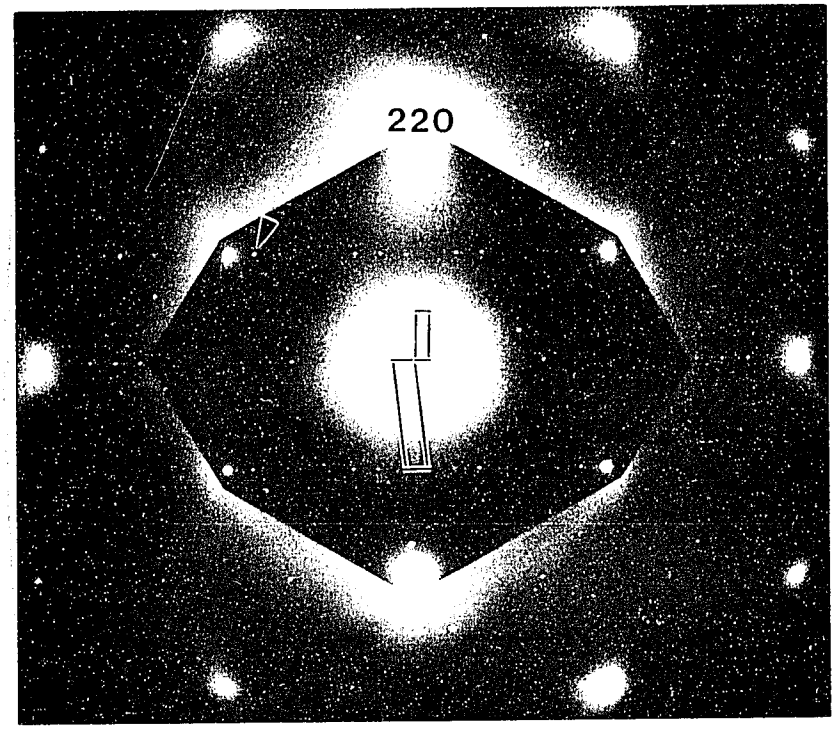


Figure 4.1. Transmission electron diffraction pattern from a region with predominantly a single domain of the Si (111)-(5x2) Au structure. This pattern was indexed in terms of a centered 10x2 unit cell (smaller rectangle), thus the arrowed strong surface beam is (h,k)=(-13,2). The larger parallelogram marks the primitive 5x1 unit cell. The x2 streaks are inherently weak near the transmitted beam.

To explain their LEED data Lipson and Singer (1974) proposed the three orientationally different domains. These domains are expected when a linear structure resides on a surface with p3 symmetry. They identified weak diffraction streaks which they correctly interpreted as arising from partially random, structure phase slippage from one row to the next row of the structure. Figure 4.1 shows a TED pattern of a single domain of 5x2 Au. If a c10x2 rectangular unit cell is defined, then (h,k) streaks

are seen for k=2n+1 and sharp diffraction spots for k=2n.

Early models (Lipson and Singer 1974, Lelay and Faurie 1977, Yabuuchi et al. 1983) for this surface contained two lines of gold atoms (Figure 4.2a) and were supported by ion scattering spectroscopy (ISS) (Huang and Williams 1988) and RHEED studies (Diamon et al. 1990). Few of these studies ventured to speculate where the silicon sites might be in this structure. To determine the height of the gold in the surface structure an X-ray standing wave study (Berman, Batterman, and Blakely, 1988) as well as ISS studies were done (Yabuuchi et al. 1983, Huang and Williams 1988). The XSW study and the first ISS study found the gold is within the

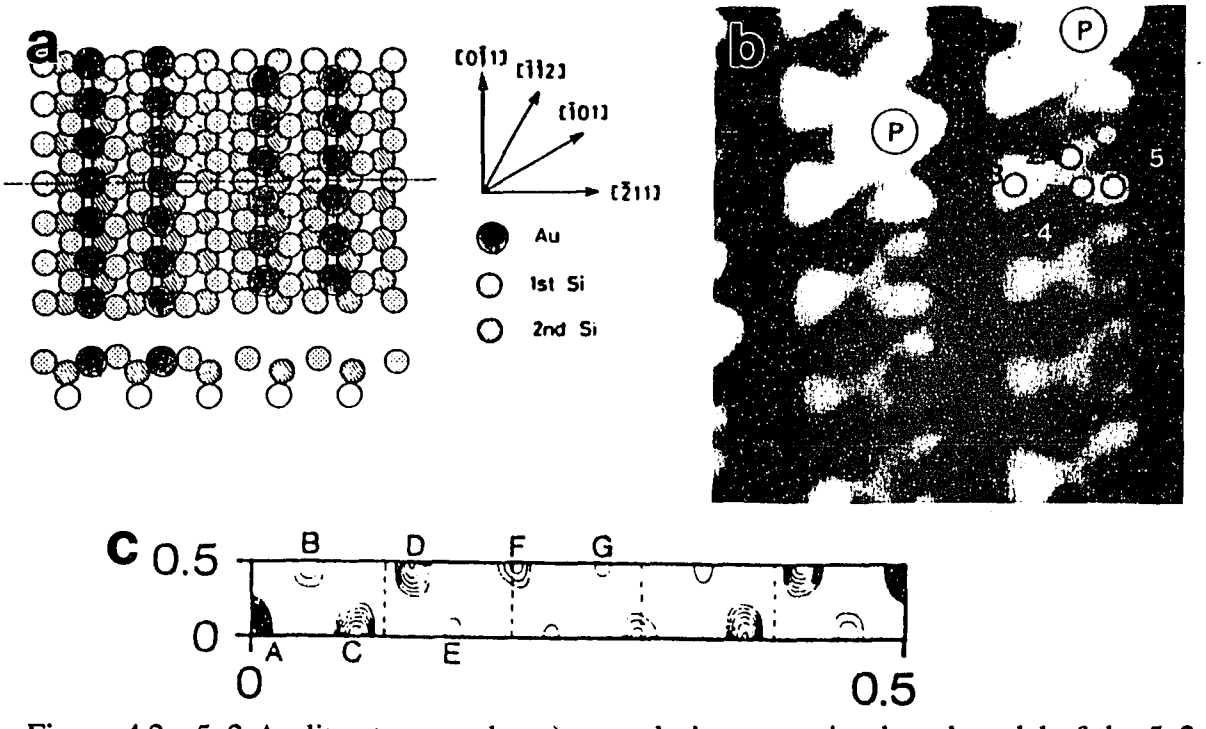


Figure 4.2. 5x2 Au literature results, a) an early ion scattering based model of the 5x2 Au surface where gold atoms are dark (after Yabuuchi et al. 1983), b) high resolution STM image of 5x2 Au (after O'Mahony et al. 1992), and c) surface X-ray Patterson function of 5x2 Au where more contours represent increasing function value (after Schamper et al. 1991).

first silicon double layer, while another ISS study found the gold 0.7 Å above the outermost Si layer.

### *4.1.2 The Apparent STM / X-ray Conflict*

Not long after the advent of STM the technique was applied to study the 5x2 Au surface. These studies (Hasegawa et al. 1990, Baski, Nogami, and Quate 1990, O'Mahony et al. 1992), however, appeared to contradict the early two gold row models, showing a more complicated structure with a feature shaped like a "Y" and an irregular decoration of protrusions (Figure 4.2b). Several authors (Baski, Nogami, and Quate 1990, O'Mahony et al. 1994) have noted that there are too many STM features for all of them to be gold atoms, the coverage of which cannot be more than 0.5 ML (Bauer 1991). To complicate the matter an X-ray diffraction study failed to give clean locations for the gold atoms since its Patterson function showed sites with apparently varying atomic density (Figure 4.2c). This result was fitted by a disordered structure model with partial occupancies (Schamper et al. 1991). However, STM images, the X-ray standing wave analysis (Berman, Batterman, and Blakely 1988), and transmission electron diffraction patterns (Takahashi, Tanishiro, and Takayanagi 1991) did not show high disorder (aside from the inherent phase slippage, since there is no strong background diffuse scattering). With this state of affairs we applied UHV-TEM techniques to the study of this surface.

## 4.2 HREM Results

As was discussed in more detail in Chapter 2, silicon (111) samples were prepared by a combination of ex-situ thinning and in-situ sputter/anneal cycles. Approximately half a monolayer of gold was deposited onto the surface and lightly electron beam annealed at about 550°C (±50°C). (Reannealing or cleaning cycles followed by repeated gold deposition and annealing to reproduce the structure were performed many times over a period of about one month.)

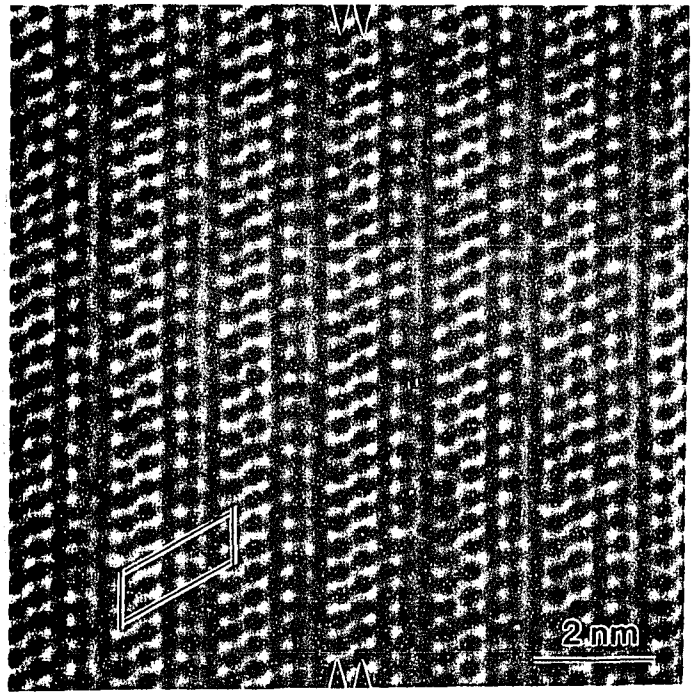


Figure 4.3. Near Schertzer defocus, noise filtered, off-zone HREM image of the Si (111)-(5x2) Au surface. Clearly visible are two (arrowed) rows of dark features which correspond to gold atoms. The unit cell is outlined.

These samples were examined using the UHV-H9000 by off-zone HREM at 250kV with the gold on the top surface to minimize electron beam damage. HREM images from four different regions of a focal series of nine members were analyzed after digitization; all 36 images were 1024x1024 pixels in size. Noise reduction was performed using the modified parametric Wiener filter discussed in Section 2.4.2.

Figure 4.3 shows a near Schertzer defocus image where atoms appear black.

Two lines of strong scattering features can be seen running along the [01] direction, which can unconditionally be identified as the gold atoms due to their strong scattering, confirming conclusively the earlier two gold row models. There are also a number of not well resolved weaker features due to silicon atoms. In this image the presence of a twofold periodicity is difficult to see, it is more apparent in other members of the focal series. The spacing between the gold atoms in this image is close to 3.84 Å, the Si 1x1 spacing. This result is confirmed by off-zone TED data since the 1x1 spots are always stronger than any of the surface superstructure spots, independent of crystal tilt. This fact explains why the X-ray diffraction results were difficult to interpret properly; the strongest surface diffraction spot is coincident with a bulk spot and its forced exclusion leaves a large gap in the data set.

### 4.3 TED Based 5x2 Au Model

Although the HREM images clearly identify two rows of gold atoms, the structure has to be more complicated than this, as the weaker features in Figure 4.3 show. Also, the diffraction pattern is very inhomogeneous; for instance, in Figure 4.1 the (13,2) type spot is the strongest pure surface spot while (11,2) is quite weak. This diffraction feature requires a large number of silicon sites to counteract the simple gold structure's scattering distribution.

For the diffraction analysis two different orientations were used, one containing three domains while the other contained >90% of a single domain. The data quantification techniques discussed in Chapter 2 were used to prepare three data

sets with 275, 268, and 310 beams each from a first sample region. This first data set came from a region 18.8 nm thick tilted 45 mrad from the (111) zone. Only beams between 0.3 and 2.5 $Å^{-1}$ and those of the 5x1 sublattice were included in the data set. From a second region (with a tilt of 71 mrad and a thickness of 37.6 nm) 648 beams were collected.

Even with the gold atomic locations, no starting model would converge in the $\chi^2$ analysis, hence heavy atom holography (Marks and Plass 1995), Section 2.5.4, was employed to iteratively identify the silicon sites from the diffraction data. The $\chi^2$ analysis then refined the atomic positions to obtain the final model. To reduce complexity and partially parameterize the model to help it converge faster (as discussed in Chapter 2) a y-axis mirror was included in the model in the half cell $0<y<0.5$ with a translational symmetry of (0.25,0.5). Lifting this mirror symmetry had only a small effect on the final results.

The final result of using this heavy-atom holography plus full dynamical $\chi^2$ minimization approach is shown in Figure 4.4; the x-y plane atom positions are listed in Table 4.1. The $\chi^2$ of this model, when using all the experimental data, was 3.6; using just the first three domains, it was 2.6. This $\chi^2$ is for a structure with no subsurface relaxations. Including these subsurface relaxations is possible, and for most surface structures necessary; however, here the experimental beam intensity errors in combination with the size and complexity of the surface unit cell make the usefulness of such a calculation doubtful. The inherent phase slippage of the structure was included in the analysis by introducing twin structure domains, as discussed by Bauer

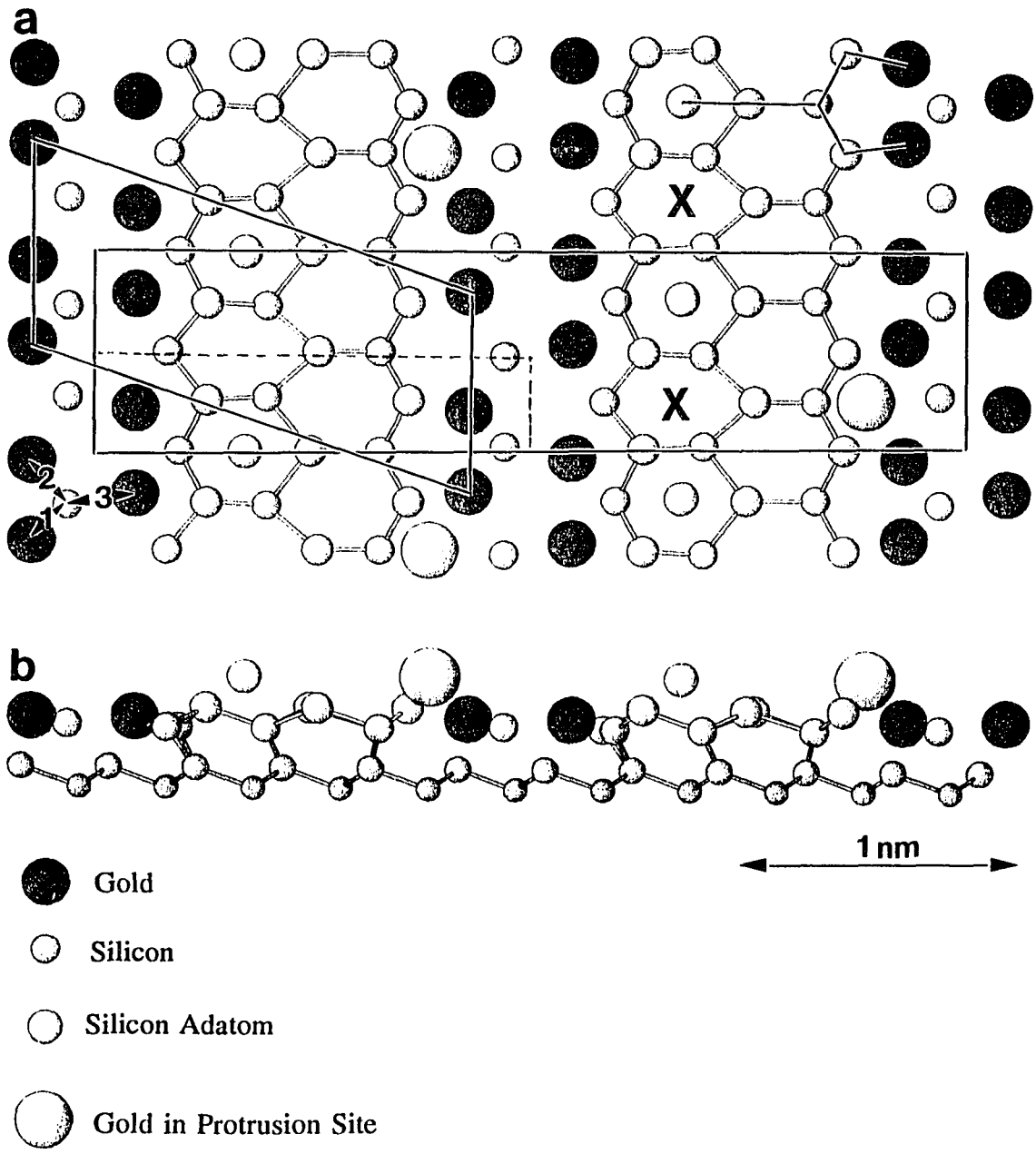


Figure 4.4. a) Top view of the Si (111)-(5x2) Au atomic structure with the unit cell and a "Y" like feature shown. An alternate set of Si adatoms sites are marked by "X"s and the most probable type of site for the STM protrusions are shown with light gold atoms. b) Side view of the structure. The parallelogram indicates the primitive 5x2 unit cell, the rectangle the c10x2 cell with the dashed 5x1 subcell corresponding to the atom positions in table 4.1. The gold atomic heights are taken from Berman, Batterman and Blakely (1988) and the silicon adatom heights are arbitrary. (No relaxations of the second silicon double layer were included in the calculation).

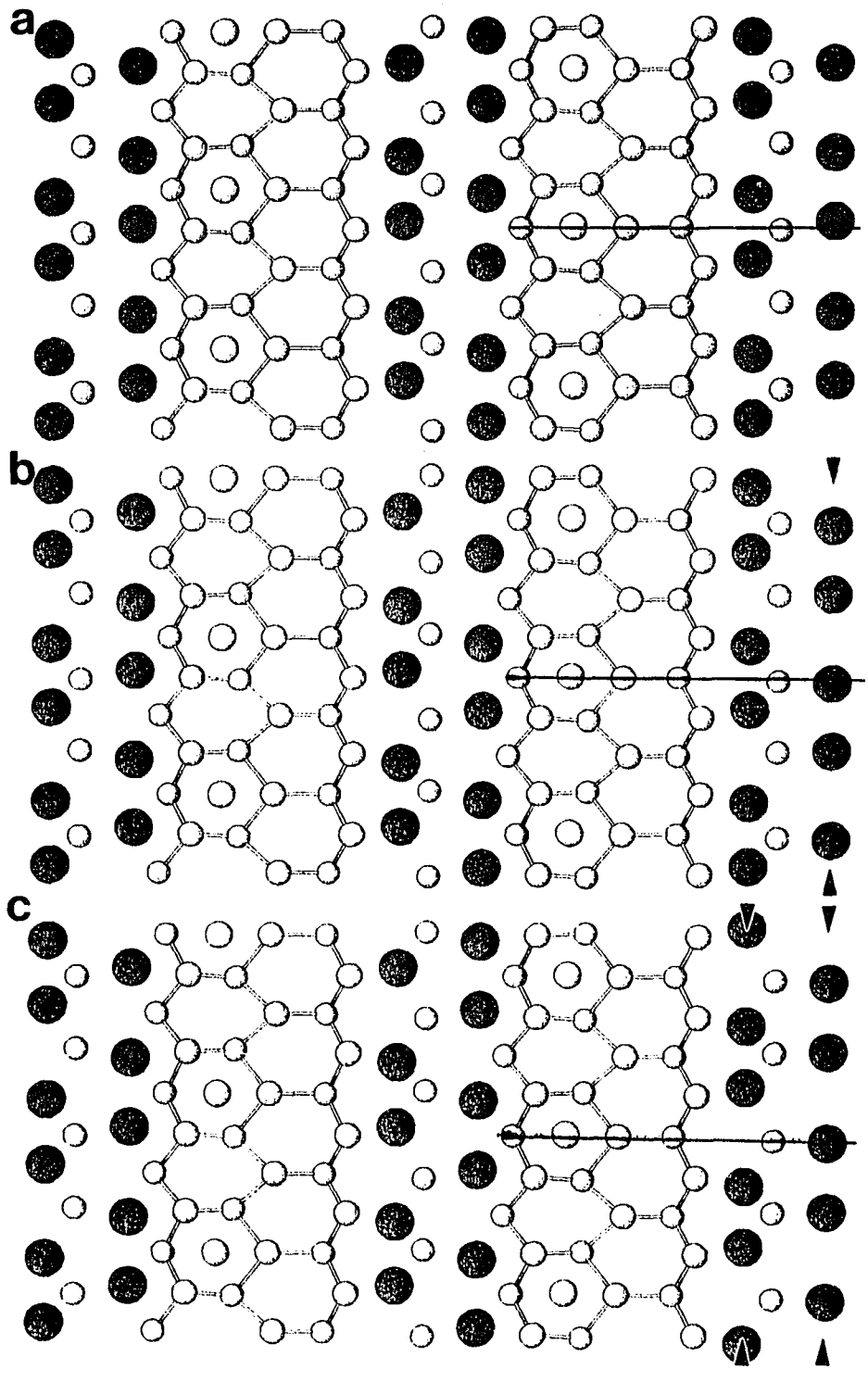


Figure 4.5. Top view schematic diagrams of how different gold atoms' "bunching up" along the rows can convert a pristine 5x2 Au structure; a) to one with a twin; b) with one row bunching change or to a complete phase shift; c) with two row changes as alluded to by Bauer (1991). Arrows indicate which gold rows have changed.

Table 4.1
Si (111)-(5x2) Au atomic positions

| Type | Site | Atoms | x [±0.003] | y [±0.013] | z [inf.] |
|---|---|---|---|---|---|
| Si | 2c | 2* | 0.188 | 0.002 | Layer 1 |
| Si | 2c | 4 | 0.375 | 0.256 | Layer 2 |
| Si | 1a | 2 | 0.263 | 0.000 | Layer 2 |
| Si | 1b | 2 | 0.272 | 0.500 | Layer 2 |
| Si | 2c | 4 | 0.144 | 0.258 | Layer 2 |
| Au | 2c | 4 | 0.063 | 0.216 | Layer 3 |
| Au | 2c | 4 | 0.445 | 0.203 | Layer 3 |
| Si | 2c | 4 | 0.985 | 0.273 | Layer 3 |
| Si | 2c | 4 | 0.213 | 0.272 | Layer 4 |
| Si | 1a | 2 | 0.113 | 0.000 | Layer 4 |
| Si | 1b | 2 | 0.100 | 0.500 | Layer 4 |
| Si | 1a | 2 | 0.343 | 0.000 | Layer 4 |
| Si | 1b | 2 | 0.343 | 0.500 | Layer 4 |

* Si adatom site with half occupancy

Plane group p1m1 with a (0.5,±0.25) translational element for a c(10x2) surface unit cell: a = 33.252 Å , b = 7.679 Å. Atoms refers to the total number of atoms of that site type in the c10x2 unit cell, x and y values are in fractions of a unit cell, z direction layer positions are inferred.

(1991), into the $\chi^2$ fitting. These are shown in Figure 4.5. The TED model has recently been confirmed using direct phasing techniques (Marks, Plass, and Dorset 1996).

Besides the subsurface relaxation, two additional ambiguities still exist in the TED model. First, since TED is only strongly sensitive to the atomic locations in the surface plane, the z (height) locations are inferred. Second, since the data is restricted

to reflections from the 5x1 subcell (i.e. omitting the streak intensities), all the positions can be shifted by (0.5,0) without significantly changing the $\chi^2$ value. The configuration that we have chosen best matches the HREM images.

The final model we have obtained appears to essentially be a gold-silicon double layer structure acting as the center of a surface dislocation.

### *4.3.1 Comparison with Current Models*

First of all it is interesting to note that the expanded silicon double layer portion of the TED model bears striking resemblance to two other atomic structures, namely the $\pi$-bonded chain model of Si(111)-(2x1) (Pandey 1981) and to the narrow strip (or "partial 7x7") portion of the structure proposed for the vicinal (h,h,m) surface (h=1, m=1.4 to 1.5) by Suzuki and coworkers (1996). That the similar 2x1 structure (Figure 3.1) contains extended chains of $\pi$ bonds could help explain the "Y" features seen by STM for the 5x2 Au surface. That is, the 2x1 $\pi$-bond has features within it as seen by STM (e.g., Feenstra and Lutz 1991). If the silicon adatom is interpreted as the bottom feature of the STM "Y" then the "Y" in Figure 4.4 would be the only set of sites which could correspond to the STM features.

Our 5x2 Au structure appears to match all the available experimental evidence quite well. On the level of visual comparison, the TED based Patterson function map is identical to the one determined by X-ray diffraction. In the 5x2 Au model the gold atoms sit within the outermost silicon double layer slightly displaced from bulk lattice sites, in agreement with the X-ray standing wave data and ISS. Silicon atoms appear

between the two gold rows with gold-silicon spacings similar to the missing top layer structures proposed for the Si(111)-($\sqrt{3}$x$\sqrt{3}$)R30° Au surface which will be discussed in the next chapter.

A quantitative comparison to other models is impossible since, to date, all other models for 5x2 Au (except the flawed X-ray diffraction analysis) have been qualitative in nature. These models are based on ICISS data (Huang and Williams 1988), ISS (Yabuuchi et al. 1983), XRD (Schamper et al. 1991), XSW (Berman, Batterman, and Blakely 1988), LEEM (Bauer 1991), RHEED and Li adsorption (Diamon et al. 1990), and STM (Hasegawa, Hosaka, and Hosoki 1996). Of these only the STM and XRD models propose silicon positions significantly different from bulk sites. As was earlier discussed, Schamper's X-ray interpretation has serious flaws and can be excluded from consideration. The remaining models can be classified into two categories based on the spacing between the two gold rows. The XSW, ISS, ICSS, STM, and one of the RHEED models have spacings between adjacent gold rows of 2 and 3 1x1 unit cells along (110) (as seen in Figure 4.2a) while the TED and LEEM models and the other RHEED model have spacings of 1 and 4 1x1 unit cells. Figure 4.3 conclusively shows that only models in the second, 1 and 4, category can be correct. Bauer's LEEM based model does not contain two full atomic rows and was only meant to illustrate the gold "bunching" effect that is the essential reason why the structure has 5x2 instead of 5x1 periodicity. Daimon's et al. RHEED based model has the correct row spacing and shows the correct minimum spacing between gold protrusions forming a fifth, partially occupied Au site, although it is essentially 5x1. The STM

based model of Hasegawa is worth mentioning in that it displays the expected bunching of gold atoms along the two fold direction and assigns silicon sites based on the high resolution STM results of O'Mahony and coworkers.

In comparing the TED model to other literature models a useful parameter to employ is the silicon surface density. Silicon surface density is defined as the number of surface structure silicon atoms per 1x1 unit cell where surface structure means only the top double layer and above. (This can be regarded as the silicon equivalent of the gold coverage.) For example, an ideally terminated (111) surface would have a silicon surface density of 2.0, 7x7's density is 2.08, 5x5's is 2.00, and the quenched 1x1 surface has a measured density between 2.20 and 2.22 (Yang and Williams 1994a, 1994b). A $\sqrt{3}$ Au surface ideally has a silicon density of 1.00 but with silicon replacing gold in domain walls, this value can vary between 1.13 and 1.16. REM and STM studies indicate that the silicon density is significantly lower in 5x2 Au than in 7x7: 1.1 to 1.3 (Tansihiro and Takayanagi 1989, Hasegawa, Hosaka, and Hosoki 1992). Our proposed model has a silicon surface density of 1.5 while Hasegawa's model has a density of 1.3. Most early models had rather high silicon surface densities, i.e., for the ISS model the silicon density is 2, for the XSW model, Si density is 1.6.

### *4.3.2 STM Protrusions*

Features common to all the STM 5x2 Au results (and conspicuously absent from Figure 4.3) are irregularly spaced clear protrusion running along the five fold

direction with a minimum spacing between them of 4 1x1 unit cells. The possible locations of these protrusions within our 5x2 Au model are shown by the large white gold atoms in Figure 4.4 although including a partially occupied gold site at this location did not affect the $\chi^2$ value significantly. RHEED studies and the behavior of these protrusions with domain growth strongly suggests that they are loosely bound gold atoms (Diamon et al. 1990, Hasegawa, Hosaka, Hosoki 1996). Baski, Nogami, and Quate (1990), Seehofer et al. (1995), and Yagi, Kakitani, and Yoshimori (1996) (based on T. Hasegawa's STM images) have found the density of these protrusions stays constant (0.32±0.02, 0.275±0.015, and 0.27 per 5x2 unit cell respectively) with increasing gold coverage but O'Mahony et al. (1994) found the density increases with increasing coverage. This discrepancy in the STM results may be due to the much longer domains prepared by O'Mahony and coworkers through vicinally cut samples. Much longer domains along the twofold direction would reduce "excess" gold's possible tendency to accumulate at domain boundaries. Based on STM images from T. Hasegawa and a straight forward model assuming repulsive interactions among the protrusions (Hasegawa, Hosaka, and Hosoki 1996), Yagi, Kakitani, and Yoshimori (1996) have been able to determine the correlation function of the protrusions with each other (both along one row and from row to row) with very good agree to experimental data.

With this feature so obvious in STM images why does it seem that there is no evidence of it in HREM images and hardly any in the TED data? While we initially speculated that the lack of strong scattering features corresponding to the protrusions

might be due to sample preparation differences (Marks and Plass, 1995), it has become clear from discussions with Dr. Hasegawa that, more likely, the electron beam is causing the protrusions to vibrate strongly or move during beam exposure. In high temperature STM experiments Hasegawa (private communication) has noted that the protrusions begin to move from one site to the next at temperatures as low as 200°C and move so rapidly above 300°C that they appear as a bright band. While it has been calculated that a 300kV electron beam only heats the sample by 50°C at most, the well known effect of momentum transfer perpendicular to the beam could, in HREM, cause the protrusions to strongly vibrate or move in a manner similar to the STM study. Yet, evidence of this movement should be more evident in the $\chi^2$ analysis which still leaves the possibility that the protrusions are related to sample preparation.

## 4.4 Registry, Surface Domain Walls, and Stacking Fault Interactions

It can be seen from the work of Itoh and coworkers (1993) that a good approach to understanding how the elements of a structure as complex as 7x7 work together is to study the structure of its domain boundaries. Domain boundaries in 7x7 arise because domains nucleate with different registries with respect to each other. How the structure accommodates these 1-D mismatches reveals a lot about what holds the pristine structure together. For instance, in studying 7x7 domain boundaries Itoh et al. have found that the dimer rows are not as important as previously suspected and that the corner holes play a more important role. In principle the same approach can be applied to 5x2 Au if the relation between the STM "Y" feature and the atomic

structure can be determined. However, for 5x2 Au this field is not as well developed.

Based on unit cell and symmetry considerations the possible registry shifts of 5x2 Au can easily be predicted independent of a specific atomic model. Since the structure can have three different rotational orientations we can group the registry shifts into four categories, shown in Figure 4.6. If the domains have their five fold directions aligned, we will call these 0° boundaries. There are two subcategories within this category which depend on whether the domains are positioned side to side or top to bottom in relation to their rows. (The second subcategory is very rare because of the strong growth anisotropy of the structure.) Tanishiro and Takayanagi (1989) call the first subcategory out of phase boundaries and have found they also are relatively rare. The second domain boundary category arises when the twofold edge of one domain comes up against, or "rams" a fivefold row of another at a 60° angle. Hasegawa and coworkers (1996) have found that these second category boundaries tend to be unstable at elevated temperatures because of the higher growth rate of the two fold direction; the "ramming" domain will tend to eat into and eventually consume the other domain.

The last two types of domains arise when the two fold directions intersect at either 60° or 120°. Depending on annealing temperature, these domain boundaries tend to be the most stable and several examples of these as well as the ramming type boundary are visible in Figure 4.7a; a bright field image of a 5x2 Au surface that was annealed for a fairly short time leading to small 5x2 Au domains. Figure 4.7b, c, and d show a sample of Hasegawa's high temperature STM domain boundary images.

For each of the stable domain boundaries (for simplicity, we assume a 5x1 unit cell since the changes along the twofold direction are relatively minor) there will also be five possible alignments as one domain "slides" past the other along the boundary.

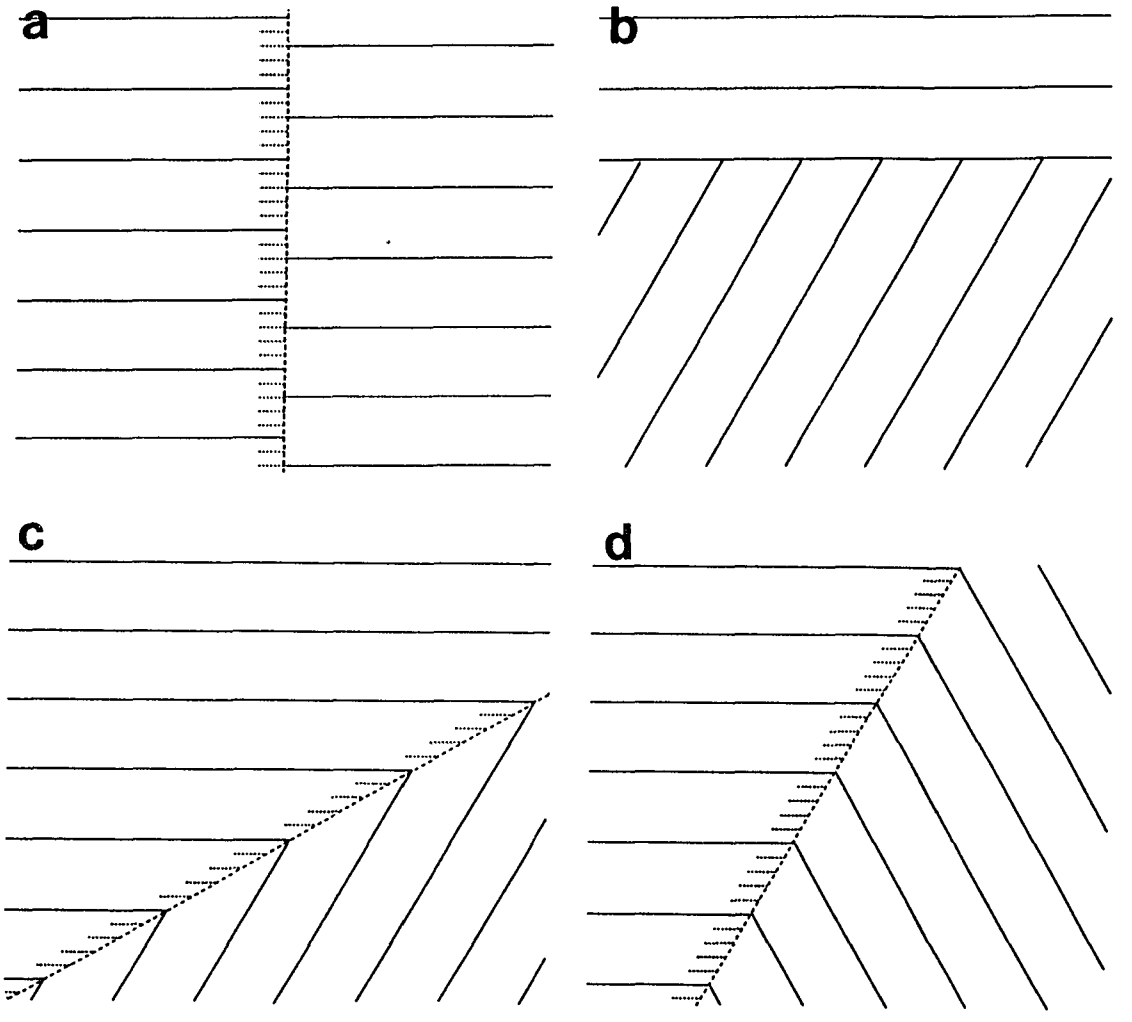


Figure 4.6. Schematic illustration of the four categories of 5x2 Au domain walls possible: a) both domains have their fivefold directions (shown by lines) aligned, b) the twofold direction of one domain "rams" a single row of the other domain, c) the fivefold directions of two domains intersect at 60°, and d) the fivefold directions intersect at 120°. The short dashed lines in a), c) and d) indicate possible registry shifts of one domain along the boundary. a) illustrates an asymmetric boundary while c) and d) illustrate symmetric ones.

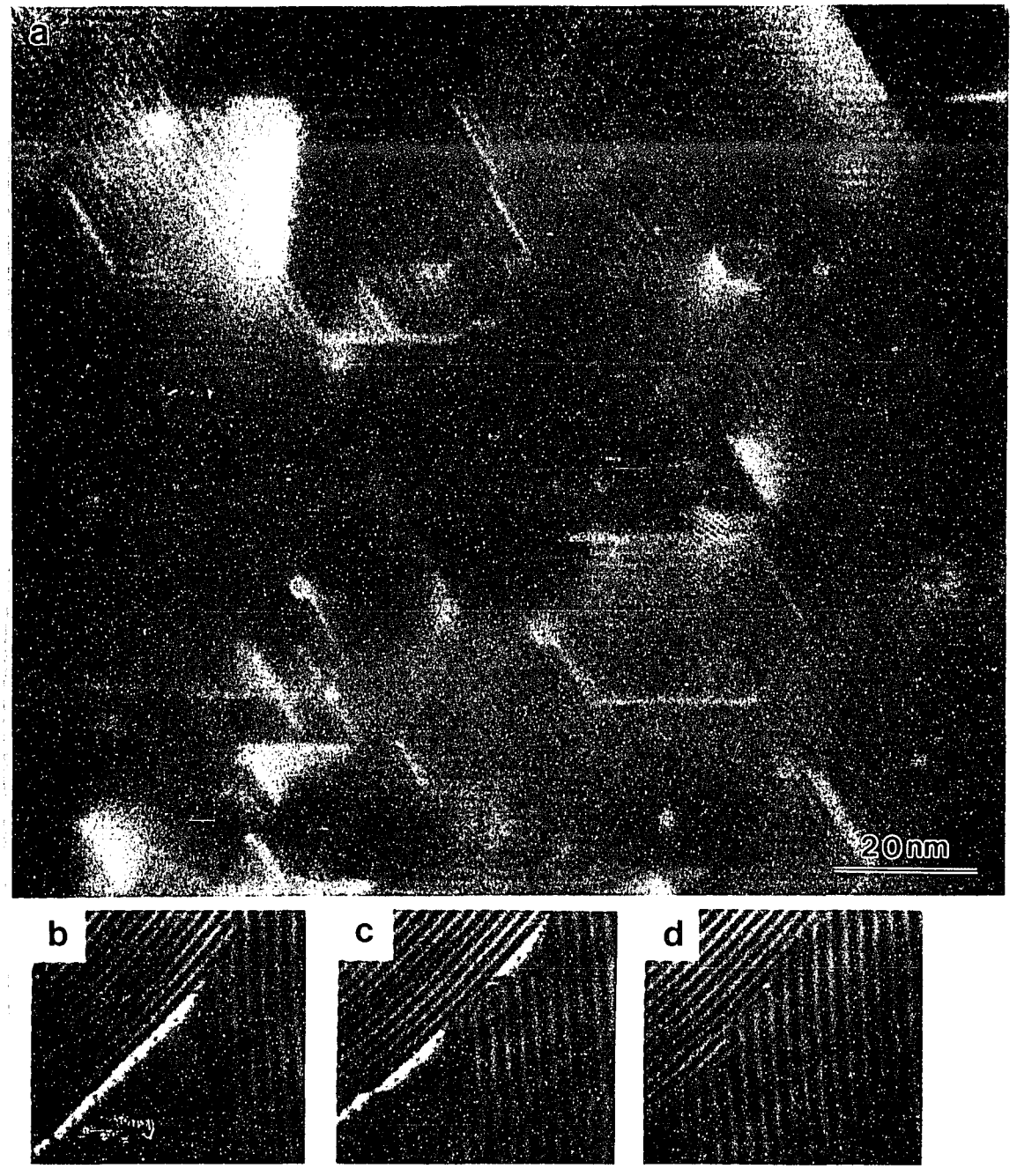


Figure 4.7. a) Bright field TEM image of a 5x2 Au surface with small 5x2 Au domains visible by the 11 Å spacing fringes. Numerous 5x2 Au domain boundaries are visible as well as subsurface stacking faults. b), c), and d) High temperature STM images of 5x2 Au domain boundaries (after Hasegawa, Hosaka, and Hosoki 1992).

One registry will lead to a symmetric boundary and of the other four, two will just be the mirror images of the other two. Thus there can be a total of 6 unique atomic configurations for the 60° and 120° category boundaries. By a similar analysis the 0° boundary can have six unique possible atomic configurations (two for the side to side subcategory, four for the top to bottom subcategory) and the "ramming" boundary can have four configurations (although only one is expected to be stable) giving a total of sixteen possible atomic boundary configurations which need to be determined.

Because of the possibility of electron beam damage (which seems to be more prevalent near the domain boundaries) and because of limited resolution, bright field TEM imaging is not the ideal choice of techniques to carry out this type of study. Still, it is worthwhile to note in Figure 4.7a that if one projects the 5x2 Au fringes to the domain boundaries for the 60° and 120° boundaries they tend to be symmetric more often than not (the ramming boundaries are more common). Only two STM images of 5x2 Au 60° boundaries have been published (Hasegawa, Hosaka, and Hosoki 1992), Figure 4.7b and d. Both seem to be symmetric but because of limited resolution the evidence is not conclusive. These STM images show a "microfacetted" pattern of 5x2 cell wide, symmetric and ramming boundaries. This pattern forms in order to match the mesoscopic angle of the domain boundary.

Given the limited resolution of both sets of images, the evidence for predominance of symmetric domain walls is admittedly weak. Still, if symmetric boundaries are favored over asymmetric ones, then the gold-silicon and silicon-silicon portions of the structure prefer to bond only with their counterparts across the

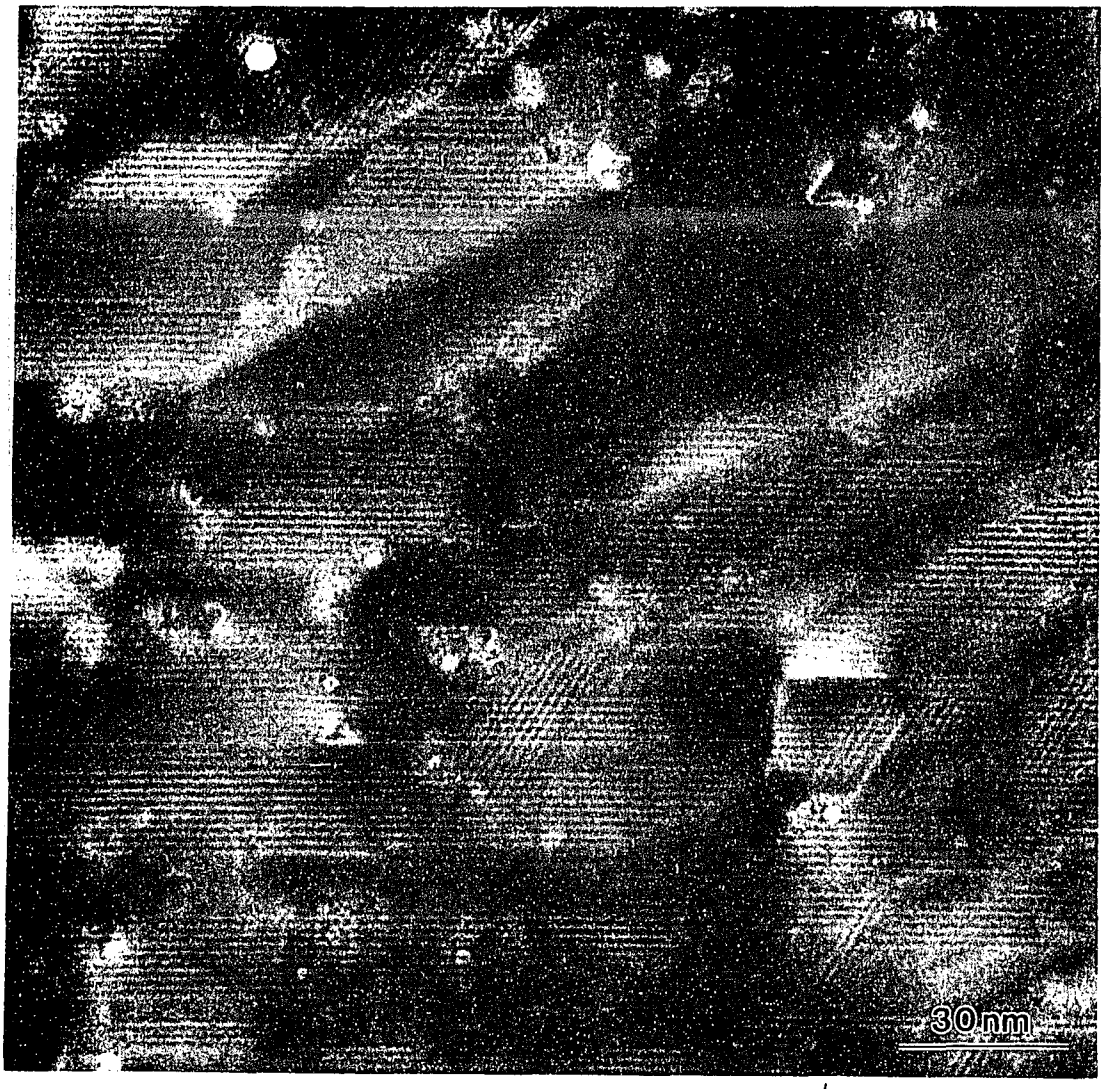


Figure 4.8. Bright field image of a sample with 5x2 Au and √3 Au on both surfaces (the 6.6 Å √3 Au fringes are barely visible). The large intensity changes between regions with curved boundaries indicate regions with different step heights.

boundary. It should be noted that a local asymmetric intersection can change to a symmetric one, and vice versa, by the rows simply lengthening or shrinking by one or two 5x1 units thus changing the position of the boundary. Symmetric boundaries also explain why the 0° category, out of phase boundaries, which are by definition asymmetric, tend to be rare. One domain will tend to eliminate the other in dynamic

domain growth and hence get rid of the unfavorable boundary.

Finally from Figure 4.7a we can also see that the 5x2 Au structure is apparently unaffected by the presence of subsurface stacking faults. From Figure 4.8 it is apparent that the 5x2 Au domains run right up to the step edges in agreement with STM results (O'Mahony et al. 1994).

## 4.5 Room Temperature Gold Deposition

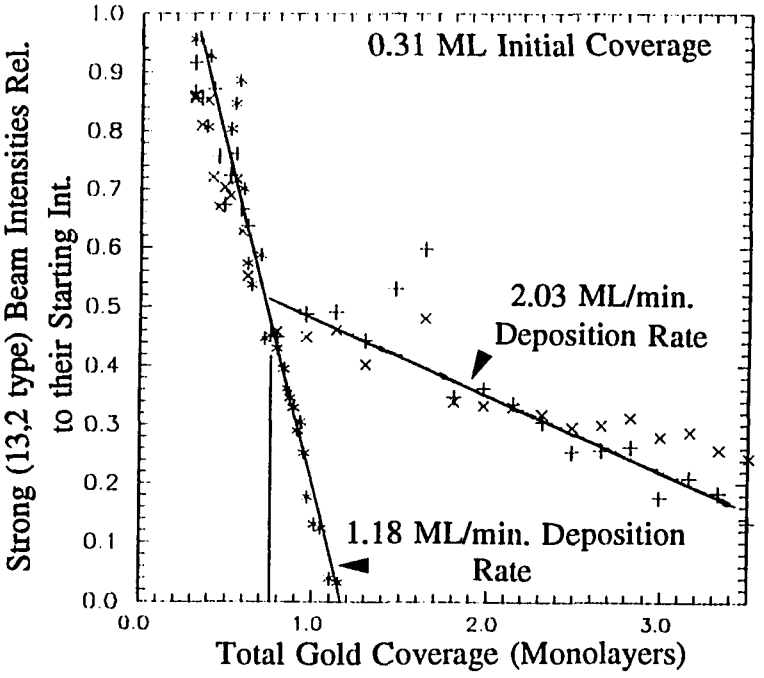


Figure 4.9. Plot of the intensity of the strongest (13,2 type) 5x2 Au diffracted beams (relative to their initial intensity) versus total gold coverage for room temperature gold deposition at two different deposition rates.

In addition to studying the domain boundaries to obtain information about the 5x2 Au structure (which basically looks into the growth dynamics) we can look at the structure's disordering kinetics by depositing more gold onto the structure at room temperature. The setup for this experiment has already been described in Chapter 2, the results are shown in Figure 4.9 which plots the intensity of strongest 5x2 Au beams versus the total gold coverage for two depositions. The key features to note are that for both depositions

the initial beam decay is linear with coverage and that after a certain coverage the decay rate for the faster gold deposition is greatly reduced. The linear decay rate means that some surface diffusion process is the rate limiting step of the structure's disordering process. This ties into the change in decay rate result since with a faster gold deposition rate surface diffusion is inhibited. Unfortunately, unlike the case of gold deposition onto $\sqrt{3}$ Au, discussed in Chapter 6, determining which parts of the structure are disordering based on the decay of the other structure beams is currently impossible since the decay of the other beams in the two runs follows no clear pattern. More deposition runs with different depositions rates could provide useful trends, however.

After completion of the faster gold deposition the strongest 5x2 Au beams still have 20% of their original intensity. Apparently some portion of the 5x2 Au survives at the interface with the gold layer if the gold deposition rate is fast enough. This fact might lead to creating linearly corrugated Au-Si interfaces.

## 4.6 Effect of Oxygen Exposure

A surface with predominantly 5x2 Au and some $\sqrt{3}$ Au surface structure was prepared by depositing roughly 0.60 ML of Au onto the top surface of a sample with clear 7x7 spots on it initially. XPS spectra (Figures 4.10a and 4.10d) show no oxygen was present on either surface before gold deposition, although there was some Mo on the top surface from accidental sample holder milling. After the gold induced structures were prepared on the top surface the sample was exposed twice to $O_2$ , first

to 4.3 Langmuirs ($1.2x10^{-8}$ Torr for 6 min) followed by a 60 Langmuir ($1x10^{-7}$ Torr for 10 min) dose through the deactivated duoplasmatron ion gun. There was no noticeable change in the TED spot intensities of either the 5x2 or the $\sqrt{3}x\sqrt{3}$ spots and hardly any increase in the top surface XPS oxygen peak (Figures 4.10b and c). (This result is in complete agreement with the $\sqrt{3}$ Au oxygen exposure results of Cros et al. (1982)). The rise in the bare silicon, bottom surface, oxygen peak in subsequent XPS spectra (Figures 4.10e and f) indicate that both gold induced structures significantly passivated the top surface against oxygen attack. This result is somewhat surprising since about half the surface of 5x2 Au has a silicon only atomic structure exposed to the ambient while in $\sqrt{3}$ Au essential all of the silicon atoms are partially hidden by gold atoms.

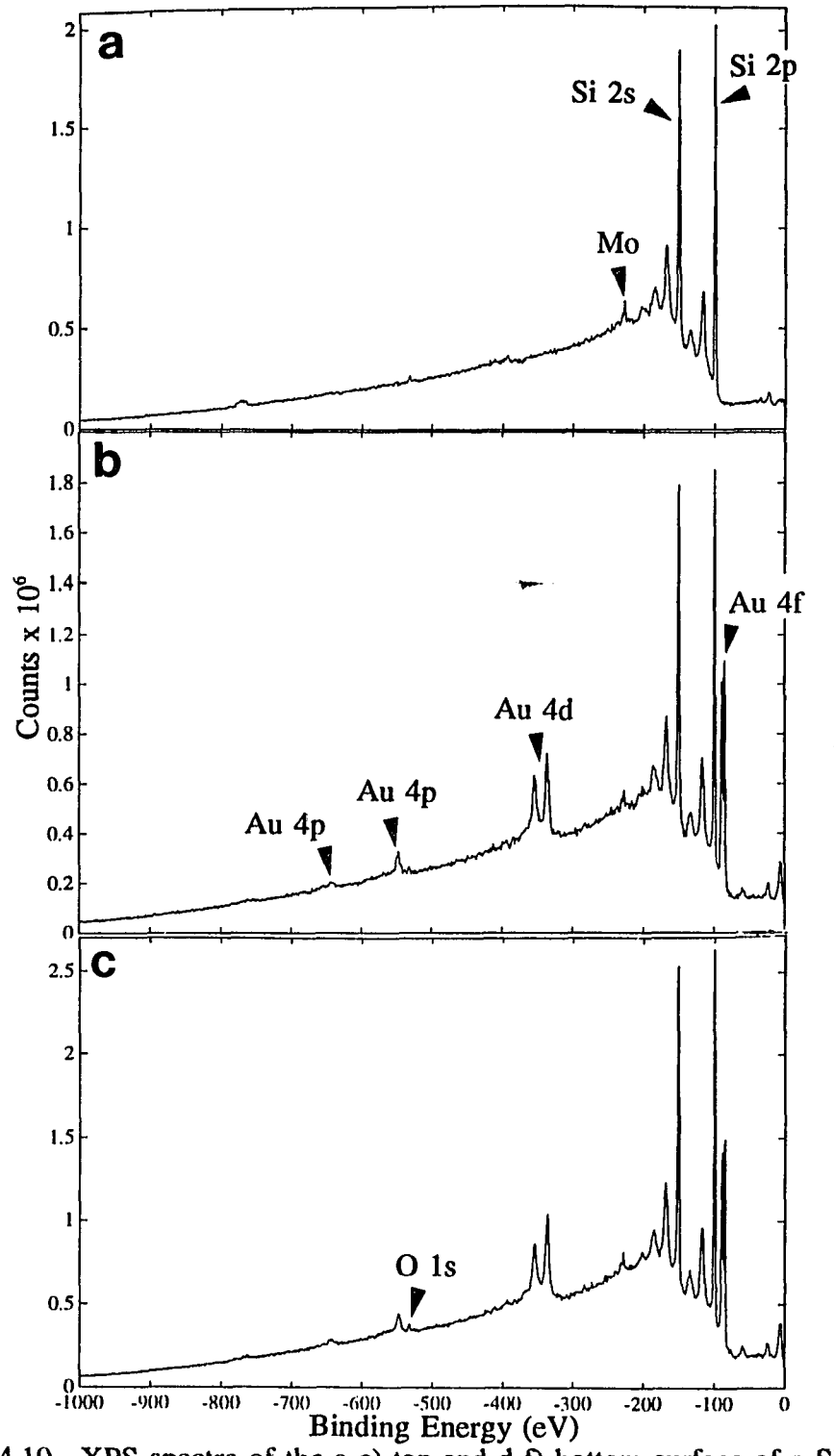


Figure 4.10. XPS spectra of the a-c) top and d-f) bottom surface of a Si(111) sample. a) and d) show the surfaces initially clean and free of oxygen. Onto the top surface 0.6 ML of Au was deposited and annealed forming regions of 5x2 Au and $\sqrt{3}$ Au.

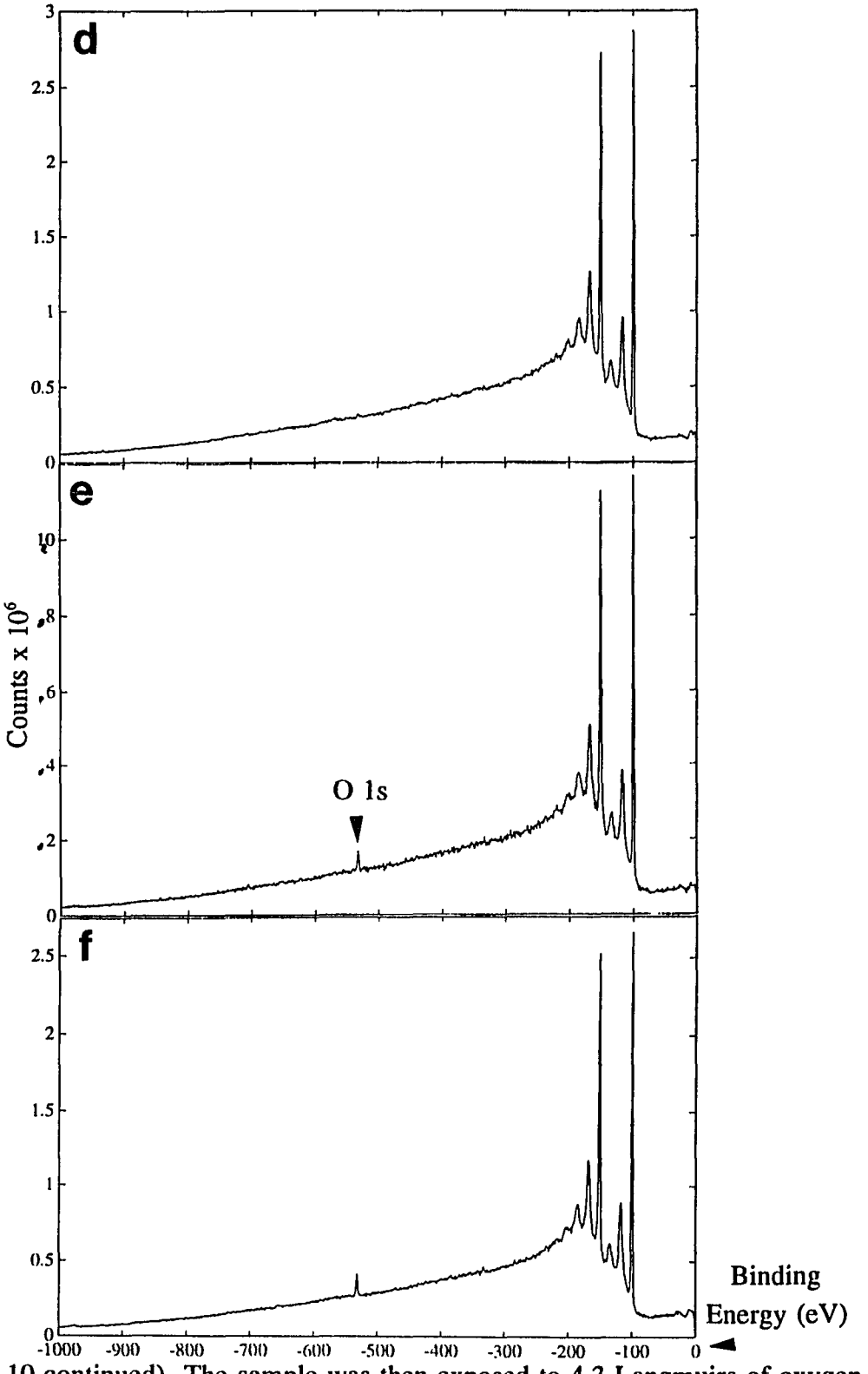


(Figure 4.10 continued) The sample was then exposed to 4.3 Langmuirs of oxygen with b) and e) being the resulting spectra. Finally the sample was exposed to 60 Langmuir more oxygen with c) and f) the result.

# 5 THE Si(111)-($\sqrt{3}$x$\sqrt{3}$)R30° Au SURFACE

## 5.1 Introduction

As one might expect from examining the Au on Si(111) surface phase maps proposed in the literature (Lelay 1983, Ino 1988, Takahashi, Tanishiro, and Takayanagi 1991, Figure 7.1) the extent and central location of the $\sqrt{3}$ Au surface solution belies its central role in understanding the different phenomena seen in this system. We will see in this chapter that understanding the $\sqrt{3}$ Au surface structure is pivotal to understanding the behavior of gold on silicon (111) since this structure embodies the essence of gold to silicon surface bonding, the missing top layer surface structure motif. Also if we can understand what is occurring in this rather complex surface it will be easier to understand the many other $\sqrt{3}$x$\sqrt{3}$ type structures common to adsorbates on the Si(111) surface.

### *5.1.1 $\sqrt{3}$ Au History*

The $\sqrt{3}$ Au structure was first observed by Bishop and Riviere (1969) using low energy electron diffraction (LEED). They reported that it coexists with the 5x2 Au structure at elevated temperatures for coverages between 0.5 to 0.8 monolayers. Although above 0.8 ML the surface is apparently completely covered with $\sqrt{3}$ Au, the $\sqrt{3}$-Au structure accommodates more gold up to about 1.0 monolayer after which the Si(111)-(6x6) Au structure appears at temperatures between roughly 200°C and 330°C

(Higashiyama, Kono, and Sagawa 1986, Takahashi, Tanishiro, and Takayanagi 1991, Nogami, Baski, and Quate 1990, Takami et al. 1994, Yuhara, Inoue, and Morita 1992b, Dornisch et al. 1991). At higher temperatures $\sqrt{3}$ Au is still apparent but arcs appear around the diffraction spots (Ino 1988, Yuhara, Inoue, and Morita 1992b, Takahashi, Tanishiro, and Takayanagi 1991). Several authors have noted that within the 0.5 to 1.0 ML coverage and 200 to 800°C temperature range a variety of shapes of the $\sqrt{3}$-Au diffraction spots are observed. Sharp spots, diffuse spots, arcs partially surrounding sharp spots, and hexagonally symmetric star shaped spots have been reported (Higashiyama, Kono, and Sagawa 1986, Takahashi, Tanishiro, and Takayanagi 1991, Ino 1988). These features are related to the relatively small sizes of the surface domains, which are on average 7 to 8 $\sqrt{3}$-Au unit cells (approx. 50 Å) in diameter (Nogami, Baski, and Quate 1990). The STM work of Takami et al. (1994), in which the relative coverages of two apparently different $\sqrt{3}$ Au phases were measured as a function of total gold coverage, supports the speculation of Ino (1988) and also Takahashi and coworkers (1991) of two different $\sqrt{3}$-Au phases. Karlsson et al. (1990) using angle resolved photoelectron spectroscopy identified a surface state that could be attributed to the $\sqrt{3}$ Au domain walls.

### *5.1.2 Proposed Atomic Structures*

There have been several studies of the $\sqrt{3}$-Au atomic structure: early STM data (Nogami, Baski and Quate 1990, Takami et al. 1994, Salvan et al. 1985, Dumas et al. 1988, Hasegawa et al. 1990, Shibata, Kimura, and Takayanagi 1992) typically show a

single bright feature per unit cell forming a hexagonal pattern. In at least one study this bright spot had triangular features (Dumas et al. 1988). Bishop and Riviere, from their LEED data (1969), initially proposed a 1/3 ML coverage model with one gold atom per unit cell. Lelay and Faurie (1977) proposed a triplet overlayer model based on Auger electron spectroscopy and LEED. Using ICISS Oura et. al. (1985) proposed a modified triplet coplanar model which consists of a 1 ML triplet layer of gold over a 2/3 ML honeycomb of silicon. Also using ICISS Huang and Williams (1988a) proposed a mixed model consisting of a 2/3 ML gold honeycomb structure with some cells having gold in the unit centers.

Based on MEIS data, Chester and Gustafsson (1991) proposed a missing top layer twisted trimer model (MTLTT) in which a layer of gold takes the place of the first layer of silicon atoms in the top double layer of the Si(111) surface. The gold and silicon atoms in these top two layers of the structure both form trimer groups which rotate about the centers of the trimers. In this model two different types of domains must exist based on which direction the trimers rotate. Each domain obeys p3 symmetry but if they are present in equal amounts their sum obeys p3m1 symmetry. Two possible MTLTT models were proposed in the MEIS study based on whether the silicon trimers rotate about their centers in the same direction or in the opposite direction as the gold trimers. Akiyama, Takayanagi, and Tanishiro (1988) also suggested the $\sqrt{3}$-Au structure could be based on twisted trimers given their TEM results of the Si(111)-($\sqrt{3}$x$\sqrt{3}$) Pd surface. Chester and Gustafsson pointed out the likelihood of significant distortions in the silicon layers immediately below the surface.

X-ray diffraction data (Dornisch et al. 1991) partially support the MTLTT models in also showing a missing top layer trimer structure and "splitting" of the second layer silicon sites. This splitting essentially forms silicon trimers given the constraints of symmetry. Dornisch et. al. saw no rotation of the gold trimers and did not propose a registry of the surface structure with the bulk. Their data also point to the likelihood of substantial subsurface distortions.

The main counter to the MTLTT model comes from the theoretical work of Ding and coworkers (1992) (based on total energy calculations) and is called the conjugate honeycomb chained trimer (CHCT) model. Its dominant features are a missing silicon top layer, gold trimers with no rotation, and first layer silicon atoms equidistant from all the nearest gold atoms. The CHCT model is essentially the MTLTT model without any twists and hence preserves the mirror planes of p3m1 symmetry. This model is supported by the dynamical LEED structure analysis of Quinn, Jona, and Marcus (1992) and by the recent X-ray diffraction work of Kuwahara et al. (1994).

The missing top layer feature of both the MTLTT and CHCT models is supported by the low temperature hole-island pair growth mechanism for the $\sqrt{3}$ Au structure proposed by Shibata and coworkers (1992). They have observed that between 200°C and 280°C, gold deposited on the Si(111)-(7x7) structure will form adjacent domains of $\sqrt{3}$-Au surfaces with a z-axis difference between them equal to the Si(111) surface step height. This can be understood in terms of Si atoms diffusing from a "hole" or defective region of the 7x7 surface and combining with gold

diffusing on the surface to form a √3-Au "island" nearby and one surface step up from the original surface. Simultaneously gold also diffuses onto the now silicon deficient surface of the 7x7 "hole" to form another √3-Au surface there.

Finally a recent total energy cluster calculation of the √3-Au system (Dobrodey et al. 1994) assuming gold in the $H_3$ type site predicts a charge transfer of 0.8 units of electron charge from the gold to the silicon.

## 5.2 TEM/TED Results

### *5.2.1 HREM Results*

The presence of gold trimers on the surface was confirmed by the HREM images in Figures 5.1, taken near the (111) zone axis. The image was noise filtered (Marks 1996) and the contrast from the 220 type bulk fringes was attenuated to enhance the information from the √3 and 1x1 type fringes. As indicated by the polygons set over patches of the √3-Au structure in some areas, this image shows (especially in the domain centers) an apparent local threefold symmetry of the √3-Au structure which could only come from a gold trimer structure with a 1 ML saturation coverage. Determining the exact extent of each domain is difficult in on-zone imaging mode because of the need for low pass filtering. In this imaging mode there is also a slim possibility that a six fold symmetric structure and certain (unlikely) imaging conditions could also generate nearly threefold symmetric image features.

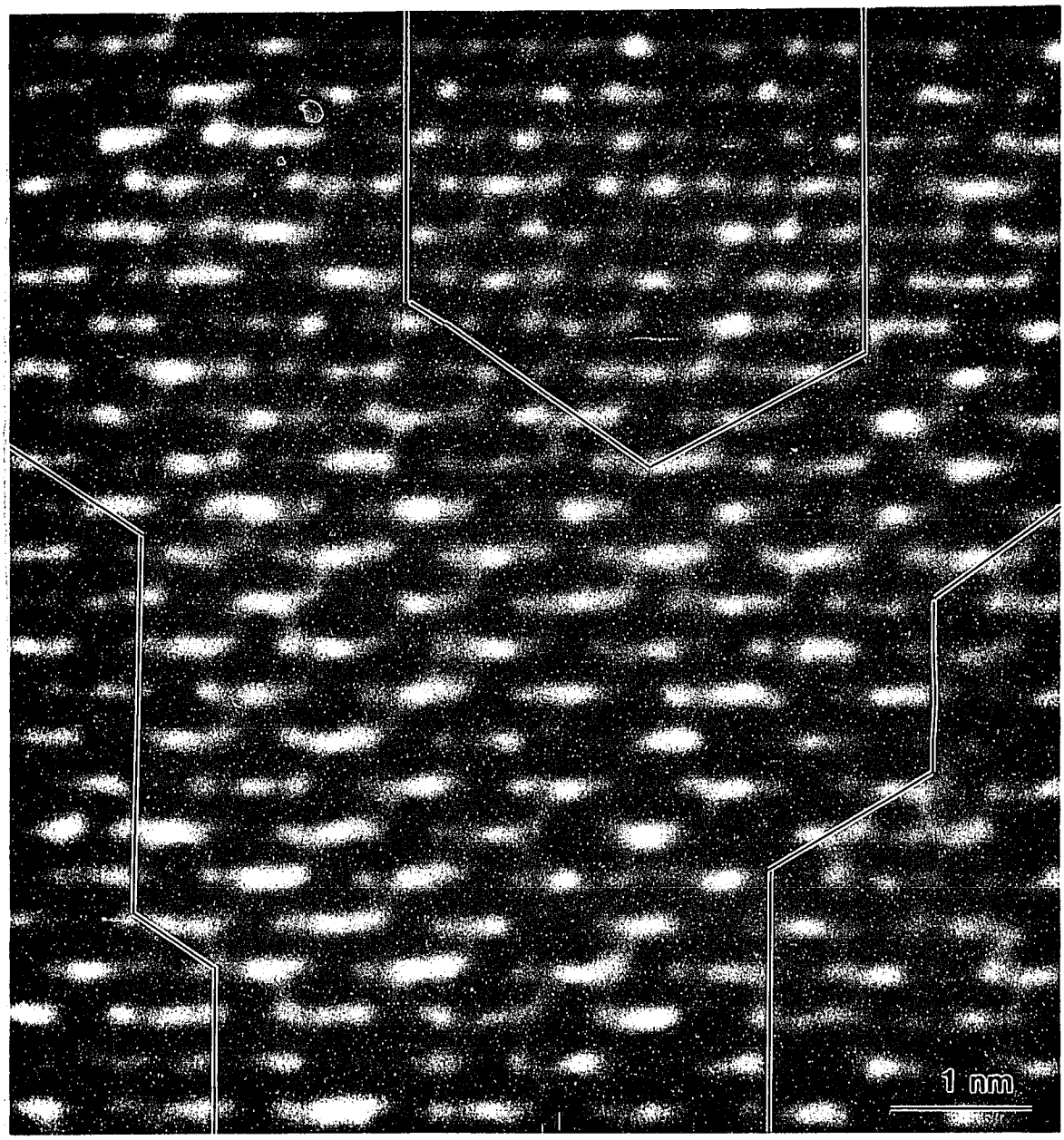


Figure 5.1. (111) zone axis high resolution image of the Si(111)-($\sqrt{3}$x$\sqrt{3}$) Au surface in which the gold trimers appear as dark triangles showing the structure has local threefold symmetry. The lines outlining the Si(111)-($\sqrt{3}$x$\sqrt{3}$) Au domains are more guides for the eye rather than strict delineations of the extents of the domains.

We have found that, for 250kV and 300kV HREM conditions, this structure appears to damage rather rapidly under the electron beam. The nature of the damage appears to be the gold trimers breaking up with some preference for trimers near the domain walls breaking up first. After a trimer breaks up, the gold apparently sits in $T_4$ like sites to make the 1x1 beams exceptionally strong. Figures 5.1 and 5.4 were obtained using minimum exposure techniques to minimize this effect. Because of the much lower beam doses of diffraction mode, the TED data sets should not be effected. This disordering mechanism may explain why LEEM (Sweich, 1991) cannot distinguish between $\sqrt{3}$ Au and 1x1 surfaces at high temperatures, this will be discussed more fully in Chapter 7. The beam damage makes it difficult to determine the extent of the domains in a 300kV TEM using HREM.

### *5.2.2 TED Based Model*

Figures 5.2a and 5.2b show typical off-zone transmission electron diffraction patterns of the $\sqrt{3}$-Au structure used in the atomic structure analysis. To collect as much information as possible, three sets of through exposure series diffraction patterns were recorded with different sample tilts and thickness. The first two of these exposure series have rather diffuse diffraction spots as shown in Figure 5.2a while the third has fairly sharp spots as shown in Figure 5.2b.

Using the diffraction analysis and quantification technique discussed in Chapter 2, three $\sqrt{3}$-Au electron diffraction data sets have the following number of independent beams, sample tilts and sample thicknesses: Set 1 - 264 diffuse beams 118.5 mrad 32.8

nm, Set 2 - 73 diffuse beams 46.0 mrad 33.7 nm, Set 3 - 297 sharp beams 57.4 mrad 30.9 nm. Since fewer beams were sampled in the second data set its results should in general be considered less reliable than the other two. Reciprocal space locations

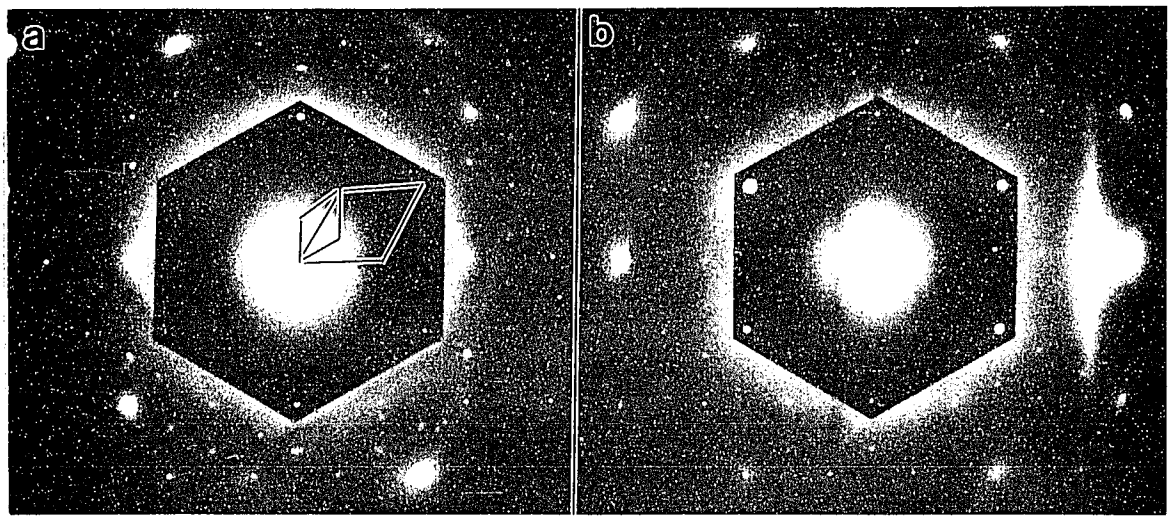


Figure 5.2. Typical experimental off zone diffraction patterns of the Si(111)-($\sqrt{3}$x$\sqrt{3}$) Au surface with a) diffuse and b) sharp diffraction spots. In a) the ($\sqrt{3}$x$\sqrt{3}$) and (1x1) unit cells are indicated by the smaller and larger rhombuses respectively.

beyond the beams appearing in the most heavily exposed negative were checked but had only a shot noise background intensity. Hence surface structure beams from just outside the (2 2 0) set of bulk beams out to the (10 10 0) bulk beams which did not have a measured intensity were set to zero with errors determined from the most heavily exposed negative's variance. This brought the data sets to 530, 332, and 527 beams respectively.

From these data sets the MTLTT model parameters in Table 5.1 were obtained through the $\chi^2$ analysis discussed in Chapter 2. The first column of Table 5.1 gives

Table 5.1.
MTLTT √3 Au model parameters

| | MTLTT Parameters for the Data Sets Included in the Fit | | | | | Corresponding Bulk Si or Au Values |
|---|---|---|---|---|---|---|
| | 1,2,3 | 1,2 | 1 | 2 | 3 | |
| $\chi^2$ Values of Fits | | | | | | |
| Fitting each set alone | | | 2.14 | 2.44 | 2.61 | |
| All sets * | 2.76 | | 2.57 | 2.77 | 3.03 | |
| Sets 1 and 2 * | 2.31 | 2.16 | 2.64 | | | |
| Trimer Values | | | | | | |
| Au-Au 1st layer [in Å] | 2.71 | 2.78 | 2.78 | 2.79 | 2.67 | |
| Trimer Rot. theta [in °] | 1.94 | 0.59 | 0.81 | -0.72 | 3.57 | |
| Si-Si 2nd layer | 2.86 | 3.05 | 3.10 | 3.21 | 2.76 | |
| theta | 3.39 | 7.65 | 8.29 | 2.52 | 2.50 | |
| Si-Si 3rd layer | 3.69 | 3.71 | 3.71 | 3.78 | 3.69 | |
| theta | 0.84 | 0.61 | 0.79 | -0.17 | 0.91 | |
| Si-Si 4th layer | 3.80 | 3.90 | 3.81 | 3.82 | 3.81 | 3.84 |
| theta | 0.23 | -0.02 | 0.14 | 0.09 | 0.20 | 0.00 |
| Values of the gold trimer center to nearest silicon atom vector V | | | | | | |
| Au trimer cen-Si [in Å] | 2.62 | 2.67 | 2.68 | 2.49 | 2.64 | 2.22 |
| theta [in °] | 9.76 | 6.24 | 5.57 | 6.43 | 11.04 | 0.00 |
| Gold to silicon x-y plane projected distances shown in Fig. 2 | | | | | | |
| Au-Si #1 [in Å] | 2.07 | 2.17 | 2.20 | 1.99 | 2.09 | 2.22 |
| Au-Si #2 | 2.50 | 2.48 | 2.46 | 2.38 | 2.49 | 2.22 |
| Au-Si #3 | 2.55 | 2.41 | 2.40 | 2.58 | 2.60 | 2.22 |
| Debye Waller terms | | | | | | |
| Au 1st layer [in Å$^2$] | 3.30 | 2.64 | 2.48 | 4.94 | 3.72 | 1.00 |
| Si 2nd layer | 0.47 | 3.68 | 3.60 | 3.84 | 0.47 | 0.46 |
| Calculated surface coverage of structure | | | | | | |
| coverage Domain 1 [%] | | | 53.1 | | 28.1 | |
| coverage Domain 2 | | | 51.7 | | 26.1 | |
| +/- Error in coverage estimate | | | 28.8 | | 15.7 | |

* When the data sets are fitted simultaneously, the $\chi^2$s reported in the single set columns are the $\chi^2$s of each corresponding set fitted to that combined set structure.

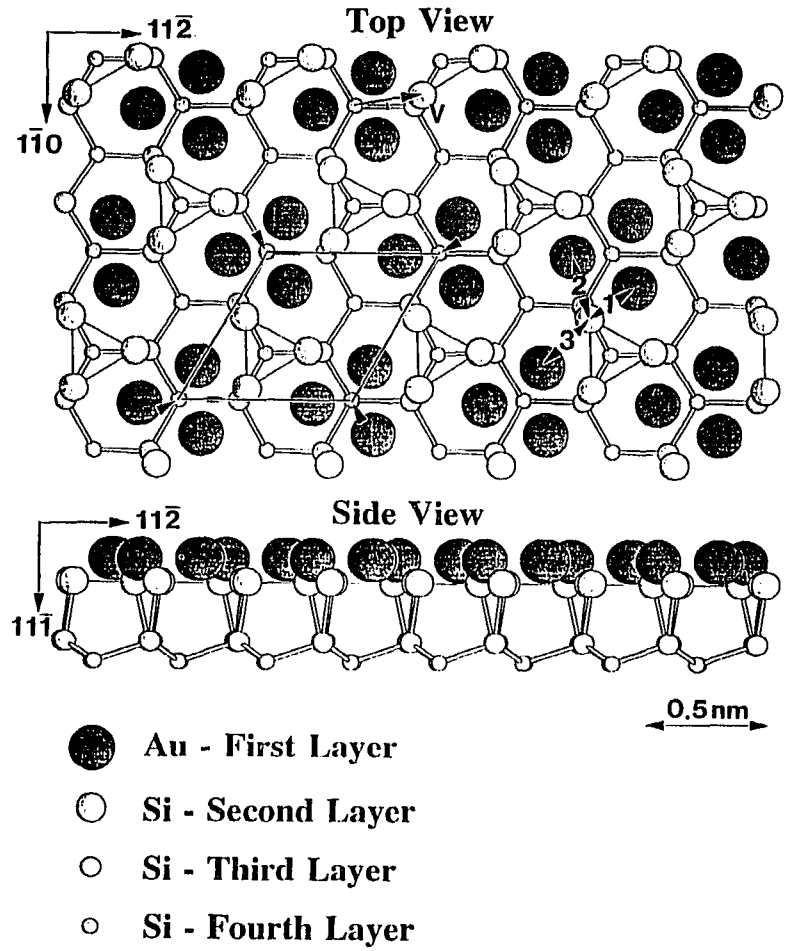


Figure 5.3. Top and side view schematic diagrams of the average Si(111)-($\sqrt{3}$x$\sqrt{3}$) Au atomic structure corresponding to the three data set combined parameters given in the first column of Table 5.1. The primitive unit cell is marked with lines and arrows in the lower left portion of the schematic. Three x-y projected gold to silicon spacings are shown in the lower right. The utility of the vector V (shown above the primitive cell) from the gold trimer center to the second layer silicon atom is discussed in the text. Gold heights are taken from Kuwahara et al. (1994).

the parameters relevant to the MTLTT structure shown in Figure 5.3. This structure has a $\chi^2$ of 2.76 from fitting all three data sets simultaneously.

Also in Table 5.1 there are the $\sqrt{3}$-Au MTLTT parameters from the data sets fitted separately and only the diffuse spot data sets (#1 and #2) fitted simultaneously.

Typically in our diffraction structure analysis, data from at least two different crystal tilt and thickness sets are matched to the proposed structure to eliminate possible artifacts. In such cases combining the sets gives a lower $\chi^2$ than if each set was fitted separately. However, as the $\chi^2$ values in Table 5.1 show, sets fitted individually have better $\chi^2$s and substantially different final parameters indicating that the first/second and the third data sets come from slightly different structures. The major difference between the data sets is that the third data set (sharp spots) has a 3.5° rotation of the gold trimers while the first two sets (diffuse spots) have essentially no gold trimer rotation within experimental errors.

### *5.2.3 Static Disorder in √3 Au*

This variability of the gold trimer rotation angle agrees with the large value of the fitted gold Debye Waller (DW) term given in Table 5.1. In other studies (Jayaram, Xu, Marks 1993, Marks and Plass 1995) our research group has found that the DW term for surface atoms in a well ordered surface structure increases typically by a factor of two times its bulk value. This increase is attributable to the increase in the thermal component of the Debye Waller term since atoms near the surface have added freedom to vibrate. However, the gold DW term in the √3-Au structures typically increased to roughly three times its bulk, value suggesting the possibility of substantial static surface disorder.

In this case the Debye Waller term appears in (Cowley, 1990):

$$S(\mathbf{g})=S_o \sum_h \delta(g-h/a)\exp(-\pi^2(b^2g^2+(\mathbf{g}\cdot\Delta)^2)) \quad (5.1)$$

where S is the average structure factor associated with beam **g**, $S_o$ is the structure factor without local atomic disorder, a is the lattice parameter, $b^2$ is the mean squared amplitude of the thermal vibrations, and $\Delta$ the static mean displacement vector of the atoms. If we assume the static displacements to be isotropic, Equation 5.1 becomes:

$$S(\mathbf{g})=S_o \sum_h \delta(g-h/a)\exp(-\pi^2g^2(b^2+\Delta^2)) \quad (5.2)$$

where the quantity $(b^2+\Delta^2)$ is the Debye Waller term reported in Table 5.1. An anisotropic fit of the Debye Waller terms was attempted to isolate the static portion but the results were inconclusive for reasons mentioned below.

This rather large gold Debye-Waller term is in general agreement with the MEIS results (Chester and Gustafson 1991). The DW term for the second silicon layer remained surprisingly close to its bulk value for the average structure and the sharp spot structure, indicating a well ordered and fairly tightly bonded layer. The DW term rose to several times its bulk value for the diffuse spot structure. Although the DW terms should not be given too much credence (especially the silicon DW term since the $\chi^2$ is not very sensitive to this parameter), their generally high values, interpreted from the point of view of static disorder, do correlate with the trimer rotation, the relatively small size of the surface domains, and the discussion of the domain walls below.

Because of the strong coupling between the Debye Waller (DW) term and the occupancy, the occupancy of atoms for all the layers of the model was held at one

while the DW terms were allowed to increase above their bulk values. This approach is justified by X-ray results (Dornish et al. 1991) and by Figure 5.1 which shows a regular pattern of dark triangular features in the centers of the indicated surface domains. Partial occupancy of gold sites would appear as non-threefold distortions of these central features.

Lack of threefold features at the very edges of the domains and in the domain walls does not relate to the gold occupancy of the $\sqrt{3}$-Au structure itself since the domain walls do not contribute to the diffraction intensity. If gold is missing in these regions then the total gold coverage of the surface would be less than one monolayer while the regions generating diffraction intensity (the central portions of the domains) still have a coverage of exactly one.

### *5.2.4 Domain Walls / Registry*

The diffraction based evidence for two types of $\sqrt{3}$ Au surface domains is also supported by high resolution images. Figures 5.4a and 5.4b are HREM on zone images showing two regions of the $\sqrt{3}$-Au surface with different diffraction spot diffuseness. Both Figures 5.4a and 5.4b have been noise filtered and both have had the bulk (220) beams eliminated. Also the 1x1 type beams have been attenuated to enhance information from the lowest order $\sqrt{3}x\sqrt{3}$ (1 0) type beams. The top halves of the insets are the corresponding power spectra of Figures 5.4a and 5.4b before low pass filtering while the bottom halves are experimental diffraction patterns from similar regions, (to the right of the insets are eight-time enlargements of the indicated

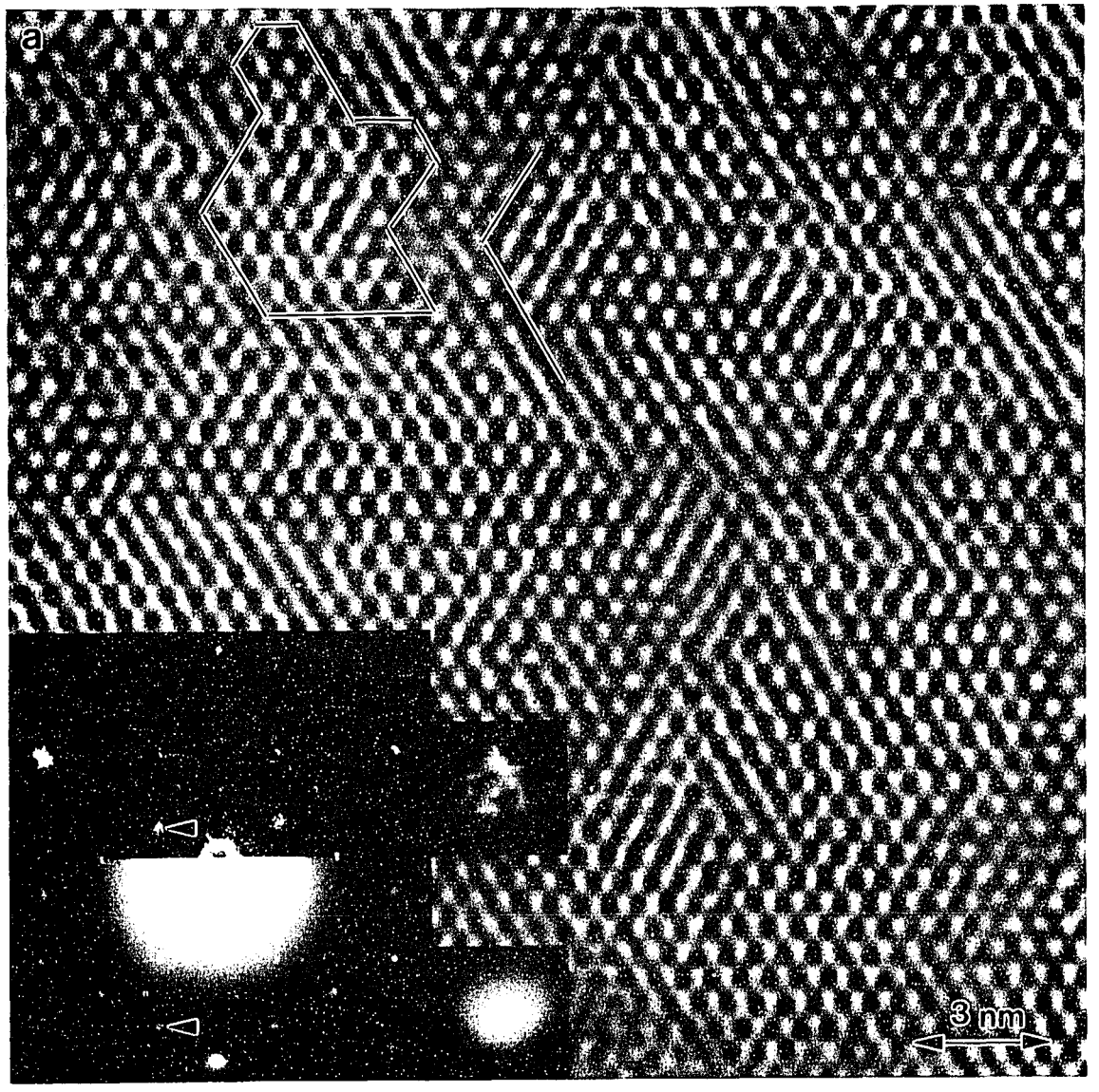


Figure 5.4. Strongly low pass filtered HREM (111) zone axis images showing two regions of the $\sqrt{3}$-Au surface. a) is from a region with diffuse diffraction spots as shown by its corresponding power spectrum (before low pass filtering) in the top half of the inset. b) is from a region with sharp spots as shown by its inset. The bottom halves of the insets are experimental diffraction patterns from data sets 1 and 3 respectively while to the right of each main inset are 8X magnifications of the

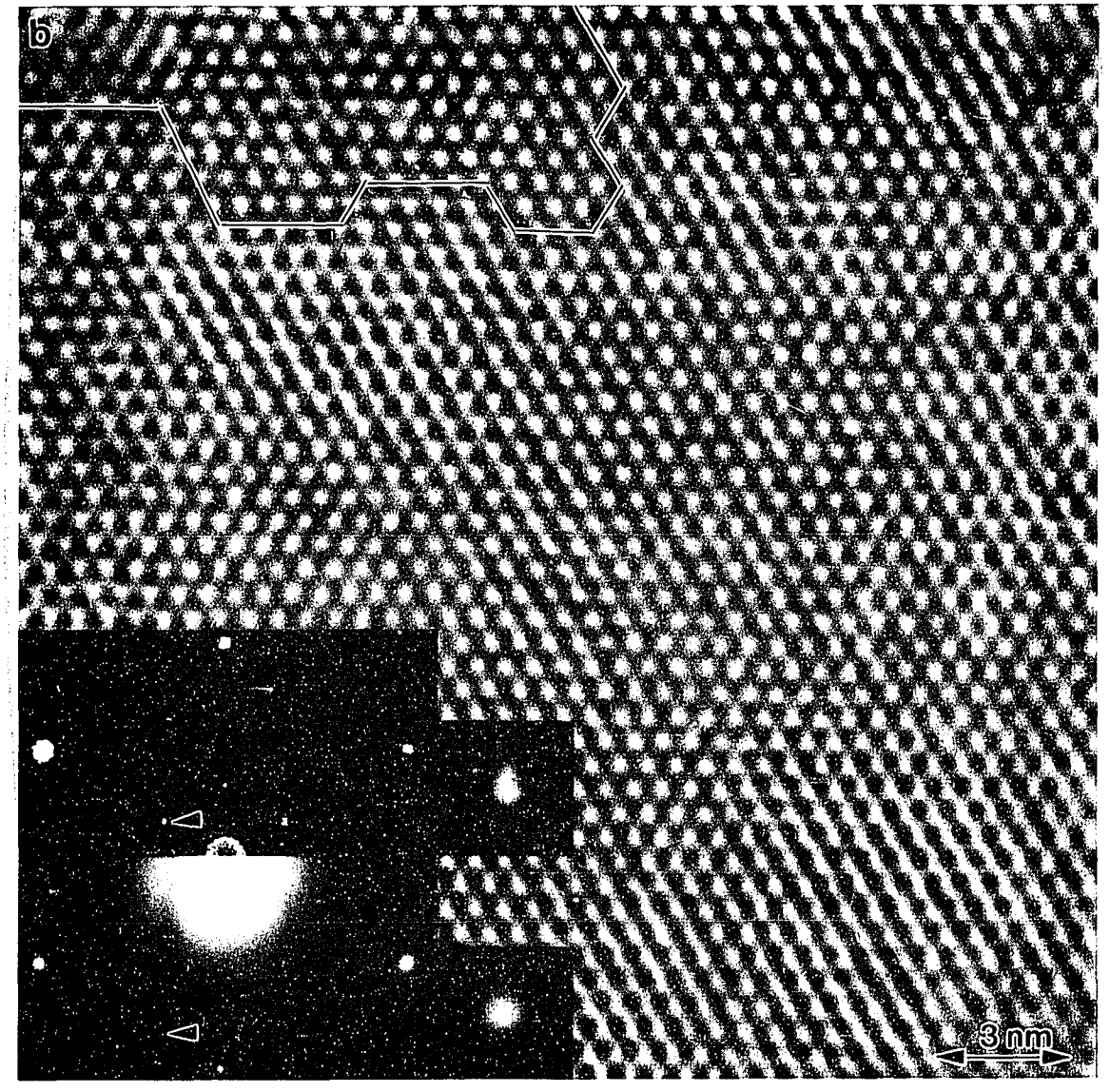


(Figure 5.4 continued) corresponding arrowed spots. An outlined $\sqrt{3}x\sqrt{3}$ domain in the upper left of a) is surrounded by regions of lower fringe contrast indicating a domain wall, the rough boundary of which is indicated by the lines to the right of the surface domain. Note the difference between the wider surface domain walls of a) versus the narrower walls between domains in b) indicated, for instance, by the line between two domains in the upper left of b).

beams). While the √3 spacing (6.65 Å) fringes are present in both, Figures 5.4a and 5.4b have distinctly different morphologies. Figure 5.4b essentially shows that sharper √3-Au diffraction spots correspond to a tighter packing of √3x√3 spacing crossed fringe regions which could indicate a tighter packing of surface domains. This packing difference is illustrated by the sharp transition between the lighter and darker √3-Au feature regions outlined in the upper left region of Figure 5.4b versus the wider region of lower contrast surrounding the √3-Au domain outlined in Figure 5.4a. (It is possible that this feature could also simply indicate that more electron beam damage has occurred at the domain edges.) Since the surface regions shown in Figures 5.4a and 5.4b are only 97 nm apart, different researchers could be studying subtly different structures depending on the exact surface preparation conditions used, a fact that to which Kuwahara and coworkers have already alluded (1994).

### *5.2.5 Comparison with Other Proposed Models*

Given the nature of the √3 Au data discussed above, I will now highlight the key features of the three data sets fitted simultaneously to the MTLTT structure in comparison to literature models. Given the above mentioned facts, the structure obtained from fitting all the diffraction data can only be considered an average structure of the √3 Au surface. Results from the separately fitted data sets give a better indication of the structures of the diffuse and sharp diffraction spot surfaces. Hence, important differences between these results, the average structure results, and literature results will be noted where appropriate.

The average structure in general matches MTLTT Structure 1 proposed by Chester and Gustafsson in which the gold and silicon trimers rotate in the same direction. The first layer of the structure consists of gold atoms near the $T_1$ type sites forming trimers centered at and rotating about the $H_3$ type sites. The gold trimers rotate by an average 1.9° with a Au-Au gold interatomic distance of 2.71 Å. The second layer of the structure consists of silicon trimers rotated by 3.4° about their centers (in the convention used by Chester and Gustafsson) with a Si-Si interatomic distance of 2.85 Å. Since TEM is not sensitive to displacements parallel to the electron beam the z axis distance between the gold and silicon layers could not be measured. Therefore all TED based interatomic distances quoted between the gold and the silicon are x-y plane projected distances. (The literature values for the gold to silicon layer distance include 1.7 Å from MEIS (Chester and Gustafsson 1991), 0.3 Å and 0.7-2.0 Å from ICISS (Oura et al. 1985 and Huang and Williams 1988a respectively), 0.9 Å from XRD (Kuwahara et al. 1994), 0.56 Å from total energy calculations and LEED (Ding, Chan, and Ho 1992, Quinn, Jona, and Marcus 1992). The XRD height result is incorporated the side views of Figures 5.3 and 5.5.)

Before continuing this discussion, an important point concerning the structure parameters needs to be made. In the MTLTT model there are two "twist" centers, care must be taken to choose appropriate parameters when comparing different structure models. The structure description parameters used by Chester and Gustafsson are the interatomic distances within a layer and the rotation angles of the gold and silicon trimers about their individual centers. While the Au-Au interatomic

distance plus the gold trimer rotation angle are good descriptions of the gold layer of the structure, second layer silicon displacements only along the line joining gold trimer centers would generate a silicon "twist" about the local silicon threefold center even though true silicon trimers have not formed as, for example, in the CHCT model (Ding, Chan, and Ho 1992). A better description of the position of the second layer silicon atoms with respect to the gold is the vector from the gold trimer center to the second layer silicon atom (shown by the arrow V in Figure 5.3) measuring the angle in terms of the deflection of silicon from its bulk site. This parameter's advantages are a ready display of the degree of silicon trimerization in terms of the vector angle while also showing the general displacement of the silicon from the gold in terms of the vector magnitude. These vector parameters for all TED structures are given in Table 5.1. We can see that in all cases the silicon atom to gold trimer center distance remains roughly constant but the angle of the actual silicon site from its bulk position, while always at least 5°, increases to 11° when the gold trimers rotate. The fact that both the first layer Au-Au and second layer Si-Si interatomic spacings contract somewhat for the rotated gold trimer data set is also worth noting.

Table 5.2 shows a comparison of the present work's average structure model to recent gold trimer based models which propose lateral sites for both the gold first layer and the silicon second layer. As several authors (Chester and Gustafson 1991, Oura et al. 1985, Dornisch et al. 1991, Ding, Chan and Ho 1992, Quinn, Jona, and Marcus 1992) have concluded, 2/3 ML honeycomb based models can be excluded from consideration. Table 5.2 provides silicon to gold trimer center values mentioned

Table 5.2.
Comparison of Recent Models of the Si(111)-($\sqrt{3}$x$\sqrt{3}$) Au Surface.

| | TED | X-ray | | MEIS | | T.E.C. | LEED |
|---|---|---|---|---|---|---|---|
| | Avg. | III-Si | III-Au | Str 1 | Str 2 | | |
| Trimer Values | | | | | | | |
| Au-Au [in Å] | 2.71 | 2.80 | 2.80 | 3.00 | 2.90 | 2.83 | 2.80 |
| theta [in °] | 1.94 | 0.00 | 0.00 | 12.00 | 12.00 | 0.00 | 0.00 |
| Si-Si 2nd layer | 2.86 | 2.89 | 2.88 | 3.20 | 3.20 | 3.50 | 3.50 |
| theta | 3.39 | 4.84 | 5.64 | 18.00 | -17.00 | 11.40 | 11.66 |
| Values of gold trimer center to nearest silicon atom vector | | | | | | | |
| Au cen-Si [in Å] | 2.62 | 2.65 | 2.67 | 2.94 | 2.08 | 2.68 | 2.69 |
| theta [in °] | 9.76 | 8.86 | 8.74 | 2.19 | 18.48 | 0.00 | 0.00 |
| Gold to silicon x-y projected distances | | | | | | | |
| Au-Si #1 [in Å] | 2.07 | 2.06 | 2.08 | 2.85 | 1.73 | 2.34 | 2.34 |
| Au-Si #2 | 2.50 | 2.56 | 2.57 | 2.27 | 2.09 | 2.34 | 2.35 |
| Au-Si #3 | 2.55 | 2.45 | 2.43 | 2.07 | 3.20 | 2.34 | 2.34 |

TED = Present Study, X-ray = (Dornisch et al. 1991), MEIS = (Chester and Gustafson 1991)
T.E.C = (Ding, Chan and Ho 1992), LEED = (Quinn, Jona, and Marcus 1992)

above for all models as well as the silicon trimer rotation parameters of Chester and Gustafsson for comparison. All gold to silicon spacings are x-y plane projections which are based on the parameters quoted by the respective authors. The gold trimer center to silicon atom spacing shows good agreement between the X-ray, dynamical LEED, total energy calculation, and the present study's average model. The fact that the silicon position deflection angle can vary between 5° and 11° agrees with the grazing incident angle X-ray models. While not included in Table 5.2, the lateral spacing X-ray diffraction results of Kuwahara et al. (1994) essentially agree with our

results since they found a gold-gold interatomic distance of about 2.7 Å and no trimer rotation within ±3.0° for a diffuse LEED diffraction spot structure.

Where our results disagree with the three studies is in the gold trimer rotation. Although we agree with the MEIS results in confirming that the gold trimers rotate, our findings do not agree with theirs in the degree of rotation. The present results are most at odds with the dynamical LEED results (Quinn, Jona, Marcus 1992) where no gold or silicon trimer rotations were reported for "sharp, high quality spots". The LEED analysis and the total energy calculation results concluded that the $\sqrt{3}$-Au structure must obey p3m1 symmetry. However, we conclude the structure has two domains of local p3 symmetry. With small average domain size and a sufficient number of domains of both types in a given area p3 symmetry domains will give results identical to p3m1 symmetry since the diffraction intensities will balance statistically. A clear example of this diffraction intensity summing of two p3 type domains is given by Akiyama and coworkers (1988) in a TEM study of Si(111)-($\sqrt{3}$x$\sqrt{3}$) Pd. In this study dark field images using the strongest surface related diffraction spots showed consistent intensity differences between the two types of domains arising from Pd trimers twisted roughly 6° with respect to the bulk.

To check the robustness of the average structure model, several variations of the starting structure were studied. Changing the number of layers that were allowed to relax produced the following $\chi^2$s versus relaxation depths: 4.54 for no relaxation (just the gold can move), 2.88 for one layer (just the gold and second layer silicon can move), 2.78 for two silicon layers, and 2.76 for three silicon layers with $\chi^2$ remaining

constant for deeper relaxations. These results, which provide a good indication of the x-y plane silicon displacements with depth, are in agreement with the X-ray diffraction results of Kuwahara et. al. (1994). Their study shows small z axis silicon displacements for the third and fourth silicon layers. Table 5.1 gives the average structure trimerization of third and fourth layers of the structure.

We found that if Chester and Gustafsson's Structure 2 (with counter-rotated silicon and gold trimers) is used as a starting point the $\chi^2$ minimization will move back to Structure 1. If the gold and silicon trimers are not allowed to rotate (essentially a CHCT model), the resulting has a $\chi^2$ of 3.50 and the gold DW term rises to four times its bulk value versus three times its bulk value in our proposed structure. Clearly the rotation of at least one set of trimers must be present in the structure. If silicon trimers can rotate but the gold trimers cannot, a structure very similar to the one proposed by Dornisch et al. (1991) has a slightly increased $\chi^2$ of 2.82 (for our data) and a slightly increased gold DW term. If the gold trimers are locked with no rotation for the fitting of third data set alone (the sharp spot set with normally the largest gold rotation) the resulting $\chi^2$ is 3.03 versus 2.61 if the gold trimers rotate.

The rotation of the gold trimers could explain certain STM $\sqrt{3}$-Au coverage results first seen by Nogami, Baski, and Quate (1990) and quantified by Takami et al. (1994), although other explanations are possible. To explain, we first note that the theoretical work of Ding and coworkers (1992) predicts that the gold trimer will have electronic states corresponding to the single bright feature per $\sqrt{3}\times\sqrt{3}$ unit cell seen in STM. This analysis was based on the CHCT model which roughly corresponds to our

diffuse diffraction spot structure (usually seen at lower coverages) in having no gold trimer rotation. However, the recent STM results show that single bright feature per unit cell regions covers the surface only in the lower gold coverage regime (roughly 0.7 to 0.8 ML), at higher gold coverages (0.9 to 1.0 ML) regions with a $\sqrt{3}x\sqrt{3}$ LEED pattern but more complicated STM features cover the surface (Takami et al. 1994). The trimer rotation moves the gold out of higher symmetry sites with respect to the bulk, possibly breaking some degeneracies of electronic states and leading to a more complicated STM image. The rotated gold trimer structure, which the present work associates with the sharp $\sqrt{3}$ Au diffraction spots (commonly seen at higher gold coverages), could be this second type of $\sqrt{3}$ Au surface seen by STM. Another possible explanation is associated with the gold honeycomb adsorption site discussed in Section 6.3.

### *5.2.6 Charge Transfer*

Another clue to the electronic nature of this structure comes from the scattering potentials used in the fit. X-ray scattering potentials for $\underline{Au^+}$ were used. The corresponding $\chi^2$ for neutral gold atoms was significantly higher, 3.92 for the average structure results with essentially no change in the atomic positions. (It should be noted that this charge transfer result is based on scattering of high energy electrons, not the more ambiguous shifting of gold orbital energies.) The result agrees nicely with the results of Dobrodey et al. (1994) who, in a nonempirical cluster calculation study, predict a 0.8 electron charge transfer from the gold to the silicon. Electron

charge transfer away from the gold also agrees in general with the reduced gold to gold interatomic distance in the trimers (2.72 Å versus 2.88 Å for bulk gold). The significant drop in $\chi^2$ between charged and neutral gold also clearly indicates the need to consider charge transfer in diffraction analysis of these types of structures. An analysis of the $\sqrt{3}$-Au structure with proper charge balance could yield an even lower $\chi^2$ but to the best of our knowledge X-ray or electron scattering potentials for $Si^{-}$ are not available.

### *5.2.7 Independent Coverage Checks*

Given the possibility of at least two different $\sqrt{3}$-Au surface structures (one with diffuse diffraction spots and one with sharp ones), the measurement of the actual coverage of the surface with a $\sqrt{3}$x$\sqrt{3}$ periodic structure becomes more critical. Hence in addition to the estimate of the amount of gold evaporated (roughly 0.70 ±0.05 ML from a quartz crystal microbalance which leads to 70% $\sqrt{3}$ Au structure coverage of the surface), two independent estimates of the structure's coverage were obtained in this study. Stereology of regions of $\sqrt{3}$ spacing fringes in bright field TEM images from diffuse diffraction spot regions were used to obtain an average $\sqrt{3}$-Au domain diameter of 6.8 ± 1.9 $\sqrt{3}$-Au unit cell spacings (45.2 Å ± 12.6 Å) with a surface coverage of 45%. The measurement involved over 130 domains with the domain extent being defined by the visibility of $\sqrt{3}$ fringes running in at least two of three possible directions. If the single direction fringe regions are included in the coverage measurement the $\sqrt{3}$x$\sqrt{3}$ coverage of the surface rises to roughly 75%-90%. Again, it

should be noted that beam damage is a serious issue in this imaging mode.

The other coverage estimation method is based on comparing the calculated absolute diffracted beam intensities to the measured absolute beam intensities, these coverage values obtained for the first and third data sets are given in Table 5.1. This approach is similar to the scattering yield approach used in the MEIS and RBS studies (Chester and Gustafsson 1991 and Yuhara, Inoue, and Morita 1992a, 1992b, respectively). Since the absolute structure beam intensities were not measured directly, the absolute intensities were estimated by comparing the simulated bulk beam intensities with the measured bulk beam intensities to obtain a mean intensity scaling factor. (This is why it is important to measure the absolute beam intensities with PEELS after taking a through exposure TED series.) This scaling factor was then applied to the measured surface beam intensities, after which a comparison of the simulated and measured surface structure beams yielded the coverage estimate, i. e., the percentage of the surface contributing to the intensity of the diffracted beams. This measurement, which in principle can provide very accurate structure coverage measurements for well fitted bulk simulations, is for the $\sqrt{3}$ Au data sets prone to a large source of error because the intensities of the transmitted and strongest bulk beams were not measured. As a result, only a visual fit could be used to obtain a rough estimate of the correct crystal tilt and thickness parameters. Using these two unoptimized bulk parameters then leads to a fairly broad distribution of intensity scaling values and hence a large (55%) standard deviation for their mean; this large deviation then propagates to the coverage measurement. It should be emphasized,

however, that since the coverage estimates fall within an order of magnitude of the expected values (the coverage estimates are 105% for the diffuse spot set and 54% for the sharp spot set compared to 70% from the microbalance and 45% from stereology) there are no serious overfittings or other major discrepancies occurring in the diffraction analysis as would be indicated by much higher or much lower values.

Due to the likely presence of numerous surface steps on the TEM sample and the possible effects of electron beam damage, we do not expect these absolute coverage estimates to be as accurate as the results of Chester and Gustafsson (1991) using MEIS scattering yields (0.85 ML) or the detailed STM studies of Nogami et al. (1990) and Takami et al. (1994). Our rough coverage measurements simply show that the majority of the surface was involved in generating the diffraction intensities upon which we base our model.

## 5.3 $\sqrt{3}$ Au Domain Walls

### *5.3.1 Lower Coverages*

The absence of the dark triangular $\sqrt{3}$-Au features near the domain walls in Figure 5.1 deserves some attention. Bearing in mind that these are on zone images there are only two possible interpretations of the absence of the features: 1) the domain walls are vacancy type with respect to gold and therefore there is no gold to generate a feature, or 2) the gold-gold spacings close to and within the domain walls must be very similar to the silicon 1x1 spacing (3.84 Å). We will return to the second

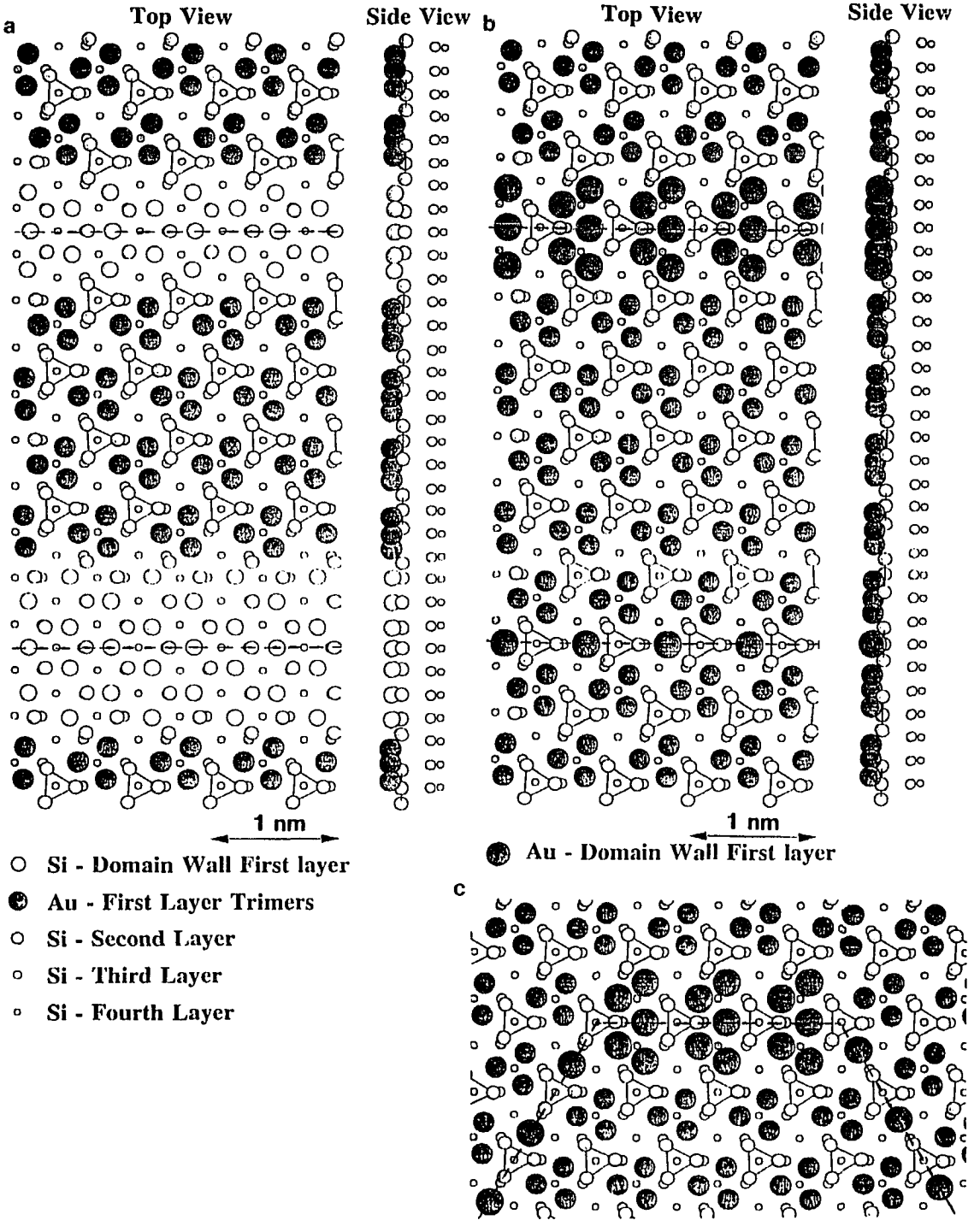


Figure 5.5. a,b) Top and side view schematics of the atomic structures of four possible √3-Au surface domain walls which agree with diffraction and HREM data, the dashed lines show the mirror planes associated with the domain walls. a) shows two vacancy type domain walls consisting of a silicon double layer providing

continuity between √3 Au domains while b) shows "neutral" type domain walls with 1.0 ML total gold coverage. c) Schematic diagram of a turning domain wall incorporating both types of proposed "neutral" domain wall structures. Note the continuity of the trimered silicon layer across the domain walls shown in b) and c) by the lines connecting the trimer Si atoms.

possibility in the next section. Grain boundary theory in general predicts that the domain walls would be of vacancy type, especially for lower gold coverages (0.5 - 0.85 ML). Thus, given that the domains themselves have a gold coverage of 1.0 ML (as we noted earlier, Figure 5.1 rules out partially occupied trimer gold sites) the only way for √3 Au to cover the entire surface at lower coverages is for the domain walls to be vacancy type. Two possible vacancy type domain wall structures are shown in Figure 5.5a and are based on the stretched silicon double layer portion of the 5x2 Au structure discussed in Chapter 4. The domain walls we propose are similar in some ways to two of the three domain walls outlined by Chester and Gustafsson (in their Figure 14 (1991)). These domain wall models are based solely on surface structure to bulk registry considerations and are similar to the domain walls of √3 Ag (McComb, Wolkow, and Hackett 1994, Nakayama, Wantanabe, and Aono 1995). However, we propose that the specific nature of the vacancy type walls is essentially a silicon double layer providing surface continuity between the √3-Au domains. The √3-Au vacancy type domain walls are line defects in the √3-Au surface which can be considered one dimensional analogies to Lave phases. Vacancy type domain walls and the relatively small average domain size lead one to conclude that, at least for lower gold coverages, the √3-Au surface is a two dimensional surface solution which has

different average structure parameters at different gold coverages. The ramifications of this fact will be discussed in Chapter 7.

### *5.3.2 Higher Coverages*

The problem with a vacancy type domain wall picture for the higher range of gold coverages (0.9 - 1.0 ML) is that Nogami and coworkers (1990) saw that the density of domain walls increases with increasing gold coverage. The distinction between the second type of $\sqrt{3}$ Au surface and the domain walls is not clear from the images of Takami et al. (1994). Falta et al. (1995) have recently identified three rows of features within these higher coverage (1.2 ML) domain walls. The three rows of features appear to be centered on $T_4$, $H_3$, and $T_4$ sites as one moves across the domain wall. From this result they derive a model of the domain wall consisting of inverted gold trimers (with respect to the domain trimers) running down the center of the domain wall. The results of Nogami, Baski, and Quate and of Falta et al. point to domain walls which incorporate gold in their structure are present for gold coverages near 1.0 ML. We now focus on what this hypothetical 1.0 ML "neutral" (versus vacancy, heavy, or superheavy) type of domain wall might be based on TEM data.

Because a domain wall will scatter diffusely across reciprocal space the diffraction data cannot provide direct information about the domain walls unless they have a periodic spacing. Hence information must come mainly from images or indirect diffraction data. To understand the HREM based 3.84 Å gold spacing interpretation mentioned earlier, note that in on-zone imaging, multiple scattering

enhances the bulk forbidden/surface allowed, (1x1) type, 3.84 Å spacing beams as well as the bulk beams (Xu and Marks 1992). As a result, in on-zone imaging, even when strong scatterers such as gold have interatomic spacings close to bulk related spacings their scattering will be washed out by the stronger bulk signal. The 5x2 Au structure shows that a 3.84 Å domain wall gold to gold spacing interpretation is certainly possible.

In addition to this fact, what can else we infer about the "neutral" domain wall structure, given the structure of the domains themselves? If the gold trimers alone are considered, a $\sqrt{3}x\sqrt{3}$ type structure on a (111) oriented surface allows three possible registries of the surface structure with the bulk. However, the trimerization of the second layer silicon atoms generates two domains in this layer with a mirror plane between them. A simple, first layer gold trimer registry shift is no longer allowed unless it is accompanied by a second silicon layer domain change. Of the six possible registry shift/domain change combinations (all of which have the same 1 ML local gold coverage as the domain structure, hence the "neutral" description) only the two shown in Figure 5.5b agree with the fitted second silicon layer Debye Waller term for the data sets associated with higher coverages. Recall that the second layer silicon DW term of the average structure and the sharp diffraction spot set structure is very close to the bulk silicon value. This indicates a well ordered layer. Both domain walls configurations in Figure 5.5b have the second silicon layer trimer pattern intact across the entire surface as shown by the triangular pattern of lines connecting the trimered silicons. The other four combinations cause either zipper or W shaped

distortions in the second layer silicon trimer pattern. The domain wall's internal 3.84 Å gold to gold spacing observation and the tight packing of the domains in Figure 5.4b favor the single gold atom type of domain wall, as do the STM images of Falta et al. (1995). Both types of boundaries can only change direction so that the domain walls are 60° apart and one type of wall can change to the other with a 120° angle between walls as shown in Figure 5.5c. These turning rules also apply to the vacancy type domain walls in Figure 5.5a. The behavior of all these domain walls in turning and changing type agrees with the observations of Nogami, Baski, and Quate (1990).

# 6 HIGHER GOLD COVERAGE STRUCTURES

## 6.1 Introduction

Though less extensively studied than 5x2 Au and $\sqrt{3}$ Au the gold induced reconstructions between 1.0 ML and 2.0 ML are important because they represent the transition between surface reconstructions and the bulk like gold 3-D islands and thin films. As will be seen, they often incorporate features of both.

## 6.2 Domain Wall Based Analysis

### *6.2.1 Si(111)-(6x6) Au*

Lander (1964) first identified 6x6 Au from LEED patterns. This structure appears at 1.0 ML gold coverage and higher, most reports suggest 6x6 Au saturates somewhere between 1.4 and 2.2 ML (Takami et al. 1994, Yuhara, Inoue, Morita 1992b, Higashiyama, Kono, and Sagawa 1986). Several sources confirm that 6x6 will form only below a certain temperature (e. g., Yuhara, Inoue, Morita 1992b, Takahashi, Tanishiro, and Takayanagi 1991). Structural data concerning the 6x6 Au surface so far originates from only two sources: STM and X-ray diffraction. Salvan et al. (1985) found a motif of four surface features in poorly resolved STM images which have not yet been reproduced. At lower 6x6 Au coverages (1.1 ML) Nogami, Baski, and Quate (1990) have found 6x6 Au to consist of sets of three STM features surrounded by line

shaped domain walls. A possible interpretation of these features is that they are gold trimers, as in $\sqrt{3}$ Au (Ding, Chan, and Ho 1992). X-ray data (Dornisch et al. 1991) agrees with this interpretation in finding that sets of three gold trimers are part of the 6x6 Au structures. However, the results of Takami et al. (1994) for a 1.4 ML coverage structure complicates matters. Their STM study revealed a rectangular pattern of surface features with a repeat unit cell much smaller than the 6x6 unit cell for all tip biases, despite a clear 6x6 Au LEED pattern.

It would seem that higher coverage 6x6 Au structures are ideal for TEM study since the 6x6 LEED pattern is presumably originating from a structure buried by a simpler surface superstructure. However after repeated attempts the 6x6 Au surface could not be prepared in our system due to the lack of a heating stage in the microscope. After discussions with several groups that have prepared the 6x6 Au surface, a common element in preparing this surface was found: slowly cooling the surface while monitoring it with a diffraction technique. At a certain temperature 6x6 will suddenly form after which the surface is almost always quenched. Without a TEM sample heating stage this procedure was impossible to carry out in our system and several other preparation methods failed to work. Hence, all that was done was to simulate the 6x6 Au diffraction pattern based on the low coverage STM result (Nogami, Baski, and Quate 1990) and our proposed model of the $\sqrt{3}$ Au surface and compare the simulated results to literature diffraction patterns visually. If one assumes that the two types of "neutral" domain walls in Section 5.3.2 have different energies, then 6x6 Au can be understood in terms of the exclusion of one type of

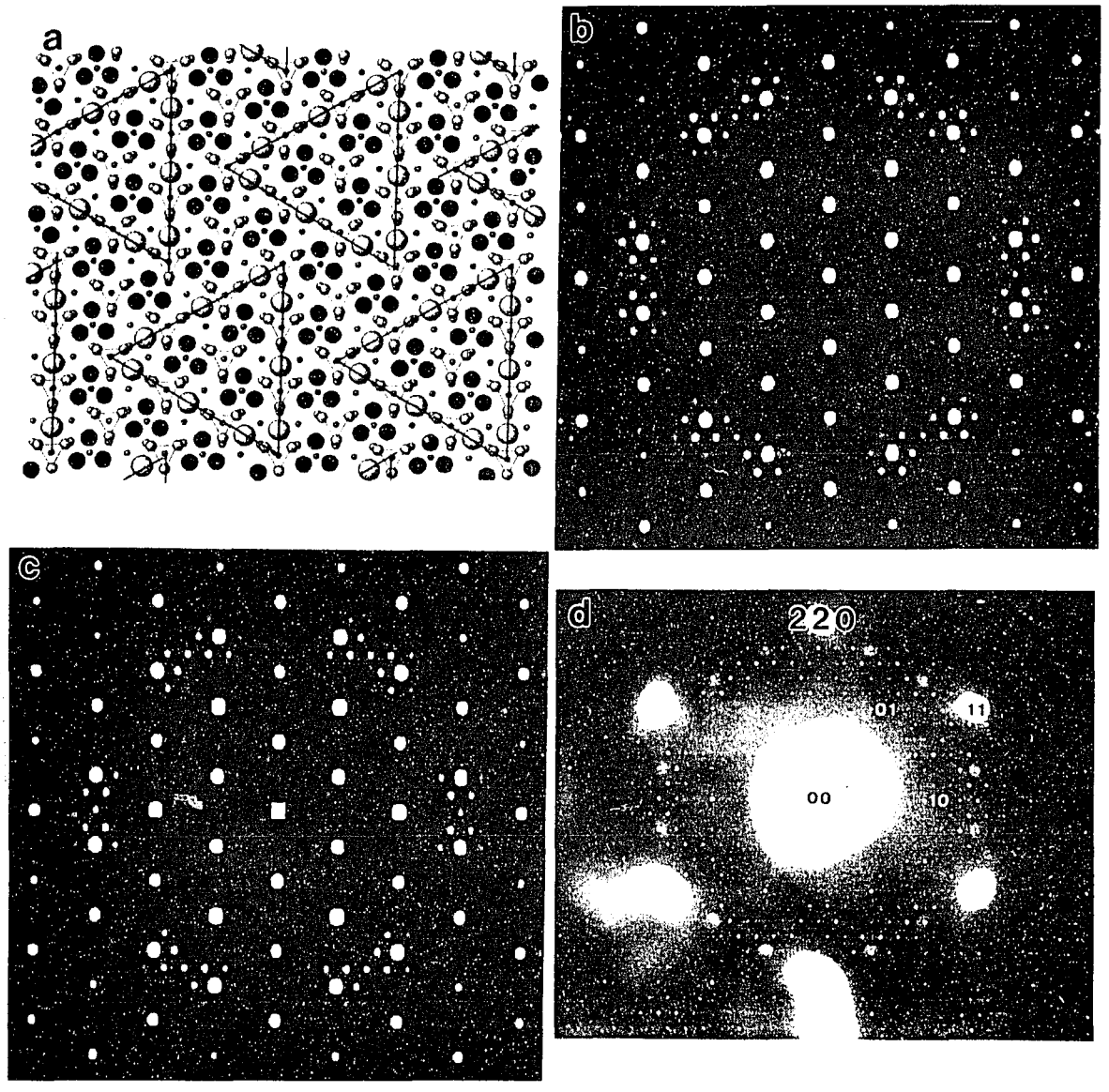


Figure 6.1. a) Top view schematic of our proposed model of the 6x6 Au structure. b) and c) Simulated diffraction patterns including and not including the domain wall gold atoms respectively. d) Experimental diffraction pattern of 6x6 Au (after Takahashi, Tanishiro, and Takayanagi 1991).

domain wall in favor of the other in combination with a shrinking of the domains. In conjunction with the STM and X-ray diffraction three trimer result this leads to our initial model for 1.0 ML 6x6 Au (Figure 6.1a), the resulting match between our simulated diffraction pattern and Takahashi et al.'s TED data (Figure 6.1b and 6.1d respectively) is fair at best.

### *6.2.2 Si(111)-β(√3x√3) Au*

At temperatures higher than roughly 330°C 6x6 Au undergoes an ordered-disordered phase transition (Yuhara, Inoue, Morita 1992b, Takahashi, Tanishiro, and Takayanagi 1991) to what Ino (1988) has dubbed the "β" √3 Au structure. The distinguishing characteristic of the β √3 Au structure is that in diffraction mode this surface has arcs partially surrounding the √3x√3 spots. These arcs are more intense on the transmitted beam side of the spots and have roughly the same radius as the distance from a √3x√3 spot to a 6x6 spot. Their intensity is proportional to the diffraction spots that they partially surround. Takahashi and coworkers have clearly documented the diffraction pattern changes between these two structures with varying temperature (1991) and Yuhara and coworkers (1992b) have noted, using RBS, that gold is lost to bulk diffusion with every ordered to disordered cycle until the surface gold coverage is too low to form 6x6 Au. This limited number of transition cycles effect has also been noted by Sweich and coworkers using LEEM (1991).

The first attempt to understand the nature of the β √3 Au structure was a simulation performed by Higashimiya, Kono, and Sagawa (1986) in which a structure

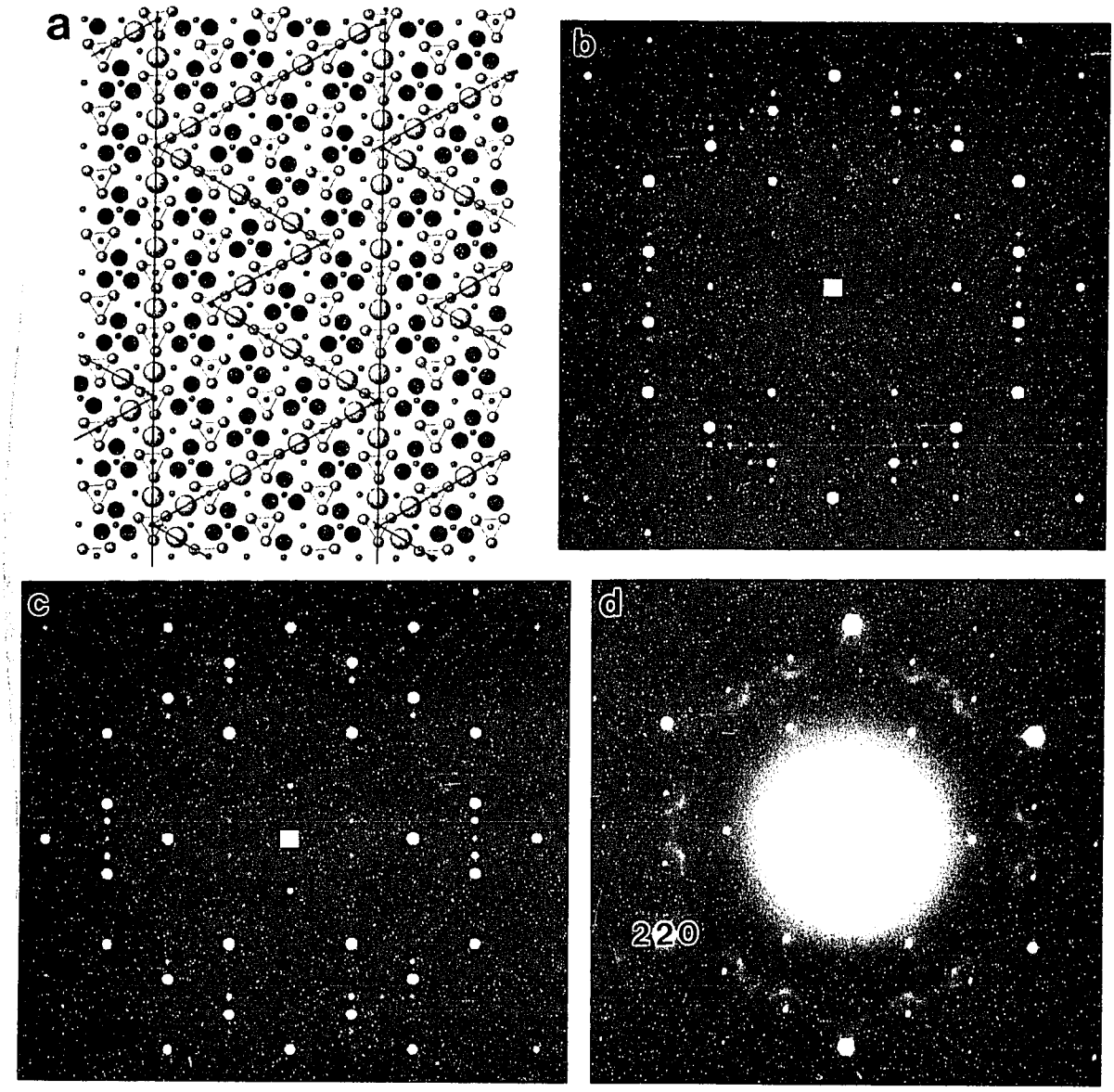


Figure 6.2. a) Top view schematic of our proposed model of the β √3 Au structure. b) and c) Simulated diffraction patterns including and not including the domain wall gold atoms respectively. d) Experimental diffraction pattern of β √3 Au.

40x40 6x6 unit cells across and down was prepared in which proposed 6x6 substructure motifs were given random single $\sqrt{3}$x$\sqrt{3}$ registry shifts. The result was a $\sqrt{3}$x$\sqrt{3}$ diffraction pattern with diffuse rings around each diffraction spot that matched several but not all features of the experimental results. This result clearly showed the relation between the $\beta$ $\sqrt{3}$ Au and 6x6 Au structures: the first is a more disordered version of the second.

The two key problems with Higasimiya's model are that it predicts complete diffraction rings instead of arcs, and that it is too general; essentially any 6x6 motif will generate the same result. Takahashi and coworkers (1991) have speculated, based on diffraction patterns of a quenched version of this surface, that there is a double spot pattern forming the arcs which points to an underlying ordered structure. From the angle and spacing of the primitive spot of this structure (from our own diffraction patterns) we propose $\beta$ $\sqrt{3}$ Au is an inherently disordered structure based on sets of three and six gold trimers as shown in Figure 6.2a. This particular model has a 6x4 unit cell but one would not expect a unit cell to repeat before a random change in the three trimer / six trimer sequence occurs. One can then create several different patterns based on different sequences of three and six gold trimer sets in two directions, which is where the inherent disorder of this structure comes from. This particular 6x4 Au model's diffraction pattern is shown in Figure 6.2b. If the other two rotational configurations are included the arcs are reproduced fairly well. Still it should be emphasized again that this is one model among several possible ones that could generate a similar diffraction pattern. Currently data quantification of $\beta$ $\sqrt{3}$ Au

diffraction patterns and a subsequent direct phasing analysis is being done to properly study this system rather than to simply speculate about possible structures. The need for this work will be apparent in Section 6.3 when we introduce another family of possible structures for 6x6 Au and β √3 Au.

### *6.2.3 Domain Wall Nature*

While the proposed models of 6x6 Au and β √3 Au explain many experimental features, a rather obvious feature of the 6x6 Au and β √3 Au simulated patterns points out a problem with both models. This problem is also related to Higashimiya's simulation. Randomly moving a 6x6 motif by √3x√3 registry shifts leads to an even distribution of spacings between the 6x6 motifs that are smaller and larger than the real space 6x6 spacing. This leads to an even intensity of 6x6 or β √3 Au diffraction features around the √3x√3 diffraction spots. But the experimental diffraction data of both 6x6 Au and β √3 Au shows significantly stronger intensities for the superstructure diffraction features closer to the transmitted beam. This means the domains tend to shift away from each other more often than they shift closer to each other. This feature is apparent in Figures 6.1a and Figure 6.2a but obscured by the additional Au to Au spacings introduced by the gold filled domain walls. If the gold is removed from the domain walls the match between simulated intensities and experimental ones is much better, as shown in Figures 6.1c and 6.2c. However this reduces the coverage of both structures to 0.75 ML. While Yuhara and coworkers (1992b) have found significant gold loss through diffusion into the bulk, RBS studies

of these surfaces, as well as every other study of these surfaces, show their coverage to be higher than 0.90 ML. A possible reason for this perplexing situation is discussed in Section 6.3.

### *6.2.4 Amorphous Au-Si and 3-D Islands*

If gold is deposited at room temperature onto clean 7x7, quenched 1x1 (Meinel and Katzer 1992), or onto the 5x2 Au or $\sqrt{3}$ Au surfaces (Plass and Marks 1996, Ichimiya et al. 1995, Fuchigami and Ichimiya 1996) an amorphous gold silicon layer forms. This layer does not completely disrupt the 7x7 or (under fast deposition conditions) 5x2 Au surfaces but the quenched 1x1 Au and $\sqrt{3}$ Au surfaces are completely disrupted by it. (Apparently 7x7 and 5x2 become part of the buried interface.) In diffraction mode this layer is characterized by a ring about the transmitted beam with a full width half maximum corresponding to roughly 11 Å and an average radius corresponding to 2.59 Å Au-Au spacing (Figure 6.3). A truly amorphous structure generates a the diffuse background in diffraction space and the gold silicon "amorphous" structure does not seem to display an obvious increase in the background intensity. But while the diffuse ring pattern also suggests some local ordering of the gold silicon layer, dark field images (Figure 6.3) and limited HREM experiments show no clear evidence of local ordering.

More gold deposition onto this amorphous surface eventually forms 3-D islands but at disputed critical coverages (Sweich, Bauer, and Mundschau 1991, Ichimiya et. al. 1995, Yuhara, Inoue, and Morita 1992b). RHEED evidence suggests these islands

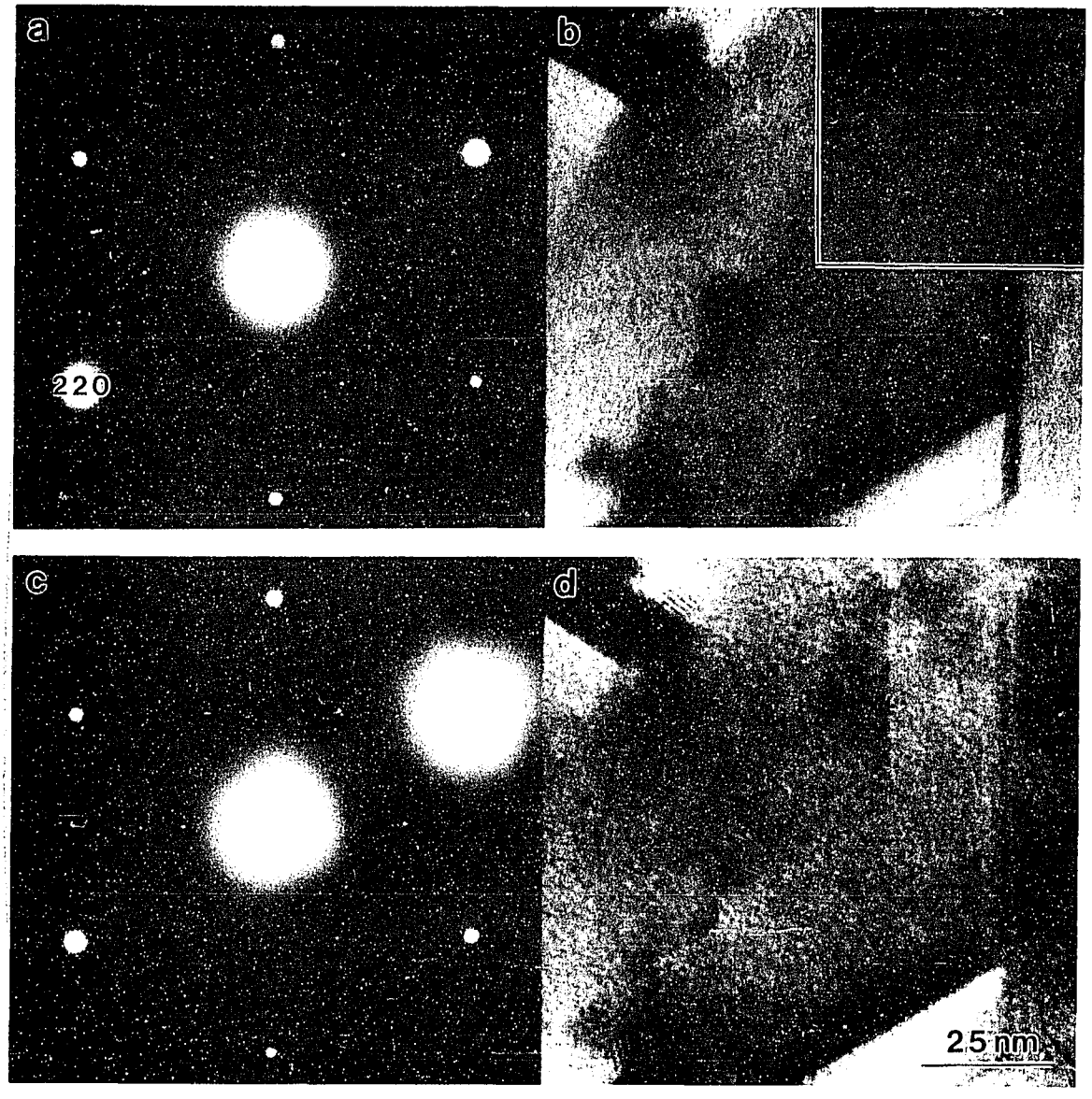


Figure 6.3. Diffraction patterns and corresponding dark field images of a) and b) a pristine 0.75 ML √3 Au structure and c) and d) the same surface with an additional monolayer of gold deposited on it at room temperature. The √3 Au fringe pattern in b) is no longer visible after gold deposition. e) and f) are, respectively, a diffraction pattern and dark field image of a 5x2 Au surface with five monolayers of gold deposited on it. Arrowed Moire fringe regions indicate the presence of islands.

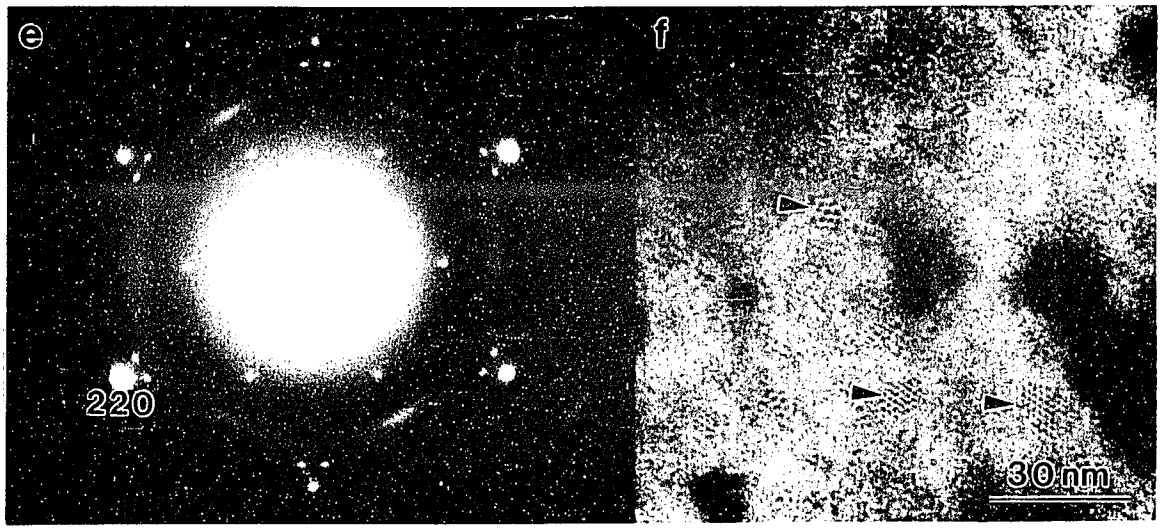


(Figure 6.3 continued)

are composed of the $Au_3Si$ metastable phase (Ichimiya et al. 1995). Annealing studies of this surface (Fuchigami and Ichimiya, 1996) using STM and SEM revealed these islands have a split size distribution with many nanometer sized particles and fewer larger particles. These observations suggest that in a certain temperature range the Ostwald ripening mechanism might occur through the creation, movement, and absorption of nanometer sized particles. We have found some of the larger annealed particles are multiply twinned (e.g., Doraiswamy and Marks 1995).

## 6.3 Honeycomb Gold Adsorption Site.

### *6.3.1 Room Temperature Gold Deposition onto √3 Au*

An immediate question that the room temperature amorphous layer's formation poses is: what is the mechanism by which it can form from

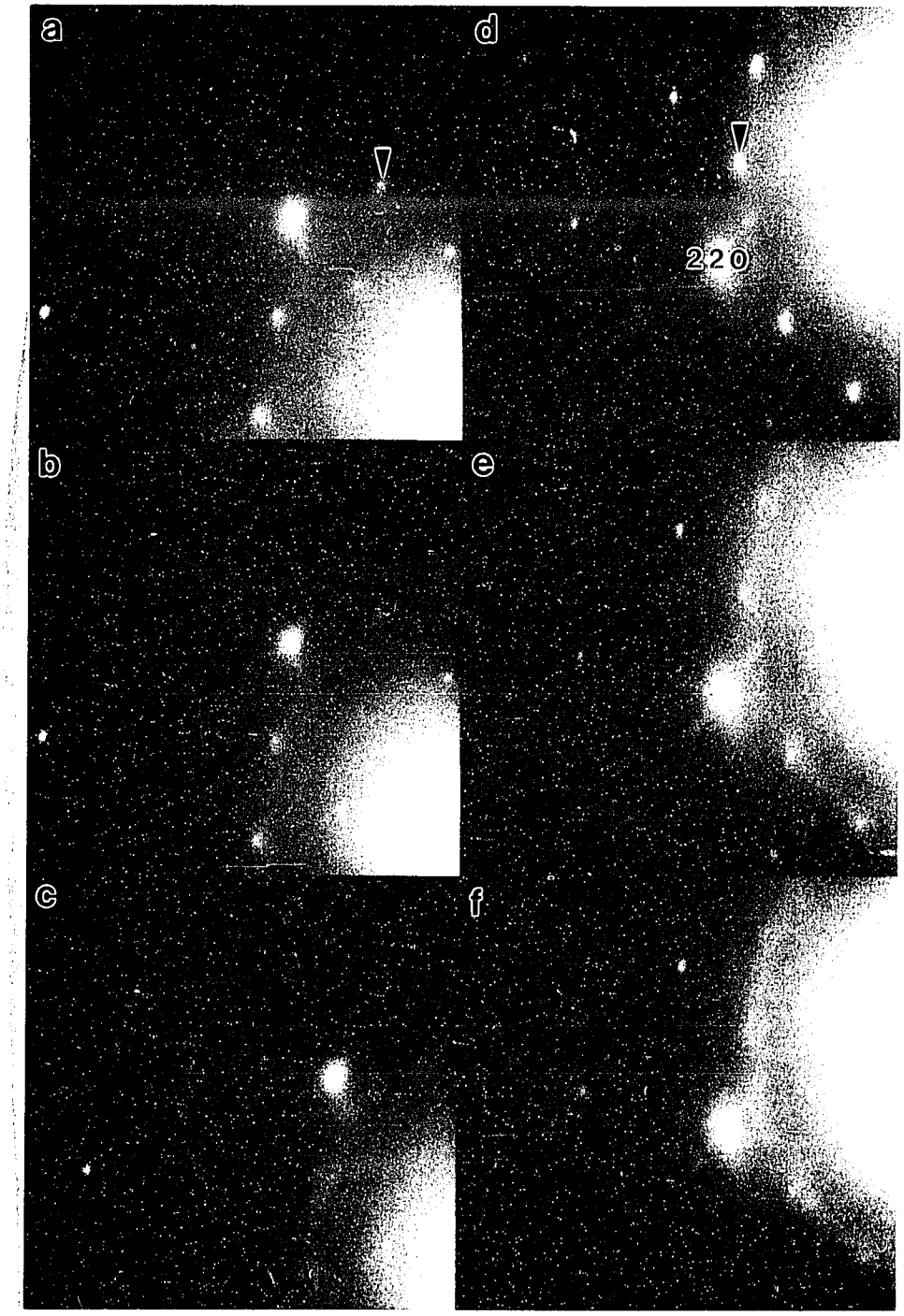


Figure 6.4. Diffraction patterns averaged over three seconds of video tape during gold deposition onto a-c) the diffuse diffraction spot Si(111)-($\sqrt{3}$x$\sqrt{3}$)R30° Au structure, and d-f) the sharp diffraction spot structure with average total Au coverages of a) 0.81 ML, b) 1.05 ML, c) 1.56 ML, d) 0.84 ML, e) 1.19 ML, and f) 1.58 ML. The arrowed diffraction spots are indexed as (2,1).

these four significantly different initial surfaces at such a relatively low temperature? This issue is closely related to the rapid interdiffusion of gold and silicon since it involves room temperature bond breaking (e.g. Hiraki 1986).

As with the 5x2 Au surface in Section 4.5 we investigated this problem by depositing gold at room temperature onto two different initial coverage $\sqrt{3}$ Au surfaces and investigated the changes in the $\sqrt{3}$ diffraction spot intensities as a function of increasing gold coverage. The experimental setup for this study is described in Section 2.6. Some of the key data is shown in Figure 6.4: diffraction patterns taken

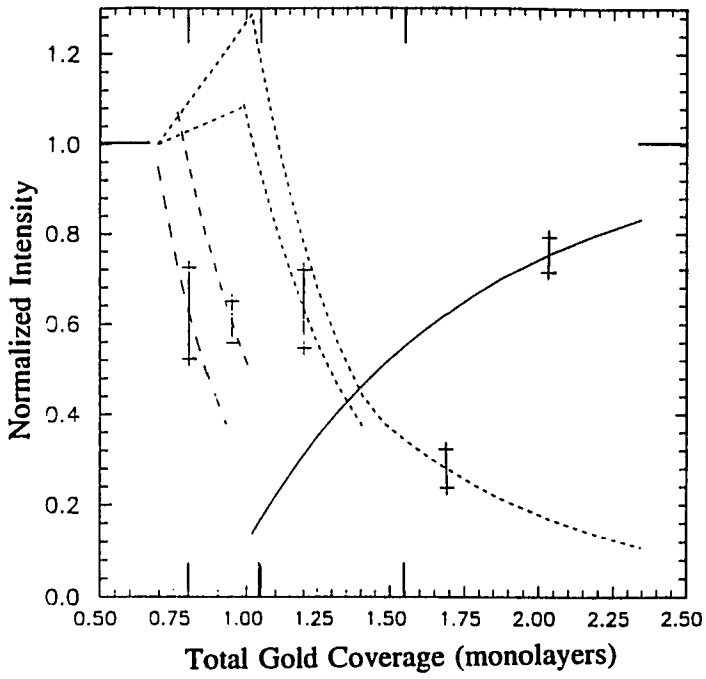


Figure 6.5. Normalized intensity curves (relative to the starting intensities) of various diffuse $\sqrt{3}$ Au diffraction pattern features as a function of total gold coverage; long dashes - average of the (4,1), (5,2) and (6,1) type beams (from 6 data points), medium dashes - average of the (2,0) and (5,0) type beams (14 pts.), upper short dashes - average of the (2,1) and (1,2) type beams, (31 pts.), lower short dashes - (4,0) type beam (22 pts.), solid curve - intensity (arbitrary units) of the ring forming around the transmitted beam (19 pts). The error bars indicate the scatter in each curve's data. The markers on the x-axis correspond to coverages in Figures 6.4 a-c) and 6.6 a-c).

from the video tape sequences at the beginning of gold deposition, just above one monolayer total coverage, and at about 1.5 ML total coverage. The intensities of the strongest beams of the $\sqrt{3}$ Au surface (Figure 6.5) initially increase with gold coverage up to one monolayer total coverage, followed by an exponential decrease. The initial decay rate after one monolayer shows a rough correlation to the gold deposition rate: for the lower coverage diffuse spot structure the deposition rate was 1.88 ML/min and the decay rate was -2.81 per ML, for the higher coverage sharp spot structure the deposition rate was 1.83 ML/min with a -2.69 per ML decay rate. While these differences are near the error levels of the measurements, these trends and the first order decay of the intensities show that this system obeys first order, Langmuir kinetics (Zangwill 1988). That is, the decay rate is proportional to the gold deposition rate and inversely proportional to the instantaneous gold coverage. First order kinetics imply a hit and stick decay mechanism with gold surface diffusion playing a minor role in the decay of the surface structure.

### *6.3.2 Direct Phasing of the Higher Order Beam Decay*

From Figure 6.5 we can see that the higher order surface structure beams decayed faster than the strongest structure beams. A Patterson function difference analysis revealed no significant changes in the structure aside from a gradual broadening of the gold trimer sites and loss of long range order. However, a better analysis of the higher order beam decay using direct phasing techniques reveals the

presence of a new gold site.

Using the measured beam intensity changes with coverage and the symmetry averaged structure factor amplitudes of the full diffraction data sets (the ones used to determine diffuse and sharp $\sqrt{3}$ Au structures in Chapter 5) the structure factor amplitudes were calculated at various coverages. Structure factor phases for higher

Table 6.1.
Honeycomb gold site coordinates and relative intensities.

| Diffuse Data | | | | Sharp data | | | |
|---|---|---|---|---|---|---|---|
| θ (ML) | d HC-$Au_1$ (Å) | d T-Au (Å) | R. Int. | θ (ML) | d HC-$Au_1$ (Å) | d T-Au (Å) | R. Int. |
| Present Study's Au honeycomb sites | | | | | | | |
| 0.695 | 1.41 | 2.96 | 0.16 | 0.839 | 2.30 | 2.90 | 0.32 |
| 0.809 | 1.57 | 2.89 | 0.14 | 0.842 | 2.32 | 2.91 | 0.30 |
| 0.924 | 2.21 | 2.41 | 0.55 | 0.873 | 2.15 | 2.82 | 0.42 |
| 0.974 | 2.19 | 2.68 | 0.60 | 0.975 | 2.15 | 2.80 | 0.40 |
| 1.049 | 2.11 | 2.72 | 0.56 | | | | |
| 1.158 | 2.02 | 2.80 | 0.53 | 1.193 | 2.19 | 2.74 | 0.52 |
| 1.325 | 2.07 | 2.77 | 0.51 | | | | |
| 1.556 | 2.35 | 2.66 | 0.57 | 1.575 | 2.24 | 2.74 | 0.53 |
| Original $\sqrt{3}$ Au structure's Si site (Plass and Marks 1995) | | | | | | | |
| 0.700 | 2.17 | 2.78 | 0.20 | 0.850 | 2.09 | 2.67 | 0.20 |

θ = total average gold coverage over 90 frames, d HC-$Au_1$ = distance from the honeycomb Au site to the apex gold trimer atom (see Figure 6.6), d T-Au = trimer gold to gold spacing, R. Int. = honeycomb site intensity relative to the gold trimer intensity.

order beams were then calculated iteratively using the Sayre-Hughes equation (as was discussed in Chapter 2) with starting phases of 122° and 116° for the 1,2 and 2,1

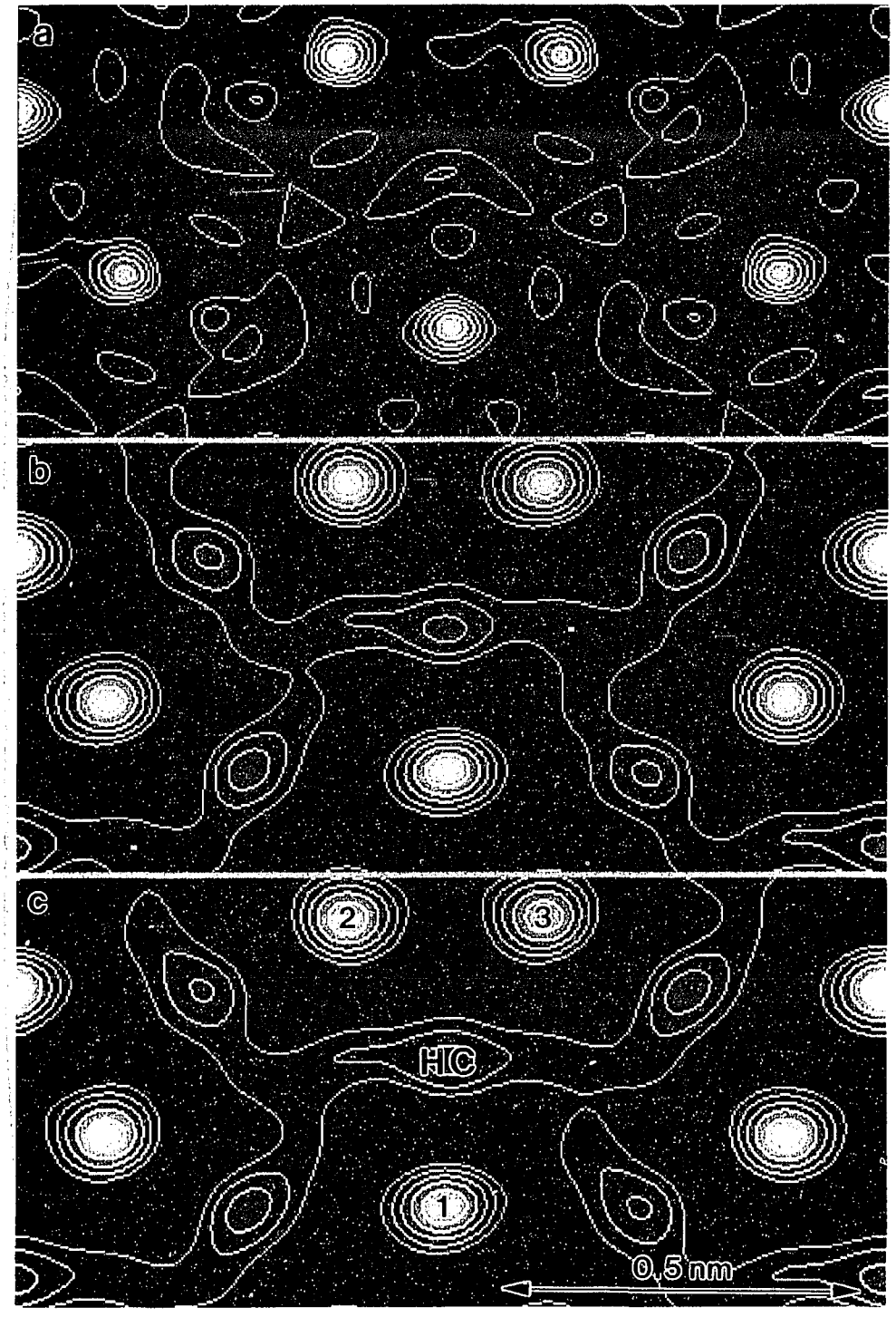


Figure 6.6. Scattering potential maps with overlaid contours corresponding to the diffraction patterns in Figure 6.4.

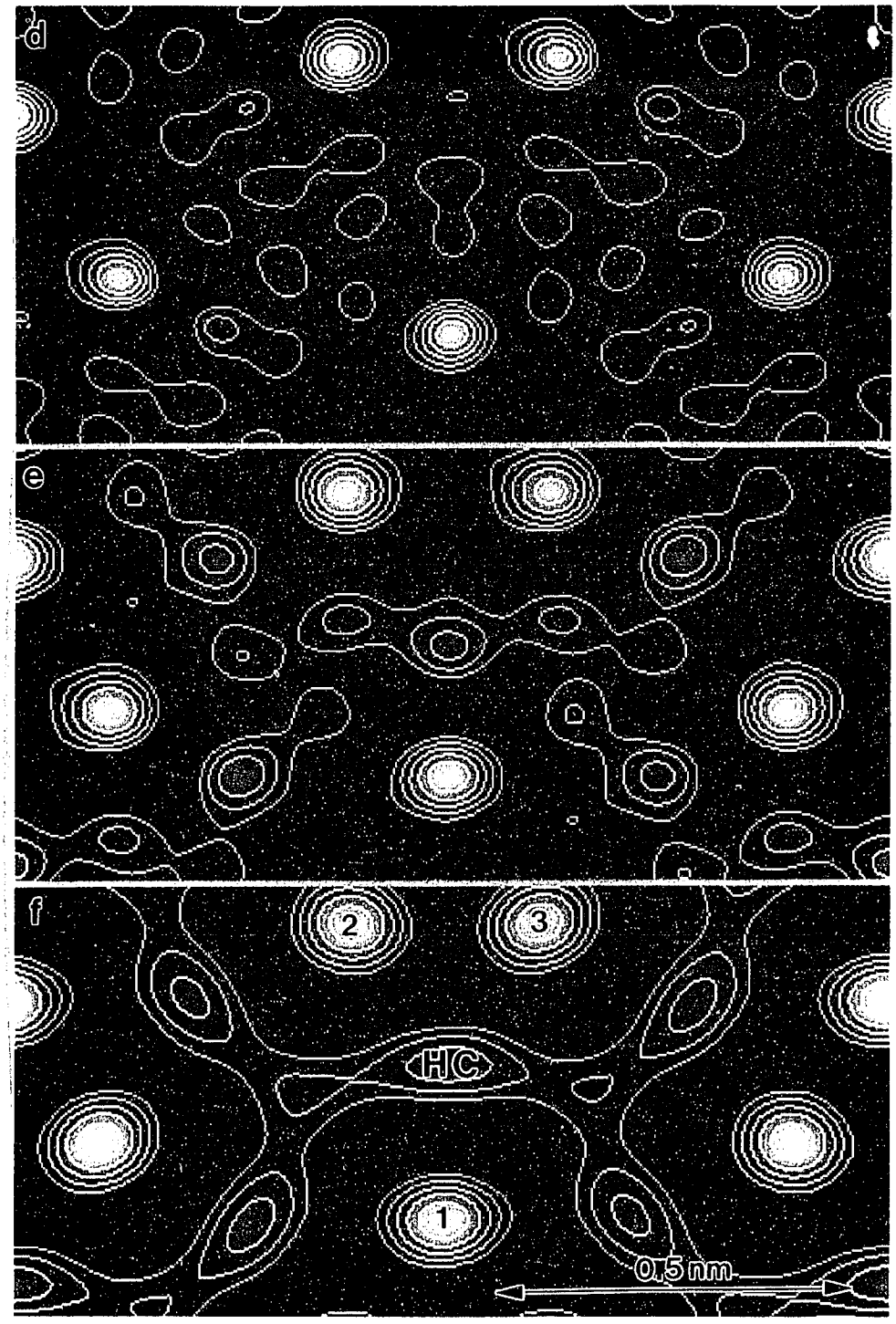
d
e
f
2
3
HC
1
0,5 nm

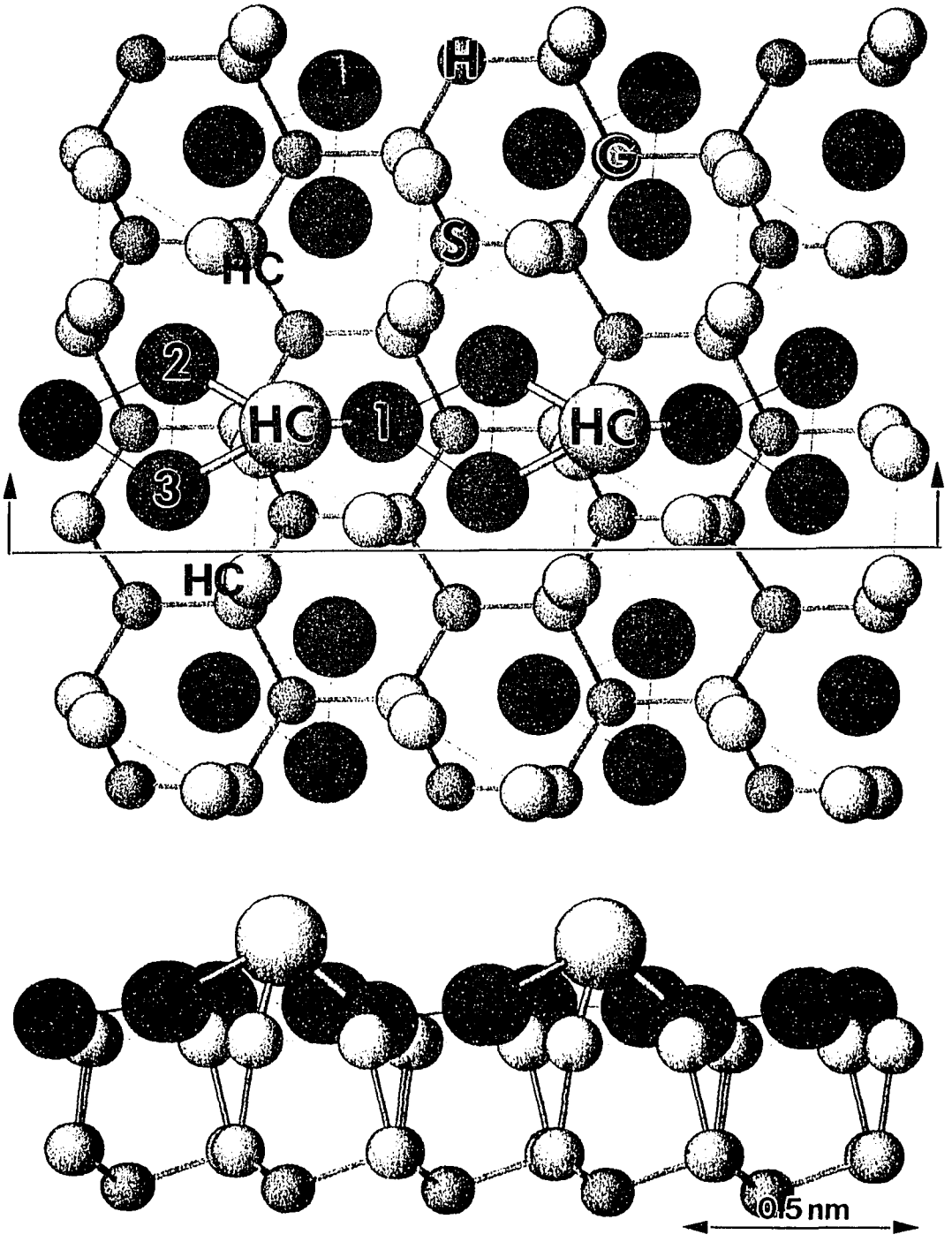


Figure 6.7. Top and side view schematics of two successive occupied Au honey comb sites (neighbored by two empty ones) relative to the pristine $\sqrt{3}$ Au structure. Arbitrary vertical displacements are based on stearic hinderance considerations.

beams respectively. The average Au distorted honeycomb (HC) adsorption site location parameters (listed in Table 6.1) were then measured from the resulting potential maps, some of which are shown in Figure 6.6. The average x-y plane projected interatomic distances (Figure 6.7) are Au HC to $Au_1$ = 2.12 Å ±0.20 Å, Au HC to $Au_{2,3}$ = 2.85 Å ±0.28 Å, Au HC to Si site = 0.59 Å ±0.20 Å. Figures 6.7 and 6.8 show that the Au HC site is close to one of the trimer gold atoms and probably leads to a buckling of the trimer. The site lies along the mirror plane of the structure if p3m1 symmetry is used (p3 symmetry was used throughout the analysis). Because of the limited number of beams in the data sets the silicon trimers are not well resolved. This lack of information leads to the weak features seen in Figures 6.6a and 6.6d.

The fact that the deposited Au prefers the $T_4$ like HC site to the high symmetry $\sqrt{3}$ Au sites (H, G, and S in Figure 6.7) confirms the point made by Bauer (1991) that with strong adsorbate-adsorbate and adsorbate-substrate bonding it is almost impossible to predict the adsorbate surface periodicity, let alone to predict the sites. The HC site does not seem to correlate cleanly to any of the other secondary Au bonding sites reported in the literature: not to the 5x2 Au protrusions (O'Mahony et al. 1992), nor to the partially occupied Au site atop the Au trimer (Dornisch et al. 1991), nor to the $\sqrt{3}$ Au domain wall sites (Plass and Marks 1995, Falta et al. 1995).

### *6.3.3 Consistency Checks*

A question which arises given this new site is why should the strongest (1,2)

and (4,0) beams of the structure linearly increase up to 1.0 ML. One could explain this increase in terms of the filling of empty trimer sites near vacancy domain walls with deposited gold (Plass and Marks 1996). This interpretation is inconsistent, though, with the rapid decrease of the higher order beams. If vacancy type domain walls do not fill with gold and are thus inherent to higher coverage structures, then we can calculate from the average $\sqrt{3}$ Au domain size, found by Nogami and coworkers (1990), that the saturation coverage of the $\sqrt{3}$ Au trimer site is between 0.84 and 0.87 ML in good agreement with RBS (Yuhara, Inoue, and Morita 1992b) and MEIS (Chester and Gustafsson 1991) results. Beyond this coverage gold would fill HC sites and we could expect that including the HC site into $\sqrt{3}$ Au structure refinements would at least modestly improve $\chi^2$. However, including the HC site with 0.1 site occupancy (0.3 ML gold) caused an increase in $\chi^2$ from 2.75 to 2.83. This shows the HC site is not inherent to lower coverage $\sqrt{3}$ Au structures.

Still, the changes of the diffraction spot strengths relative to each other seen in Figure 6.5 need to be explained. Therefore using the HC site parameters multislice simulations were done to compare the HC site's behavior with increasing site occupancy to that of other possible adsorption sites, namely the high symmetry location hollow, center of the silicon trimer, and center of the gold trimer adsorption sites (Plass and Marks 1996), shown in Figure 6.7. These diffraction pattern simulations show the HC site qualitatively matches all the trends in Figure 6.5 while the other adsorption sites do not. Interestingly, all the adsorption sites cause an increase in the strong (1,2) type spots. The key trend that distinguishes the structures

is the increase in the (4,0) spot. The decay of all beams after 1.0 ML can be interpreted in terms of the surface structure disordering mechanism associated with the HC site, discussed next.

### *6.3.4 Surface Structure Disordering / Amorphous Structure Formation Mechanism*

In the scattering potential maps the HC intensity changes relative to the Au trimer intensity (as seen in Table 6.1), the HC site relative intensity increases with gold coverage up to one monolayer and then remains relatively constant. While these intensity changes should not be over interpreted, these results, and the simultaneous decay of the $\sqrt{3}$ Au surface / formation of a disordered Au-Si structure, implies that a $\sqrt{3}$ Au structure with greater than a certain number of filled HC sites per unit cell is unstable. This is supported by the exponential decay of the strong beams of the structure. The key element of this disordering mechanism seems to be that the HC site gold atom weakens the surface to substrate bond of the $\sqrt{3}$ Au silicon atom. When this key bond breaks, the immediate Au-Si double layer structure collapses since it had been acting to compress the Si(111) surface (Plass and Marks 1995).

Given the formation mechanism of Si(111)-(2x1) upon UHV silicon cleavage, mentioned in Chapter 3 (which involves half the surface to substrate bonds breaking and reforming with other atoms), the room temperature Si-Si bond breakage causing surface disordering is possible. Additional evidence supporting the disordering tendency of the Au HC site comes from the increasingly diffuse nature of the $\sqrt{3}$ Au diffraction spots (Plass and Marks 1995, Takahashi, Tanishiro, and Takayanagi 1991).

As the $\sqrt{3}$ Au surface disorders, the domains effectively shrink and thus the spots become more diffuse.

### *6.3.5 Honeycomb Site Based Superstructures*

Since there are three rotationally different HC sites within the $\sqrt{3}$ Au structure and since it would seem only one of these sites is occupied per $\sqrt{3}$ Au unit cell before the structure decays, one could have different superstructures of HC sites at a certain Au coverage. Disordered arrangements of the rotationally different HC sites could also explain the $\beta$ $\sqrt{3}$ Au diffraction features. Thus the HC site could lead to a new family of superstructures that could explain the 6x6 Au and $\beta$ $\sqrt{3}$ Au surfaces. There is also no reason why this HC site family of features could not coexist with the domain wall family of features discussed in Section 6.2 or with some other features as yet undetermined.

This gold deposition study brings up one other feature, the $\sqrt{3}$ Au gold trimers contract by about 0.2 Å with the filling of HC sites. The reason for this is unclear but could be related to the presence of the bonds to the HC gold atom or to significant charge transferring away from the Au trimer atoms.

## 6.4 Conclusions

Given the variety of evidence for different features in $\beta$ $\sqrt{3}$ Au and 6x6 Au, plus the amorphous gold silicon structure, 3-D islands, and even a report of a Si(111)-($2\sqrt{3}$x$2\sqrt{3}$) Au surface (Yuhara, Inoue, and Morita 1992b), all in the 1.0 to 2.0 ML

range, more investigation into this part of the Au on Si(111) system is certainly warranted. More studies are needed to verify the presence and determine the roles of the three trimer surface motif, the six trimer surface motif, the vacancy and "neutral" domain walls, the honeycomb sites, and island chemical composition (and other, as yet unknown features) in these structures. Because of the disordered nature of both structures off-zone HREM images of the 6x6 Au and $\beta$ $\sqrt{3}$ Au surfaces (similar to those of 5x2 Au in Chapter 4) though difficult to obtain, would be invaluable. To minimize beam damage a good avenue for this investigation is to use a 200kV UHV-TEM. These studies were attempted at NEC's Fundamental Research Laboratory in Japan. However, due to an inexplicable inability to prepare a clean Si(111) sample, as well as other technical difficulties, the experiments were not carried out. Still, the ongoing direct phasing TED study of $\beta$ $\sqrt{3}$ Au will hopefully shed some light on the problem.

# 7 THE Au ON Si(111) SURFACE PHASE DIAGRAM

## 7.1 Introduction

Up to this point we have been discussing what the various gold induced Si(111) surface structures are individually with little regard for the driving forces that create them or how they interact with each other. Based on the atomic structures discussed in the previous four chapters and key materials science principles, this chapter focuses on understanding the driving forces and coexistence of the gold induced reconstructions through study of the Au on Si(111) surface phase diagram. The recent explosion of new surface science results concerning the gold on Si(111) system helps to fill in many of the gaps that existed in the phase diagram when the present study was begun. As a result, a review of the current literature of this area provides us with a Au on Si(111) surface phase diagram in contrast to the surface phase maps (Figure 7.1) which have been previously proposed (Ino 1988, Lelay 1983, Takahashi, Tanishiro, and Takayanagi 1991, Yuhara, Inoue, and Morita 1992a, Lelay, Manneville, and Kern 1977).

## 7.2 Au-Si(111) Phase Diagram

### *7.2.1 Coverage Calibration*

Before discussing the Au on Si(111) surface phase diagram the key issue of

determining the "saturation" coverages of the 5x2 Au and √3 Au phases needs to be addressed briefly because of the considerable confusion in the literature. The concept of saturation coverage, in itself, is misleading since, as we have seen in the previous chapters, 5x2 Au and √3 Au have the ability to vary their gold content to

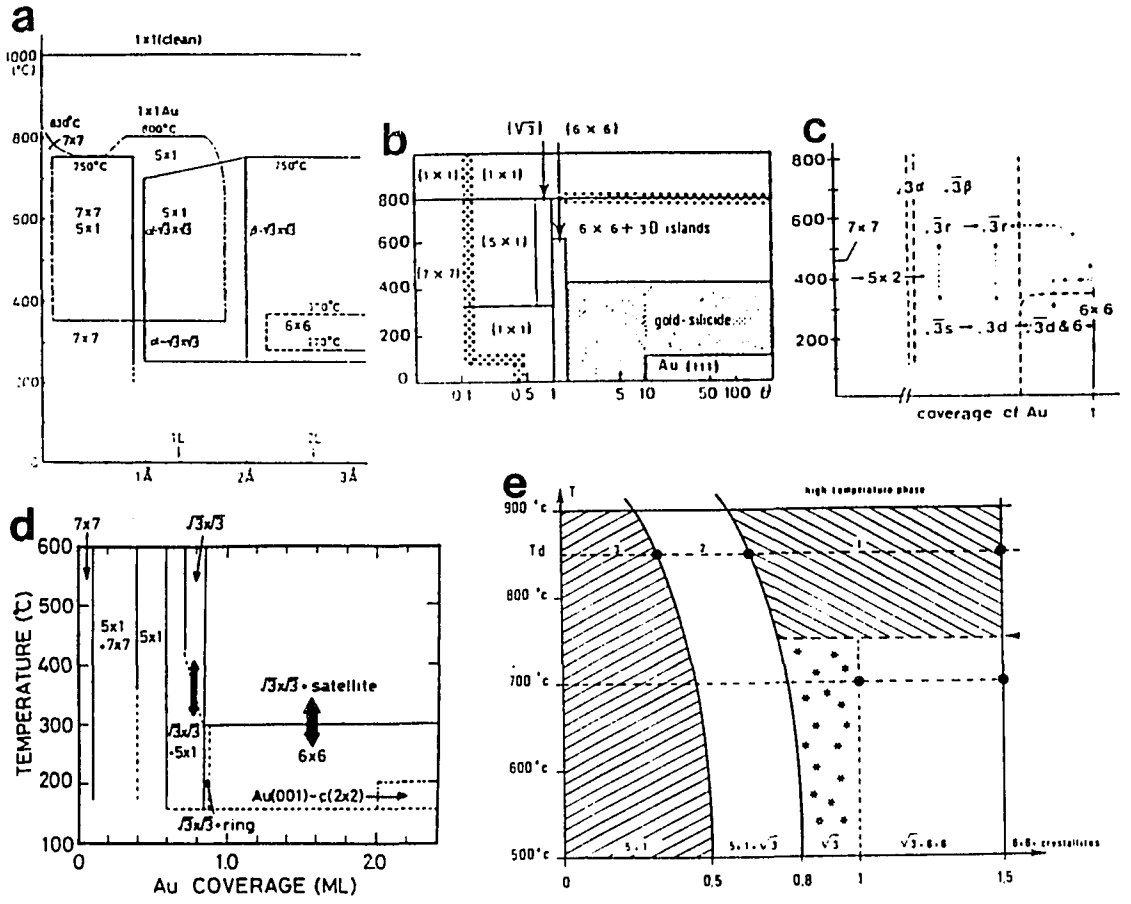


Figure 7.1. Various surface phase maps that have been proposed for the Au on Si(111) system by: a) Ino (1988), b) Lelay (1983), c) Takahashi, Tanishiro, and Takayanagi (1991), d) Yuhara, Inoue, and Morita (1992a), d) Lelay, Manneville, and Kern (1977).

some extent and, therefore, should be considered "surface solutions".

Thermodynamics then dictates that the total gold coverage range over which any of these surface phases completely covers the surface must vary with temperature. The

exact annealing and temperature measurement conditions vary from one study to another, this fact can partially explain the debate that still persists on this issue. However, the variations in reported saturation coverages are larger than the variations in the coverage expected from thermodynamics. For instance, the reported saturation coverages for 5x2 Au range from 0.4 ML (e.g. Lelay 1981, Marks and Plass 1995) to 0.8 ML (Seehofer et al. 1995) and for $\sqrt{3}$ Au range from 0.66 ML (Nogami, Baski, and Quate, 1990, Takami et al. 1994) to 1.17 ML (Seehofer et al. 1995). Given these discrepancies it is important to find an "anchor" coverage for each of these structures based on reliable, surface composition sensitive techniques.

For the 5x2 Au surface the HREM result discussed in Chapter 4 is the first component of the "anchor" while the STM protrusion result common to four groups (Baski, Nogami, and Quate 1990, O'Mahony et al. 1992, Hasegawa et al. 1990, Seehofer et al. 1995) is the second component. The HREM result conclusively shows that there must be at least four gold atoms per surface unit cell (but not significantly more) corresponding to a coverage of 0.40 ML. As was discussed in Chapter 4, in HREM the protrusions seem to blur or simply are not present. To obtain the occupancy of the fifth gold site we assume the protrusions seen in STM are gold atoms. While the differences in protrusion surface density seen (or not seen) by various groups will be discussed below, for now we assume the value of 0.32 per unit cell (Baski, Nogami, and Quate 1990) for a 5x2 Au "saturation" coverage of 0.432 ML. For the $\sqrt{3}$ Au "anchor" the RBS study (Yuhara, Inoue, and Morita 1992a, 1992b) value of 0.85 ML for the well annealed $\sqrt{3}$ Au surface seems most appropriate

since this surface shows no diffusion tail and the value agrees well with MEIS results (Chester and Gustafsson 1991). However, as was discussed in Chapter 5, the presence of vacancy type domain walls still makes this surface less reliable as a saturation coverage standard than the tighter coverage ranged 5x2 Au structure. Still, it provides some consistency check since coverage calculations based on the 5x2 Au "saturation" coverage can be compared to this value.

The main reason the 5x2 Au coverage anchor is important is that while almost all of the in-situ and annealed surface studies that contribute information to the surface phase diagram have their own coverage calibration, the pivotal LEEM study of Sweich, Bauer, and Mundschau (1991) does not. Instead it reports precise values of the saturation coverage ratios. Since this study provides many key pieces of in-situ information, a reliable standard calibration coverage must be determined so that its carefully measured ratios can be utilized. The study itself used an assumed $\sqrt{3}$ Au coverage of 0.66 ML; a recent study (Seehofer et al. 1995) reformulated the conclusions based on a 1.17 ML $\sqrt{3}$ Au saturation coverage. I believe the second formulation is in error since the resulting 5x2 Au coverage, 0.8 ML, is far too high. Surprisingly, the original formulation may not be far off. Therefore all LEEM coverage results are calculated based on a 5x2 Au saturation coverage of 0.432 ML.

### *7.2.2 Phase Diagram: General*

Figures 7.2 and 7.6 together give an overview of the results of all relevant experimental studies to date on the Au on Si (111) surface phase diagram. Figure 7.2

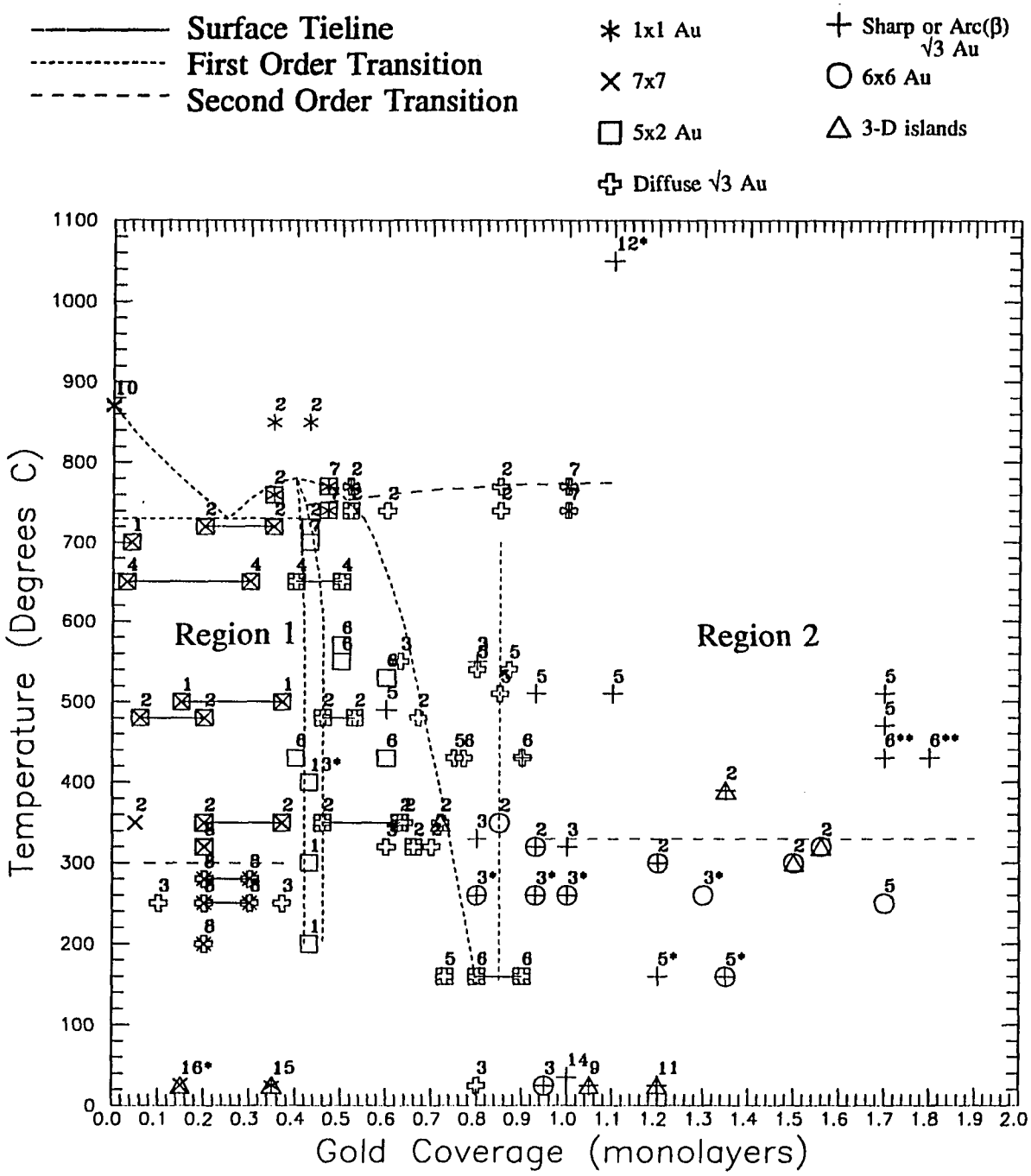
Surface Tieline
First Order Transition
Second Order Transition
1x1 Au
7x7
5x2 Au
Diffuse √3 Au
Sharp or Arc(β) √3 Au
6x6 Au
3-D islands
Region 1
Region 2
Temperature (Degrees C)
Gold Coverage (monolayers)
0
100
200
300
400
500
600
700
800
900
1000
1100
0.0 0.1 0.2 0.3 0.4 0.5 0.6 0.7 0.8 0.9 1.0 1.1 1.2 1.3 1.4 1.5 1.6 1.7 1.8 1.9 2.0

Figure 7.2. Au on Si(111) surface phase diagram with in-situ experimental results. In this and subsequent figures single symbols represent a surface completely covered by that symbol's surface structure. Overlapping symbols represent coexistence of the corresponding structures on the surface. For example ⊠ means 7x7 and 5x2 Au are both on the surface. Solid lines represent experimental tielines between surfaces with these mixed compositions. The short dashed curves are potential locations of first order phase transitions between different phase regions. These transition curves are not based on specific energies but could well be. Longer dashed curves represent second order transitions or irreversible transitions as discussed in the text. All data points (except the RBS studies; 5 and 6) have an expected error of at least ±.05 ML based on crystal monitor / AES limitations and a temperature error of at least ±10°C based on pyrometer limitations. Data points were taken either directly from the text of references or from coverage estimates based on the reference's images. The number above a data point corresponds to its reference as follows: 1 = (Hasegawa et al. 1991, Hasegawa, Hosaka, and Hosoki 1992, Hasegawa, Hosaka, and Hosoki 1996), 2 = (Sweich, Bauer, and Mundschau 1991), 3 = (Takahashi, Tanishiro, and Takayanagi 1991), 4 = (Tanishiro and Takayanagi 1989), 5 = (Yuhara, Inoue, and Morita 1992a), 6 = (Yuhara, Inoue, and Morita 1992b), 7 = (Diamon et al. 1990), 8 = (Shibata, Kimura, and Takayanagi 1992; this pivotal annealed study is included for clarity), 9 = (Fuchigami and Ichimiya 1996), 10 = (Miki et al. 1992), 11 = (Ichimiya et al. 1995), 12 = (Kamino et al. 1996), 13 = (Minoda et al. 1992), 14 = (Plass, Marks, and Dorset 1996), 15 = (Berman, Batterman, and Blakely 1988), 16 = (Meinel and Katzer 1992). Starred (*) reference numbers indicate the coverage was estimated.

shows all the in-situ studies, those in which the structure has been observed at the same temperature at which it was formed. Figure 7.6 shows all the annealed studies, where the structure was observed at a lower temperature than the one in which it was formed. The distinction between these two data types needs to be made since the cooling rate of an annealed structure determines its effective formation temperature. That is, a structure quenched from high temperatures may be equivalent to a structure that formed at a much lower temperature. The set of dashed curves, identical in Figures 7.2 through 7.6, represent potential phase boundaries but they have not been derived from any energy parameters. However, with more experimental data they could be used to derive the key energy parameters, as will be discussed below.

For clarity I will separate the in-situ phase diagram, and its explanation, into two separate regions: Region 1 - (Figures 7.3 and 7.4) coverages between 0 and 0.85 ML and Region 2 - (Figure 7.5) coverages 0.85 ML and higher. After discussing the in-situ results I will mention some aspects of the annealed studies.

### *7.2.3 Phase Diagram: Region 1*

This is currently the best studied and most interpretable region of the phase diagram. Figure 7.3 shows this region's thermodynamically stable phase diagram while Figure 7.4a highlights metastable data points and phase boundaries, Figures 7.4b, c and d illustrate schematic free energy curves. Inspection of the relative locations of the data in this region reveals that it is complex in nature, made up of lower coverage eutectoid and higher coverage peritectoid regions, if one assumes the

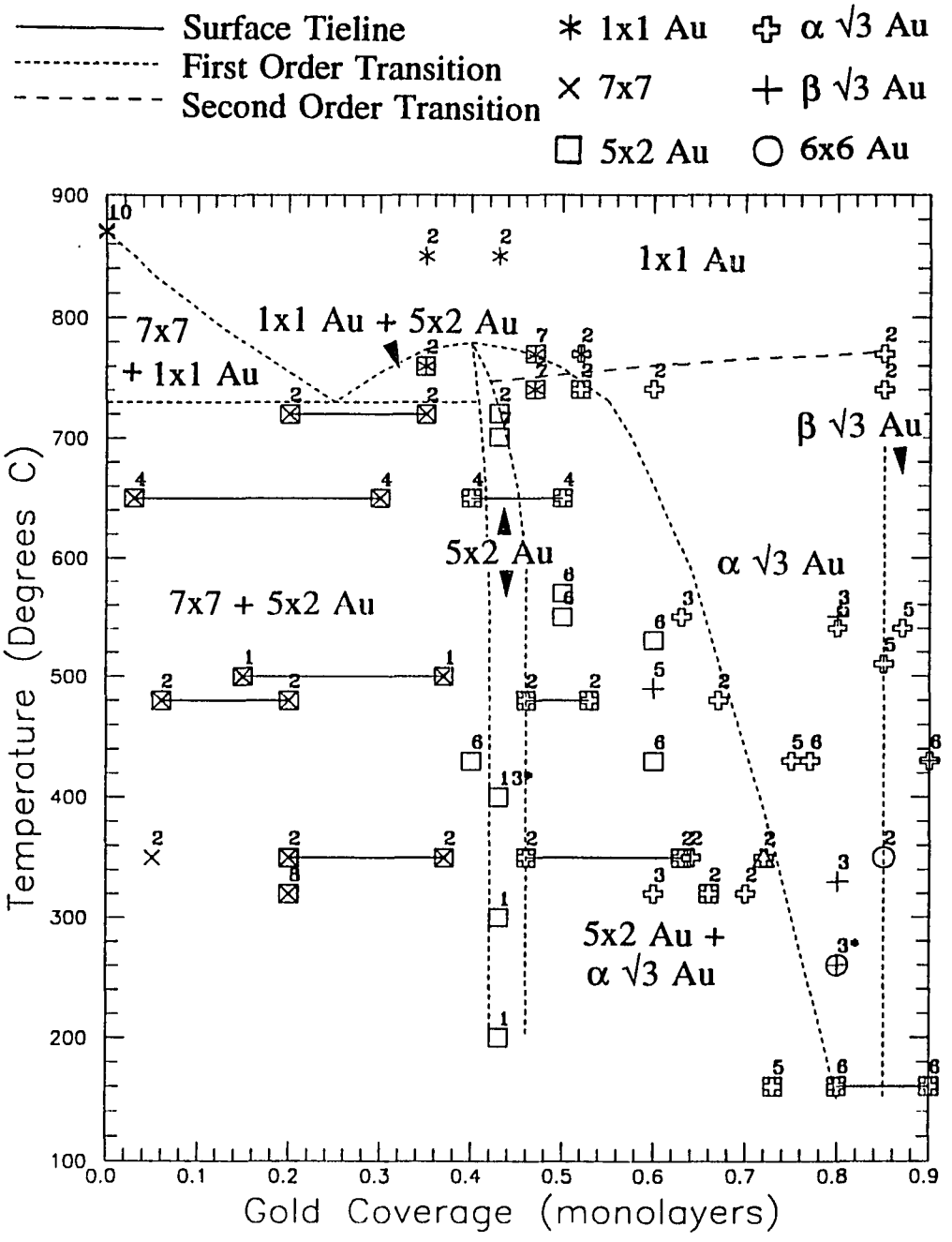


Figure 7.3. Magnification of Region 1 of the Au on Si(111) surface phase diagram with in-situ experimental results. The number above a data point corresponds to its reference as listed in Figure 7.2, dash length has the same meaning as in Figure 7.2. This plot only shows the thermodynamically stable phases and data points.

high temperature 1x1 and the $\sqrt{3}$ Au phases are related by a second order phase transition.

Among the data points shown in Figure 7.3 there are a handful that are pivotal in establishing the phase boundaries of the diagram. The first of these are the LEEM results of Sweich and coworkers (1991) and the RHEED results of Diamon et al. (1990) below, at, and above the saturation coverage of 5x2 for temperatures above 700°C. Together these results define parts of the 1x1 Au to 1x1 Au + 5x2 Au and the 1x1 Au + 5x2 Au to 7x7 + 5x2 Au phase boundaries. The LEEM results are particularly interesting in that they show anisotropic 5x2 Au growth and decay in the reversible 1x1 Au to 5x2 Au transition. (It should be noted, as shown by the arrowed curves in Figure 7.6 that for temperatures above 800°C the desorption of gold from the surface (Lelay, Manneville, and Kern 1977) means the system is not in true equilibrium unless gold is also condensing slowly from the vapor phase.)

Below the eutectoid/peritectoid temperature (around 730°C, in agreement with Ino's 1988 map, Figure 7.1a) several studies have shown that the 5x2 Au surface nucleates at surface steps and 7x7 domain walls (Sweich, Bauer, and Mundschau 1991, Hasegawa, Hosaka, and Hosoki 1996, Tanishiro and Takayanagi 1989). As the tielines in this region show, 5x2 Au domains grow to the extent of the amount of gold available. The LEEM results in the low gold coverage, 350°C area can be taken with some skepticism since the domain size is close to the LEEM resolution limit. Above the eutectoid/peritectoid temperature it is clear from LEEM that 5x2 Au and 1x1 Au coexist. This means that at some lower gold coverage there must be a eutectic point

between 5x2 Au + 1x1 Au, pure 1x1 Au, and 1x1 Au plus a 7x7 structure that may or may not have adsorbed gold in it (this point is arbitrarily shown at .25 Ml in phase diagram). Although this eutectic point as yet has no in-situ experimental evidence to back it, it is also seen in Ino's surface phase map (Figure 7.1a) and shows that the "melting point" and therefore 5x2 Au's binding energy is close to that of 7x7.

The scatter of data points for the pure 5x2 Au phase is rather large for the in-situ studies and even larger for the annealed studies. Hence the coverages of the phase boundaries defining the region of pure 5x2 Au are based on the microstructure aspects of the structure discussed in Chapter 4 while the results of Sweich and coworkers (1991) and Diamon and coworkers (1990) set the temperature limits. The phase boundaries bordering pure 5x2 Au curve and approach each other as they near the eutectoid/peritectoid temperature. This represents the fact that the gold protrusions become less and less stable (compared to the $\sqrt{3}$ Au trimer site) with increasing temperature. Hence the average protrusion density as well as the density's range becomes smaller with increasing temperature. This could mean 5x2 Au is not a true line compound even though, over most of the temperature range, it acts like one. (A line compound interpretation for 5x2 Au, i.e., a straight vertical line at about 0.43 Ml could also match the experimental data given its large scatter.) The curving of these boundaries toward lower coverage can explain why the 5x2 Au / $\sqrt{3}$ Au saturation coverage ratio, carefully measured by Sweich and coworkers (1991), remained constant over a large temperature range while other results (O'Mahony 1994) show the 5x2 Au saturation coverage itself decreases with increasing temperature.

The constant (with respect to temperature) 5x2 Au to √3 Au saturation coverage ratio provides a definite link between the phase boundaries that limit the 5x2 Au + √3 Au coexistence region. The 5x2 Au + √3 Au tielines, particularly the result of Yuhara and coworkers (1992a) at .75 ML and 150°C, as well as the 5x2 Au + √3 Au to 1x1 Au + √3 Au transition seen by LEEM at about 750°C, define the rest of the "liquidus" phase boundary.

The final key feature of this region is the second order phase transition seen between √3 Au and 1x1 Au. What evidence is there to support it? Consider the high temperature profile images of the gold covered Si(111) surface obtained by Kamino et al. (1996) (Figure 1.6). This image shows a surface layer with much stronger contrast than the bulk which has about the correct height for a missing top layer structure. If we then consider what the high temperature or "liquid" 1x1 Au surface must be, the gold is still in a missing top layer type configuration but thermal vibrations inhibit the formation of gold trimers. If the gold coverage is less than one monolayer, silicon double layer units must also be present to maintain layer continuity. Otherwise it would be expected the high gold desorption energy of √3 Au (Lelay, Manneville, and Kern 1977) would be significantly lower. Essentially, gold substitutes randomly into an ideal bulk terminated Si(111) surface and stabilizes it, much as excess silicon apparently does in clean, high temperature 1x1. As the temperature drops to somewhere around 750°C, strong Au-Au and Si-Si bonding leads to trimerization and the √3 Au structure as indicated by the almost horizontal curve in Figure 7.3. (The role of the domain walls will be discussed in Section 7.3.3).

Based on this second order transition argument, one would expect that in the range of about 600°C to 750°C the average Au trimer spacing will vary linearly from about 2.7 Å to 3.84 Å. (A similar effect is seen in the Pb on Ge(111) system as seen by Franklin et al. (1996).) Appropriate high temperature in-situ diffraction studies would easily verify the change in gold to gold spacing but unfortunately no direct studies of this type have been performed. However, RHEED studies (Hasegawa and Ino 1993) indirectly support this trend in finding that the average $\sqrt{3}$ Au domain size increases with temperature. Also, our electron beam damage mechanism, mentioned in Section 5.2.1, tends to confirm the hypothesis. The key data supporting the second order phase transition so far comes from the LEEM study in which Sweich reported that at temperatures above 700°C it was impossible to distinguish regions of 1x1 from $\sqrt{3}$ Au with LEEM's contrast mechanism despite the presence of $\sqrt{3}$x$\sqrt{3}$ diffraction spots in LEED. The near 3.84 Å Au to Au spacing in the 5x2 Au structure also shows the proposed second order transition is viable.

In principle, the positions of the phase boundaries of this system can be used to obtain rough to fair estimates of the thermodynamic parameters of the gold decorated 7x7, 5x2 Au, and $\sqrt{3}$ Au surface structures. Lupis (1983), for example, outlines such a procedure but it is not straightforward if the structures are not thermodynamically regular. Also some key thermodynamic relationships will likely have to be derived from total energy calculations first. Thus the above discussion is not meant as a complete thermodynamic analysis but more as a guideline for future

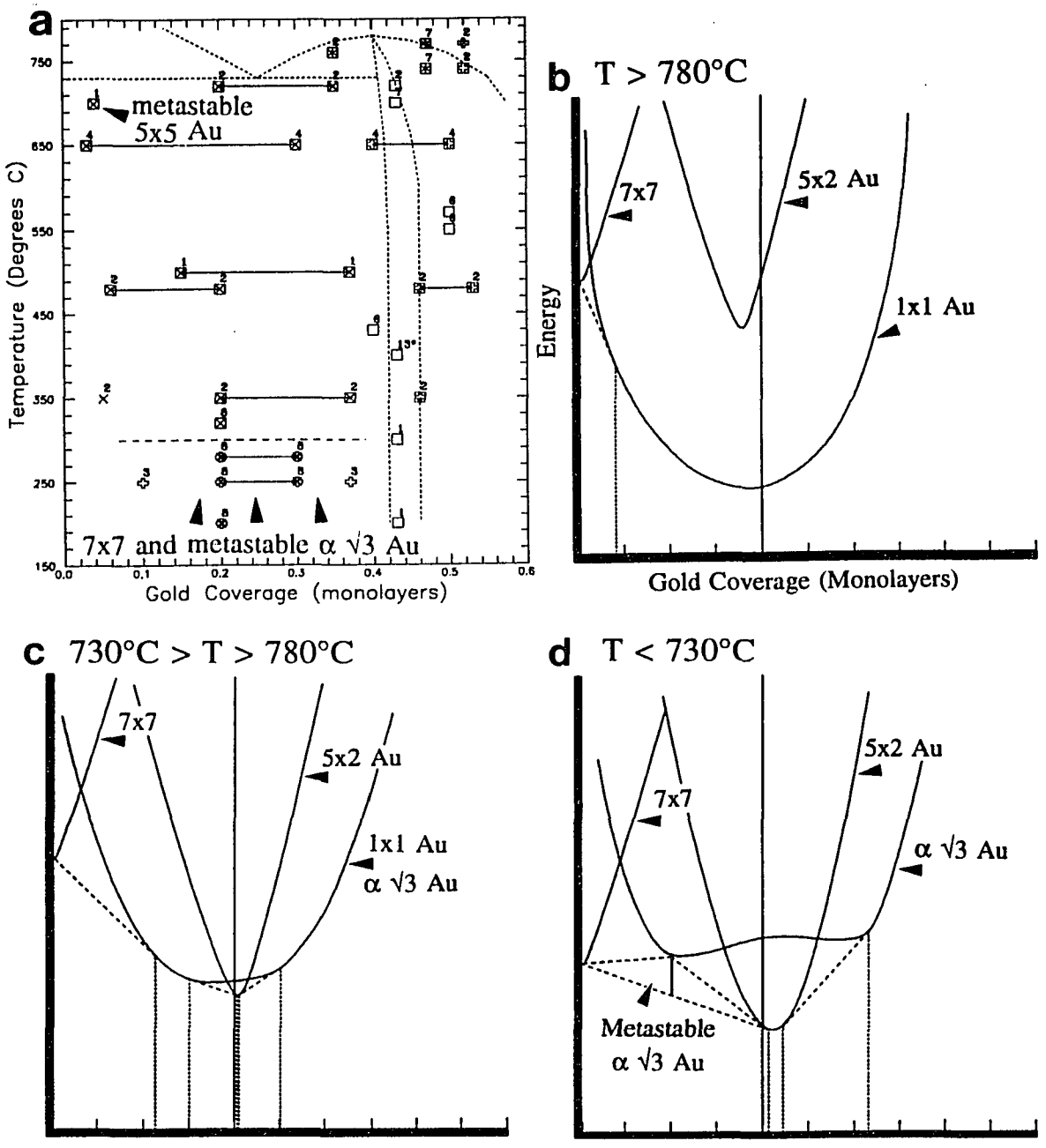


Figure 7.4. a) Magnification of Region 1 of the Au on Si(111) surface phase diagram highlighting the metastable surface structures. The number above a data point corresponds to its reference as listed in Figure 7.2. b-d) Schematic free energy curves which illustrate how the real free energy curves interact to generate the low coverage Au on Si(111) phase diagram features in b); the 780°C to 870°C, c); the 730°C to 780°C, and d); the below 730°C temperature ranges.

work. Figures 7.4b-d schematically illustrate how the free energy curves based on these thermodynamic parameters would have to interact to generate Region 1's phase diagram features, these curves also predict the presence of metastable $\sqrt{3}$ Au at low coverages.

Figure 7.4a illustrates two regions of metastable gold induced surface reconstructions delineated by long dashed curves, one of these regions has clear experimental evidence, the other's presence is less definite. The presence of both structures relies on slow kinetics which may arise from two factors: 1) a high activation barrier to removal of silicon from the 7x7 structure and/or nucleation of 5x2 Au or 2) slow silicon surface diffusion. As will be seen, evidence supports the latter factor.

The most obvious and important metastable structure is the metastable $\sqrt{3}$ Au at coverages below 0.4 ML. The phase diagram's nature at higher temperatures excludes the coexistence of 7x7 and $\sqrt{3}$ Au; therefore it is initially surprising to see them coexist at lower temperatures. The work of Tanishiro and Takayanagi (1989) and especially of Shibata, Kimura, and Takayanagi (1992), in identifying and characterizing the metastable $\alpha$ $\sqrt{3}$ Au structure in coverages between 0.2 and 0.4 ML and temperatures between 200°C and 280°C, is exceptional in that they also determined the island-hole pair formation mechanism (Section 5.1.2). The similarity in the irreversible transition temperature from 2x1 to 5x5 (350°C) and from low coverage $\sqrt{3}$ Au to 5x2 Au (300°C) is also striking. As Shibata and coworkers point out in proposing the hole-island mechanism, much less silicon transport is required to

form the √3 Au structure than to form 5x2 Au. The same "sluggish" silicon kinetics that drives the formation of 2x1 upon cleavage rather than the more stable 5x5 and 7x7 is also at work in the formation of √3 Au rather than 5x2 Au at these temperatures. (It was discussed in Chapter 3 that the metastable 2x1 structure arises because formation of the 7x7 structure requires substantial silicon displacements (Feenstra and Lutz 1991, Miki et al. 1992).)

The presence of metastable √3 Au leads to an important proposed conclusion. As in the case of the quenched 1x1 surface (Yang and Williams, 1994a, 1994b), the specific structure which forms depends more on the concentration of the mobile species present at the formation site than on the stress requirements of the surface. If plenty of mobile silicon is available the 5x2 Au surface grows from defect sites. If the surface is "mobile silicon starved," the √3 Au structure forms. A confirmation experiment for this conclusion would be to quench a clean 1x1 reconstructed surface to 200-250°C and hold it there while slowly depositing about 0.25 ML of Au onto it. Under these conditions, where "mobile" Si is readily available, we can see if it is the formation of 5x2 Au's double layer or the disruption of 7x7 that is the rate limiting step in the formation of 5x2 Au. If 5x2 Au readily nucleates and grows under these conditions then the disruption of 7x7 and/or Si surface diffusion are key. If √3 Au forms then the activation barrier to 5x2 Au nucleation is key.

The other metastable structure in Region 1 is based solely on Hasegawa's STM observation of an annealed 5x5 protrusion pattern on terraces at 700°C (Hasegawa et al. 1990). The theoretical coverage of these protrusions, 0.04 ML assuming they are

gold, establishes this structure's likely saturation coverage. Since not many unit cells of this surface were shown and since later studies have not confirmed this result, one wonders if it is not just a poorly ordered version of 5x2 Au. Still, this surface's possible presence shows that gold may find a loosely bound site within a DAS structure. As was discussed in Chapters 4 and 6 we have seen loosely bound gold sites in both the 5x2 Au and $\sqrt{3}$ Au structures. The fact that a 5x5 like structure forms when silicon (111) is decorated with gold (presumably in an adatom configuration) may show that the silicon atom density is dropping towards the 5x2 Au value of 1.5. (The pure DAS 5x5 structure has a silicon surface density of 2.0, with gold substituting for the Si adatoms this density drops to 1.76, 7x7 has a density of 2.08.) The metastability of "5x5 Au" compared to 5x2 Au may be related to the metastability of "pure" 5x5 compared to 7x7 between 350°C and 600°C (e.g., Feenstra and Lutz 1991). Along with the needed confirmation of the 1x1 Au + 7x7 Au coexistence region, the lack of information on this metastable phase shows more experiments are needed in the very low gold coverage region of the phase diagram.

### *7.2.4 Phase Diagram: Region 2*

In contrast to the numerous in-situ experimental results in Region 1 of the Au on Si(111) phase diagram, Region 2 (coverages greater than 0.85 ML, Figure 7.5) is potentially more complex but less studied. Hence not as many conclusions can be made about this region.

There are three principle reasons why there are fewer reliable data points in

this region. First, as we saw in the previous chapter, the high density of domain walls and the disorder they introduce severely limit the usefulness of diffraction techniques. Second, lack of electron beam robustness and the presence of superstructures

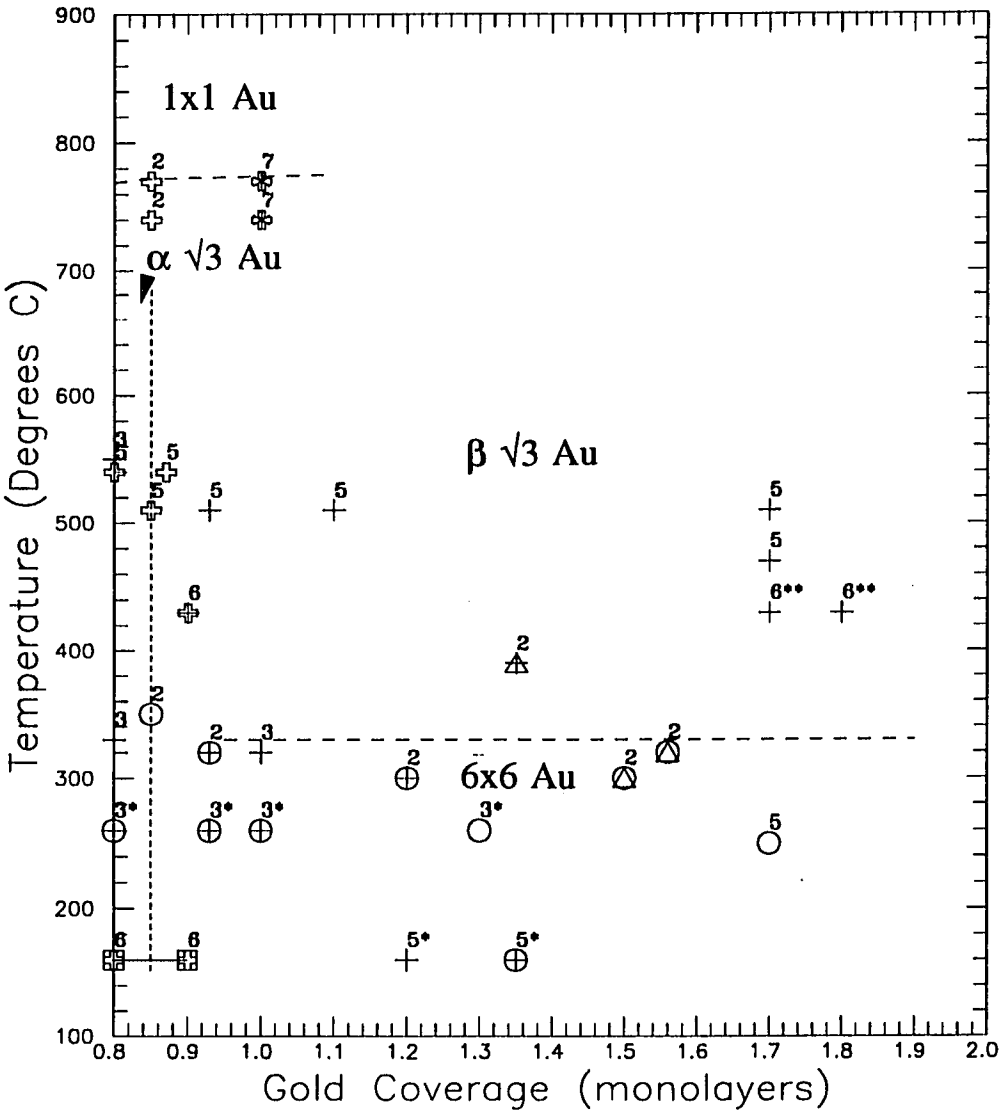


Figure 7.5. Magnification of Region 2 of the Au on Si(111) surface phase diagram with in-situ experimental results. The number above a data point corresponds to its reference as listed in Figure 7.2.

atop buried structures limit the usefulness of TEM and STM respectively. Third, as Yuhara and coworkers have pointed out (1992b), the slow diffusion of gold into the bulk at coverages greater than 0.85 ML and temperatures higher than 450°C makes the equilibrium and reproducibility of the structures studied a serious concern. The nucleation of 3-D islands (Sweich, Bauer, and Mundschau 1991) in this region further complicates matters.

Despite this region's difficulties in characterization we can note two key features. The first is the transition from diffuse to sharp spotted $\sqrt{3}$ Au diffraction spots around 0.85 ML. In surveying the literature to prepare the phase diagram the distinction was made between the $\alpha$ or diffuse spot $\sqrt{3}$ Au structure and the $\beta$ or sharp / arc surrounded diffraction spot $\sqrt{3}$ Au structure. This distinction is based on the work of Nogami et al. (1990) who found that the $\sqrt{3}$ Au domain wall density remained constant below roughly 0.85 ML while it increased for higher coverages. (This definition of $\beta$ $\sqrt{3}$ Au is different from that of Ino (1988) in including the sharp spot structure, a distinction he was ambiguous on.) The constant domain wall density makes $\alpha$ $\sqrt{3}$ Au a more "stable" structure in the discussion of the last section. It is important to note that while this distinction is based solely on an image criteria, the 0.85 ML distinction defines the "boundary" between $\alpha$ and $\beta$ $\sqrt{3}$ Au phases surprisingly well for the in-situ diffraction data. The connection is not necessarily obvious and this fact will likely have important theoretical consequences. The $\beta$ $\sqrt{3}$ Au structure itself is more properly described as a set of structures whose domain size depends on gold coverage and whose diffraction spot shapes vary as a function of

coverage, temperature, and sample history (Takahashi, Tanishiro, and Takayanagi 1991). Our studies of different coverages and temperature anneals in this region confirm most of the results of Takahashi and coworkers.

The second key feature of this region is the ordered to disordered phase transition between the 6x6 Au and $\beta$ $\sqrt{3}$ Au structures discussed in Section 6.2.2. Other features worth noting are the ubiquitous presence of gold islands in all the LEEM results in this region and the report of a Si(111)-($2\sqrt{3}$x$2\sqrt{3}$) Au structure at 1.7-1.8 ML and 430°C (Yuhara, Inoue, and Morita 1992b). The LEEM study found that the 3-D island movement trails inhibit formation of 6x6 Au. As was discussed in Section 6.4 much more study is required in this region before we can understand the energetics involved.

Looking now at the low (room) temperature regime of both regions; numerous studies of room temperature gold depositions onto the Si(111) surface have been undertaken, (Hiraki 1984 and Calandra, Bisis, and Ottaviani 1985 present good reviews of the topic) but for the present discussion we will only consider a few key results that help illustrate the system's kinetics. As one would expect from the relatively low temperature, the structure that forms upon gold deposition depends on what surface was there initially. This is most clearly demonstrated in the LEED / AES study of Meinel and Katzer (1992) in which gold deposited onto room temperature 7x7 form 3-D islands, Volmer-Weber or VW growth, while gold deposition onto the quenched 1x1 surface proceeded by Stranski-Krastanov or SK growth (islands nucleate at 2.2 ML). Our own studies of gold deposition onto 5x2 Au

(Section 4.5) show that disruption of the 5x2 Au surface depends on the gold deposition rate. Gold deposition onto $\sqrt{3}$ Au (Plass and Marks 1996, Ichimiya et al. 1995, Fuchigami and Ichimiya 1996) proceeds in the same SK growth mode as on the 1x1 surface. The gold honeycomb adsorption site may play a vital role in the disruption of the initial surface (Section 6.3). Berman, Batterman and Blakely (1988) found similar results to Meinel and Katzer for Au onto 7x7. Taken together these studies illustrate the rather tough nature of the 7x7 and 5x2 Au surfaces. (Section 6.2.4 discusses the amorphous Au-Si structure that forms as the SK layer structure.)

### *7.2.5 Annealed Studies*

As can be seen from the large number of annealed structure studies at 700°C in Figure 7.6, several researchers have followed a "standard recipe" in preparing gold induced surface reconstructions based on Lelay's determination that significant gold desorption starts above 800°C. The substantial scatter in these results likely originates from different (and poorly specified) cooling rates from the annealing temperature. Because of this, true equilibrium conditions between phases are probably not present. The loss of Au to the bulk at higher coverages (Yuhara, Inoue, and Morita 1992b) could also account for the large scatter in reported phase saturation coverages in these studies. Along with Bauer's suggestion (1991) of the need for more accurate coverage calibrations and measurements, detailed annealing procedures should be reported in future literature to make this data more useful.

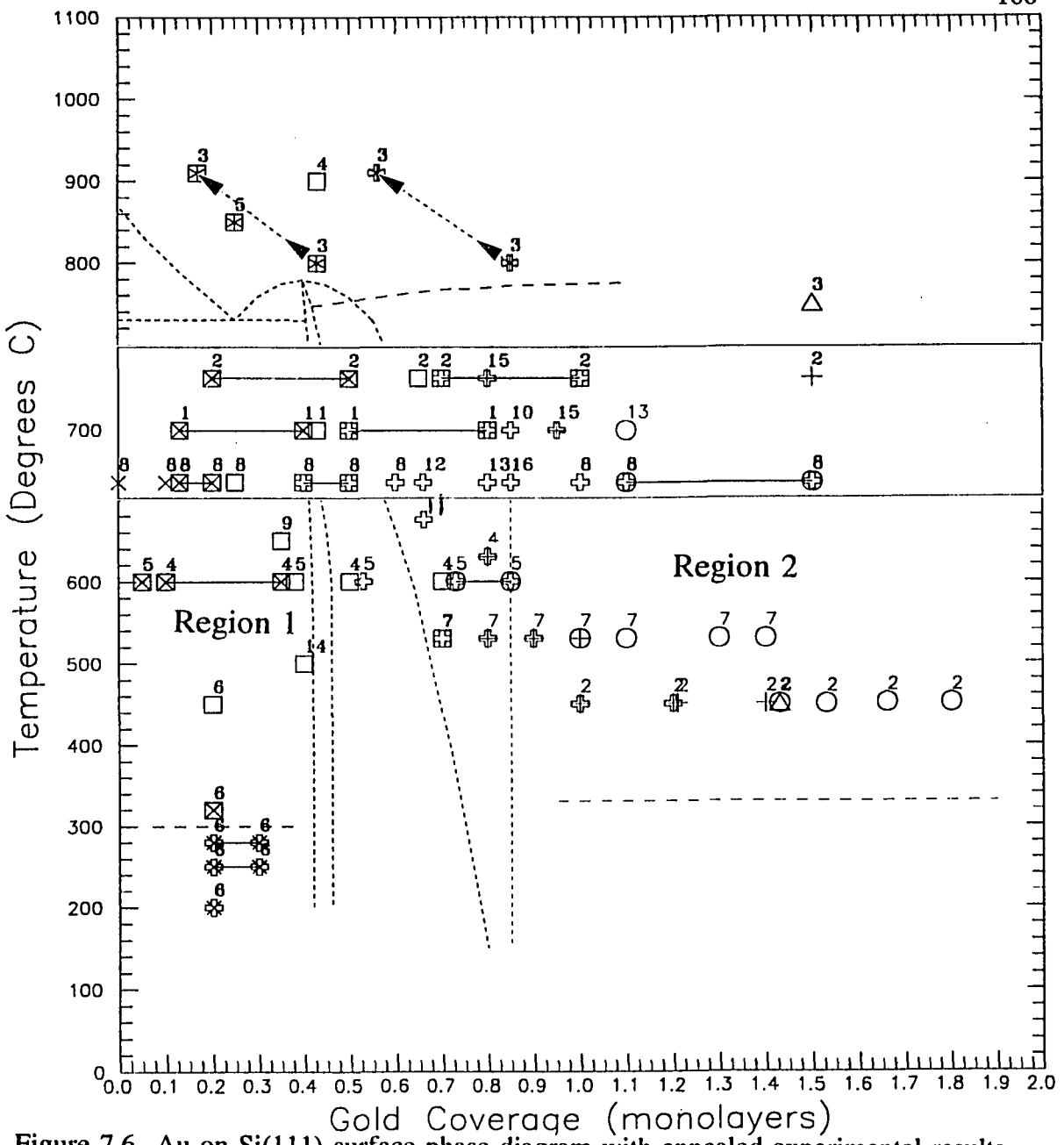


Figure 7.6 Au on Si(111) surface phase diagram with annealed experimental results. The dashed curves are the same as in Figure 7.2. In this figure numbers above a data point corresponds to its reference as follows: 1 = (Baski, Nogami, and Quate 1990), 2 = (Higashiyama, Kono, and Sagawa 1986), 3 = (Lelay, Manneville, and Kern 1977), 4 = (O'Mahony et al. 1992, O'Mahony et al. 1994), 5 = (Osakabe et al. 1980), 6 = (Shibata, Kimura, and Takayanagi 1992), 7 = (Takami et al. 1994), 8 = (Yabuuchi et al. 1983), 9 = (Berman, Batterman, and Blakely 1988), 10 = (Chester and Gustafsson 1991), 11 = (Dornisch et al. 1991), 12 = (Dumas et al. 1988), 13 = (Huang and Williams 1988a, 1988b), 14 = (Marks and Plass, 1995), 15 = (Nogami, Baski, and Quate 1990), 16 = (Quinn, Jona, and Marcus. 1992).

With that said, we can still conclude that the annealed data follows the same general trends as the in-situ data if the larger coverage uncertainties and much larger temperature uncertainties are taken into account. A notable exception is in one of the first comprehensive AES studies of the system, the study of Higashiyama, Kono, and Sagawa (1986, reference 2 in Figure 7.6). While their reported absolute coverages of the different surface phases are quite high (compared to the commonly accepted saturation coverages) their coverage ratios are in agreement with other values indicating a possible systematic error in their coverage calibration.

## 7.3 Summing it all up

We can summarize the information presented in this and the previous four chapters as well as extrapolate to new results through an approach taken by Duke and Lafemina. In their respective reviews of native semiconductor surfaces Duke (1994) and Lafemina (1992) discussed certain surface structure "motifs" as well as a set of underlying principles in clarifying what is fundamentally going on. After discussing comparable motifs and principles for the gold induced reconstructions (derived from all the data discussed so far) we will look at how they can help explain the driving forces of these structures.

### *7.3.1 Gold Induced Surface Structure Motifs*

First we note that $\sqrt{3}$ Au and 5x2 Au have a Au-Si double layer portion of their structures which are very similar (see, for instance, Figures 4.4 and 5.3). In 5x2

Au and $\sqrt{3}$ Au a gold atom's surface nearest neighbors are two gold atoms and three silicon atoms. In 5x2 Au one Si atom has three gold atoms around it while in $\sqrt{3}$ Au all the silicon atoms have three gold atoms nearby. The x-y projected silicon bonding distances to these three gold atoms are similar, i.e., $Si\text{-}Au_1$ = 2.07 Å for $\sqrt{3}$ Au and 1.94 Å for 5x2 Au, $Si\text{-}Au_2$ = 2.50 Å for $\sqrt{3}$ Au, 2.21 Å for 5x2 Au, and $Si\text{-}Au_3$ = 2.55 Å for $\sqrt{3}$ Au, 2.61 Å for 5x2 Au. (The discrepancy in $Si\text{-}Au_2$ arises because the formation of Si trimers in $\sqrt{3}$ Au pulls the Si away from this Au atom.) Since the vertical heights of the gold atoms above the silicon atoms are also similar in these structures (Berman, Batterman, and Blakely 1988, Kuwahara 1994) the gold's environment is essentially the same despite large differences in the overall structures. As discussed in Section 5.2.6, a key component of the $\sqrt{3}$ Au structure is charge transfer from Au to Si (Plass and Marks 1995, Dobrodey et al. 1994). While charge transfer was not statistically significant in the 5x2 Au $\chi^2$ analysis, the errors of the data set coupled with the inability to include subsurface relaxations and $Si^{--}$ scattering potentials in the analysis could act to mask possible charge transfer. The gold-silicon double layer is the first and most important gold induced surface structure motif. The Au-Si "skin" (Kamino et al. 1996) seen in high temperature profile HREM studies of several facets of silicon, as well as the structure of Si(100)-(5x3) Au (Lin et al. 1993, Jayaram and Marks 1995), show that variations of this motif apply to other silicon surfaces as well.

In the 5x2 Au structure, and less clearly in the vacancy domain walls of the lower coverage $\sqrt{3}$ Au structure, there is present a limited width, distorted silicon

double layer structure (at times decorated with silicon adatoms) that provides continuity between regions of the Au-Si double layer structure. This structure bears strong resemblance to the "partial 7x7" reconstructed strip seen by Suzuki, and coworkers (1996) in the vicinal (h,h,m) surface and to the 2x1 metastable reconstruction. The 5x2 silicon double layer strip consists of stretched adjacent silicon hexagonal rings while the (h,h,m) structure consists of hexagons and pentagons. The 2x1 structure consists of surface hexagons with subsurface pentagon and heptagon loops. The roughly 9 Å wide silicon double layer strips constitute the second gold induced surface structure motif.

Gold also seems to occupy less strongly bonded sites when it cannot occupy the missing top layer type site. These loosely bonded "decorative" sites are present in the "5x5 Au" (or gold decorated 7x7) surface (Hasegawa et al. 1990), in 5x2 Au, i.e., in the protrusions, and in the honeycomb site of $\sqrt{3}$ Au. The gold "decorative" sites are the third gold induced surface structure motif.

### *7.3.2 General Principles*

The work of Yuhara and coworkers (1992a,b), Chester and Gustafsson (1991), Kamino and coworkers (1995), and Wilk and coworkers (1994) makes it clear that below 0.85 ML, Au always stays on the surface. Above 0.85 ML Au will diffuse into Si, and with multiple Au layers Si will diffuse through Au (Green and Bauer 1974, Hiraki 1984). These and other facts lead to a "bonding hierarchy" with increasing gold coverage / distance to the surface, i.e.:

1) Au-Si bonds are strongest at surfaces, probably due to the surface's ability to stabilize significant charge transfer;

2) as the coordination around the Au and Si becomes more bulk like, Au-Au and Si-Si bonds will tend to dominate; and

3) silicon will always prefer to bond with Au rather than with oxygen if the temperature is sufficient to desorb the initial oxide layer. Together these bonding hierarchy rules make up the first principle.

The second principle is that kinetics, specifically surface diffusion, plays a very important role because it regulates the local availability of a species and therefore controls which phases will appear at a given temperature and coverage. This principle is essentially the same as the one that controls which quenched Si(111) metastable phases appear (Yang and Williams 1994a, 1994b).

### *7.3.3 Driving Forces*

Whether a certain structure is stable or not is governed both by its ability to eliminate dangling bonds and by the amount of "internal" stress built up in doing so. A factor which ties into the structure's internal stress is its ability to compensate for the tensile stress of the Si(111) surface (Robinson et al. 1988). That is, not only must a given structure have a configuration which allows stable bonding without extreme bond stress but, overall, the structure must apply a net compressive stress to the next substrate layer down to compensate for the silicon lattice that "was removed" in creating the surface. Just how large this net compressive stress is in relation to the

internal structure stresses (caused by reconfiguring to eliminate dangling bonds) is a matter of debate (e.g. Robinson et al. 1988, 1987a) but, as we will see, the current study concludes that it is relatively small.

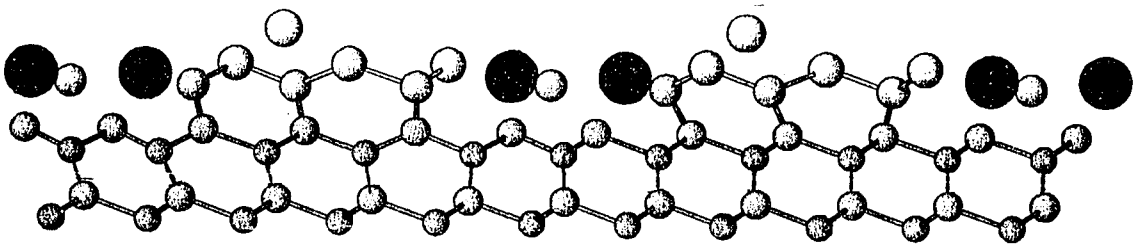

Figure 7.7. Side view schematic of the 5x2 Au model with (left), and without (right), qualitative relaxations in the second silicon double layer.

If we look carefully at the side view of the proposed 5x2 Au structure (Figure 7.7 right) we see significant tensile strain, 17%, in the silicon double layer. In comparison, the "strain" caused by silicon trimerization in the MTLTT $\sqrt{3}$ Au structure is about 21% relative to the layer to which it bonds, 26% in absolute terms. (Robinson et al. (1988) found an average tensile strain in the 7x7 structure of between 0.8% and 3.2% in 7x7 depending on the calculation method used.) Some of the tensile strain in 5x2 Au silicon-only region can come from lack of subsurface relaxations in the analysis which might cause all the projected atomic displacements to accumulate in the top (fitted) layer. If we qualitatively "relax" the second 5x2 Au double layer based on St. Verdant's principle and the measured $\sqrt{3}$ Au relaxations (3.9% in the upper and 1% in the lower silicon layer of the next double layer down), the resulting schematic, Figure 7.7 left, shows that the gold-silicon structure seems to

be drawing all nearby silicon atoms toward it. Presumably this is because of charge transfer and in accord with the first principle of bonding hierarchy. This means that the region around the gold silicon layer is under significant net compressive stress and explains the 1-D tensile strain of the silicon-only portion of the structure. We essentially have a situation of strong, balanced forces in which the 5x2 Au structure can compensate for a small "preexisting" surface tensile stress by moving like an accordion. As a result, the basic 5x2 Au structure is inherently quite stable and does not need to change much over a wide range of temperatures and coverages. Also, this interpretation explains the structure's growth anisotropy (e.g., Tanishiro and Takayanagi 1989, Hasegawa, Hosaka, and Hosoki 1996). 5x2 Au grows much more rapidly in the twofold direction than in the fivefold direction. The compressive / tensile stress pattern inherent in 5x2 Au explains this since in growing along the twofold direction the structure just adds gold and silicon atoms more or less simultaneously to the ends of rows already present, stresses are balanced as the rows elongate. However, in growth along the fivefold direction, a fairly large number of complete unit cells must assemble simultaneously to nucleate a new row. This is because either a gold-silicon portion or a silicon-silicon portion of the structure alone is unstable.

In contrast to the stability of the 5x2 Au structure, the nature of $\sqrt{3}$ Au changes substantially with temperature and coverage. This arises from the fundamentally different nature of the $\sqrt{3}$ Au internal stresses and the way $\sqrt{3}$ Au handles the Si(111) tensile stress. Unlike the predominantly 1-D stress mode of the 5x2 Au surface, $\sqrt{3}$

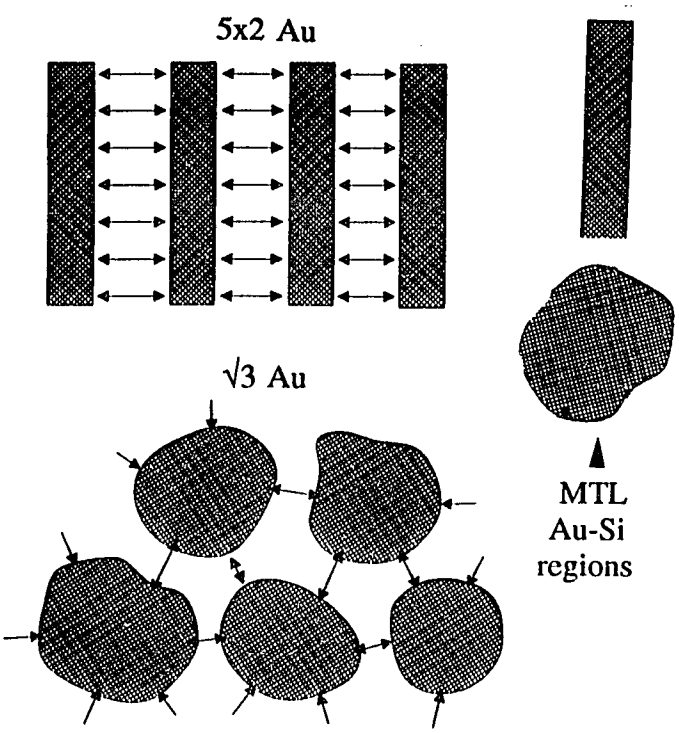


Figure 7.8. Schematic illustration of the 1-D nature of inherent stresses in 5x2 Au versus their 2-D nature in √3 Au.

Au acts in a 2-D mode as shown in Figure 7.8. From the high static gold Debye Waller term of √3 Au we can surmise that √3 Au has compressively stressed domain centers with the stress dropping as one moves radially away from the domain centers. Therefore the domain walls must be under tensile stress. From the fact that the metastable √3 Au surface (Shibata, Kimura, and Takayanagi 1992) has domains roughly the same size as the maximum average size found by Nogami, Baski, and Quate (1990), about 50 Å, we can conclude that this is the optimum domain size at lower temperatures and could find a corresponding compressive stress to generate it. (With proper isotropy and domain size compensation this should be the about same compressive stress as generated by the 5x2 Au gold-silicon structure.) One would expect the optimum domain size to increase with increasing temperature since larger vibrations reduce gold's bonding strength and hence the compressive stress. This prediction is confirmed by RHEED (Hasegawa and Ino 1993). One can argue that the exact opposite stress behavior is seen in √3 Ag (e.g., Takahashi and Nakatani 1993, Jia, Zhao, and Yang 1993), silver

decorates the three "tensile stressed" domain walls that surround the "compressively stressed" silicon trimers to form a stable long range structure.

The inherent stress system of $\sqrt{3}$ Au works well for lower $\sqrt{3}$ Au coverage structures and especially for higher temperatures (as is evident from the curve of the 5x2 Au+$\sqrt{3}$ Au to $\sqrt{3}$ Au phase boundary toward lower coverages). However, the system seems to break down for coverages above 0.85 ML since the domains appear to shrink linearly with coverage above this value (Nogami, Baski, and Quate, 1990, Takami et al. 1994). The silicon-silicon $\sqrt{3}$ Au domain walls have a limited minimum width beyond which the silicon-to-silicon bonds would break and the layer would lose continuity. Therefore above a certain coverage (presumably 0.85 ML) this system no longer applies and a new pattern of secondary gold sites and/or more domain walls must form. The conclusion concerning the driving forces of $\sqrt{3}$ Au is that they are driven more by chemical potential, that is, by the species locally available, rather than by surface tensile stress compensation (Plass and Marks 1995). This confirms Vanderbilt's hypothesis that the role of surface tensile stress is small compared to other factors (1987a).

One piece of evidence that supports the hypothesis that the gold-silicon structure motif applies a net compressive stress stronger than what is needed to balance the "preexisting" surface tensile stress comes from the Au-Au spacings of the various surface structures. The average Au-Au spacing in 5x2 Au is 4.14 ± 0.29 Å, 2.78 Å in lower coverage $\sqrt{3}$ Au, 2.67 Å in higher coverage $\sqrt{3}$ Au, and 2.59 Å in the amorphous Au-Si structure, compared to 2.88 Å in bulk gold. While these results

assume the Au-Au bond remains horizontal (a big assumption for the amorphous case) we can see in this progression (and especially from the "free floating" amorphous structure result) that the gold-silicon combination wants to apply a strong compressive stress to the surface.

A final, subtle point worth noting is that in the formation of all these various gold induced structures, surface diffusion of both species but especially silicon plays a vital role. From the high temperature behavior of the 1x1 to 7x7 transition (Miki et al. 1992) we can see that large unit cell structures are only stable in fairly complete forms. Fractions of a 7x7 unit are generally not stable adjoining another phase such as 1x1. Also, Suzuki et al. (1996) have shown 7x7 is stable only as whole units unless it is on an unusual vicinal surface. Thus the dynamic process of 7x7 unit cells forming and dissipating requires a lot of silicon atoms falling into place within the horizontal scan time of the STM and hence requires a lot of silicon surface diffusion (Miki et al. 1992). In this respect 5x2 Au is similar to 7x7 since it requires substantial silicon rearrangement to form. The "smaller" structures such as 2x1, $\sqrt{3}$ Au, or 6x6 Au form readily at lower temperatures since they require less silicon rearrangement. This is evident from the presence of the metastable $\sqrt{3}$ Au surface. But, large or small, surface structures form or dissolve at their domain edges, even in the hole-island pair mechanism (Shibata, Kimura, and Takayanagi 1992). The ramification is that surface diffusion is one of, if not the key, process in any type of surface domain growth / decay system and thus is important in epitaxy. This fact can may be critical in

explaining Wilk's essentially perfect gold mediated Si(111) homoepitaxy result (Wilk et al. 1994).

## 7.4 Conclusion

We are now in a position where, with a few final careful experiments and some theoretical number crunching, we can determine the key microscopic and macroscopic thermodynamic parameters of 5x2 Au and $\sqrt{3}$ Au and see if they match. If they do match we can say the low coverage Au on Si(111) system has been adequately characterized.

# 8 FUTURE WORK

## 8.1 Motivation

In the present study, and in other investigators' parallel studies, we have collectively answered many of the "what is it?" type questions of the Au on Si(111) system. In Chapter 7 we have begun to look at the "so why is it here?" questions but given the complexities of this system, more research is needed. What would be the possible rewards of continuing this effort? Wilk and coworkers' study points to the possibility of forming energetically stable gold decorated interface structures with unusual electronic properties since they showed that submonolayer amounts of gold will not be included in bulk silicon where it forms electronic traps deep in the silicon energy band (Wilk et al. 1994). In tackling these Au on Si(111) "why" issues we can address the questions already raised in this thesis and summarized in the next section, or we can use a novel, fairly new avenue of inquiry discussed in Section 8.3 for which preliminary data have already been obtained.

## 8.2 Cleanup

As with most scientific inquiries, this study has advanced our understanding of the Au on Si(111) system but in the process, has raised at least as many questions as were answered. I have already posed most of these questions in discussing results in the last four chapters, along with avenues for future research to answer them. The

potentially most fruitful future work can be summarized as follows.

1) Gold deposition onto a quenched 1x1 surface held at about 250°C should be performed to see if 5x2 Au nucleates and grows under these conditions in order to answer activation barrier and surface diffusion questions.

2) AFM of the 5x2 Au surface may prove useful in confirming or dismissing the TED based model.

3) Off-zone 200kV UHV-HREM of the $\sqrt{3}$ Au and 6x6 Au surfaces at several coverages will go a long way in conclusively determining the nature of the $\alpha$ $\sqrt{3}$ Au domains, the domain walls, and possible secondary gold sites in $\beta$ $\sqrt{3}$ Au and 6x6 Au. However beam damage will have to be monitored carefully.

4) Elevated temperature diffraction studies should be performed on $\sqrt{3}$ Au at about 0.80 ML to see if the Au-Au trimer spacings change with temperature as the phase diagram seems to predict.

5) And finally, microscopic total energy type calculations on 5x2 Au and MTLTT $\sqrt{3}$ Au as well as macroscopic determination of free energy parameters based on the Au on Si(111) phase diagram need to be carried out to fully understand the roles of the surface motifs, principles, and driving forces discussed in Chapter 7.

Another possible avenue of investigation would be to study the Ag on Si(111) system, especially the Si(111)-(3x1) Ag reconstruction (e.g. Wan, Lin, and Nogami 1993, Ohnishi et al. 1994), since this linear structure is expected to be related to 5x2 Au. Together these two structures can explain what the advantages are in noble metals forming low coverage linear structures versus dimer-adatom-stacking fault or

$\sqrt{3}x\sqrt{3}$ type structures. In this vein the Si(111)-(4x1) In system is also of interest.

## 8.3 Thin Film Intrinsic Stress Studies

An interesting point that the XPS spectra of the 5x2 Au and $\sqrt{3}$ Au surfaces raise is that while gold is only present on one surface (within detectable limits) the 7x7 reconstruction is missing from both surfaces! This phenomena was seen repeatedly for both the 5x2 Au and $\sqrt{3}$ Au surfaces. The only time 5x2 Au was seen to coexist with 7x7 is for top surface coverages around 0.25 ML. A detailed HREM analysis of fairly thick sample regions with 5x2 Au on the top surface revealed that the bottom surface was disordered but the annealing temperature to form 5x2 (roughly 550°C) was not near the 7x7 to 1x1 transition (870-850°C, Miki et al. 1992) so 7x7 should still be present on the bottom surface. One might say that the faster beam induced damage of HREM on the bottom surface is disordering the bottom 7x7 surface. However, the diffraction patterns should then show the 7x7 spots in regions where no HREM was performed. The bottom surface reconstruction must disorder during the deposition of gold or during the anneal. Why should the presence of either 5x2 Au or $\sqrt{3}$ Au on one surface of a TEM sample with varying thickness disorder the 7x7 structure on the other surface? While we do not know the answer to this puzzle, a possible explanation involves the intrinsic stress created by the "thin film" as the gold is deposited.

As has been discussed in detail by Koch (1994), thin film intrinsic stress exhibits two general modes of behavior based on what type of growth mode the thin

film exhibits. If the film exhibits Volmer-Weber (VW) type growth (Venables, Spiller, and Hanbucken 1984), that is, islands, the system exhibits hardly any stress until the islands start to percolate; then the intrinsic thin film stress rises geometrically (Koch 1994). For Stranski-Krastanov (SK) growth, however, the stress rises very steeply at the onset of deposition then stabilizes to a more or less constant value (Koch 1994). Of the two systems VW intrinsic stress has been studied in far more, detail whereas to date only two works have been published on SK thin film growth intrinsic stress (Schell-Sorodin and Tromp 1990, Koch, Winau, and Rieder 1993) which makes further study all the more worthwhile.

Our preliminary data in this area come from the Au deposition study video tapes. By tracking the intensity changes of the bulk beams and simulating them using different crystal tilts, we found the local crystal tilt varied during the deposition. Crystal tilt changes occurred for room temperature gold depositions onto both the 5x2 Au and $\sqrt{3}$ Au surfaces. From the crystal tilt change we can, in principle, calculate the thin film intrinsic stress.

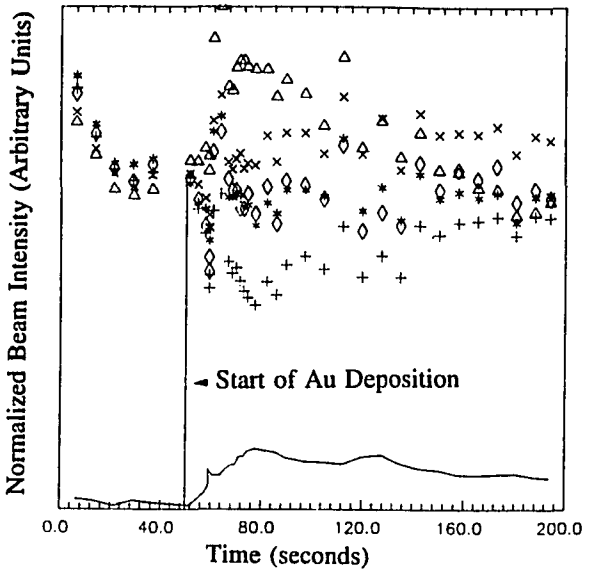


Upper Data Points - 5 bulk beam intensities

Lower Curve - Plot of an error function which roughly approximates the change in crystal tilt.

Figure 8.1. Plot showing the intensity changes of the bulk Si beams during Au thin film deposition.

Looking at one of the gold deposition runs onto $\sqrt{3}$ Au in detail, where experimental diffraction patterns were taken before and after gold deposition, the sample tilted locally by 0.53°±0.04°. The video tape recorded silicon bulk beam intensity changes corresponding to this tilt change. That is, the intensity changes correspond to a sharp initial tilt change at the start of deposition, followed by a broad maximum and finally a gradual small decrease, as shown in Figure 8.1. This behavior was qualitatively similar to intrinsic stress studies of the other SK growth systems.

Unfortunately, the local sample geometry for the measured tilt change run was not measured, so the actual intrinsic stress could not be determined. Even if the local sample geometry was measured carefully using PEELS, the thinning process we use in the final stages of sample preparation creates a "swiss cheese" perforated sample, as discussed in Section 2.2.2. this makes getting meaningful stress measurements quite difficult because the sample geometry varies significantly from the thin region under the beam to the stationary edge of the sample. To explore this avenue further we will require much better control

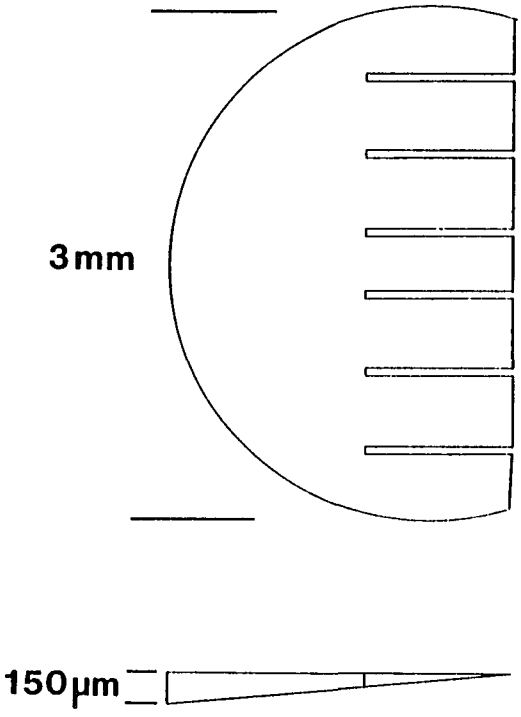


Figure 8.2. Top and side views of a TEM sample with cantilevers cut into it.

of the sample geometry so that reasonably precise stress values for the process can be obtained. This will require tripod polishing to prepare a wedge shaped bulk sample. Once cleaned under UHV conditions this wedge will be cut repeatedly with an ion beam along the direction of increasing thickness to form cantilevers for the thin film deposition studies (Figure 8.2). While it is relatively straightforward to do this procedure, the samples will be inherently fragile, a problem for SPEAR's sample transport mechanisms. Getting the sample to be 7x7 reconstruction level clean and relatively defect free while still maintaining the initial geometry could also be quite difficult. It must be remembered that in our normal sample preparation method the thinning acid etch also removes the scratches and contamination caused by the polishing process. A tripod polished sample could only receive a very brief etch at most.

Once clean cantilevers have been prepared, several worthwhile studies could be pursued. I will mention briefly only one set of studies: same metal deposition onto vicinal, metal induced, linear reconstructions. As O'Mahony et al. (1994) and Seehofer et al. (1995) have shown, vicinally cut surfaces can cause one of the three surface rotated linear reconstructions to be the dominant reconstruction on the surface. If two types of cantilevers are prepared, one with the surface vicinal steps running parallel to the long side of the cantilever (in the case of 5x2 Au the twofold direction would be going along the cantilever) and another with the vicinal steps running perpendicular to the cantilever (the twofold direction would be running across the cantilever), one would expect a significant difference in the tilt change response of

these two structures, both as the reconstructions are formed, and as they are destroyed by further metal deposition at various temperatures. These results will have important ramifications in understanding the dynamics of linear metal induced reconstructions and would almost be required if useful 1-D type device structures are to be made. (In the process, we may also answer the question of what happened to the 7x7 reconstruction on the other surface.) I have outlined this approach with the well studied 5x2 Au and 3x1 Ag reconstructions in mind but the general experimental framework would work with Si(100) based reconstructions as well.

# REFERENCES


Andersen, G. A., J. L. Bestel, A. A. Johnson, and B. Post. 1971. Eutectic Decomposition in Gold-Silicon System. *Material Science and Engineering* 7:77-82.

Akiyama, K., K. Takayanagi, and Y. Tanishiro. 1988. UHV electron microscope and diffraction analyses of the $\sqrt{3}x\sqrt{3}$ structure formed by Pd on Si(111) 7x7. *Surface Science* 205:177-186.

Azim, M., C. J. Harland, T. J. Martin, R. H. Milne, and J. A. Venables. Cesium on Si(100) studied by biassed secondary electron microscopy. *Scanning Microscopy.* 7:1153-1160.

Baski, A. A., J. Nogami, and C. F. Quate. 1990. Si(111)-5x1-Au reconstruction as studied by scanning tunneling microscopy. *Physical Review B* 41:10247-10251.

Bauer, E. 1985. The resolution of the low-energy electron reflection microscope. *Ultramicroscopy* 17:51-56.

_____. 1991. The Si(111)-(5x1) Au structure. *Surface Science Letters* 250:L379-L382.

_____. 1994. Low energy electron microscopy. *Reports on Progress in Physics* 57:895-938.

Becker, R. S., J. A. Golovchenko, E. G. McRae, and B. S. Swartzentruber. 1985. Tunneling images of atomic steps on the Si(111) 7x7 surface. *Physical Review Letters* 55:2028-2031.

Becker, R. S., J. A. Golovchenko, G. S. Higashi, and B. S. Swartzentruber. 1985. New reconstructions on silicon (111) surfaces. *Physical Review Letters* 57:1020-1023.

Bennett, P. A., M. Y. Lee, S. A. Parikh, K. Wurm, and R. J. Phaneuf. 1995. Surface phase transformations in the Ni/Si(111) system observed in real time using low-energy electron microscopy. *Journal of Vacuum Science and Technology* 13:1728-1732.

Berman, L. E., B. W. Batterman, and J. M. Blakely. 1988. Structure of submonolayer gold on silicon (111) from x-ray standing-wave triangulation. *Physical Review B* 38:5397-5405.

Binning, G. and H. Rohrer. 1987. Scanning tunneling microscopy - from birth to adolescence. *Review of Modern Physics* 59:615-620.

Bisi, O., C. Calandra, L. Braicovich, I. Abbati, G. Rossi, I. Lindau, and W. E. Spicer. 1982. Electronic properties of metal-rich Au-Si compounds and interfaces. *Journal of Physics C* 15:4707-4716.

Bishop, H. E. and J. C. Riviere. 1969. LEED of the gold silicon surface. *Journal of Physics D* 2:1635-1642.

Bootsma, G. A., and H.J. Gassen. 1971. A quantitative study on the growth of silicon whiskers from silane and germanium whiskers from germane. *Journal of Crystal Growth* 10:223-234.

Born, M. and E. Wolf. 1980. *Principles of Optics*. 6th ed. Oxford: Pergamon Press.

Burger, R. M., J. A. Glaze, T. Seidel, and O. Williams. 1995. The SIA's Roadmap: consensus for cooperation. *Solid State Technology* February:38-43.

Calandra, C., O. Bisi, and G. Ottaviani. 1985. Electronic Properties of silicon-transition metal interface compounds. *Surface Science Reports* 4:271-364.

Cherns, D. 1974. Direct resolution of surface atomic steps by transmission electron microscopy. *Philosophical Magazine* 30:549-557.

Chester, M. and T. Gustafsson. 1991. Geometric structure of the Si(111)-($\sqrt{3}$x$\sqrt{3}$)R30°-Au surface. *Surface Science* 256:135-146.

Coene, W., G. Janssen, M. Op de Beeck, and D. Van Dyck. Phase retrieval through focus variation for ultra-resolution in field emission transmission electron microscopy. *Physical Review Letters* 69:3743-3747.

Cochran, W. 1955. Relations between the phases of structure factors *Acta Crystallographica* 8:473-478.

Collazo-Davila, C., E. Landree, D. Grozea, G. Jayaram, R. Plass, P. C. Stair, and L. D. Marks. Design and Initial Performance of an Ultrahigh Vacuum Sample Preparation Evaluation Analysis and Reaction (SPEAR) System. *Journal of the Microscopy Society of America* 1:267-279.

Collins, I. R., J. T. Moran, P. T. Andrews, R. Cosso, J. D. O'Mahony, J. F. McGilp, and G. Margaritondo. 1995. Angle-resolved photoemission from an unusual quasi-one-dimensional metallic system: a single domain Au-induced 5x2 reconstruction of Si(111). *Surface Science* 325:45-49.

Cowley, J. M. 1990. *Diffraction Physics.* 2nd rev. ed.. Amsterdam: North-Holland.

Cowley, J. M. and A. F. Moodie. 1959. The scattering of electrons by atoms and crystals, III. Single-crystal diffraction patterns. *Acta Crystallographica* 12:360-368.

Cros, A., F. Houzay, G. M. Guichar, and R. Pinchaux. 1982. Passivation of Si(111) surfaces by ordered metal layers. *Surface Science* 116:L232-L236.

Davisson C. J. and L. H. Germer. 1927. Diffraction of electrons by a crystal of nickel. *Physical Review* 30:705-740.

Dennis, J. E., D. M. Gay, and R. E. Welsch. 1981. An adaptive nonlinear least-squares algorithm. *ACM Transactions Mathematical Software* 7:348-383.

Diamon, H., C. Chung, S. Ino, and Y. Watanabe. 1990. A study of Si(111)5x2-Au structures by Li adsorption and their coadsorbed superstructures. *Surface Science* 235:142-155.

Ding Y. G., C. T. Chan, and K. M. Ho. 1992. Theoretical investigation of the structure of the ($\sqrt{3}$x$\sqrt{3}$)R30°-Au/Si(111) surface. *Surface Science Letters* 275:L691-L696.

Dornisch, D., W. Moritz, H. Schulz, R. Freidenhans'l, M. Nielsen, F. Grey, and R. L. Johnson. 1991. Au/Si(111): Analysis of the ($\sqrt{3}$x$\sqrt{3}$)R30° and the 6x6 structures by in-plane x-ray diffraction. *Physical Review B* 44:11221-11231.

Dobrodey, N. V., L. I. Ziegelman, V. G. Zavodinsky, and I. A. Kuyanov. 1994. nonempirical cluster study of the Au adsorption on the Si(111) surface. *Surface Review and Letters* 1:273-284.

Doraiswamy, N. and L. D. Marks. 1995. Preferred structures in small particles. *Philosophical Magazine B* 71:291-310.

Duke, C.B. 1994. Principles of semiconductor surface reconstruction. *Scanning Microscopy* 8:753-764.

Dumas, Ph., A. Humbert, G. Mathieu, P. Mathiez, C. Mouttet, R. Rolland, F. Salvan, and F. Thibaudau. 1988. Summary abstract: Scanning tunneling microscopy studies on Au/Si(111) interfaces. *Journal of Vacuum Science and Technology A* 6:517-518.

Dunn, D. N., P. Xu, and L. D. Marks. 1992. Problems with use of surface reconstructions as indicators of a well-ordered surface. *Journal of Crystal Growth* 125:543-547.

_____. 1993. UHV transmission electron microscopy of Ir(001) I, Microstructure of the (1x1) and reconstructed (5x1) surfaces. *Surface Science* 294:308-321.

Durbin, S. M., L. E. Berman, B. W. Batterman, and J. M. Blakely. 1986. X-ray standing wave determination of surface structure: Au on Si(111). *Physical Review B* 33:4402-4405.

Endo, A. and S. Ino. 1993. Observations of the Au/Si(111) system with a high-resolution ultrahigh-vacuum scanning electron microscope. *Japanese Journal of Applied Physics* 32:4718-4725.

_____. 1996. Energy and angular distribution of secondary electrons emmitted from Si(111)-7x7, $\sqrt{3}$x$\sqrt{3}$ Ag, and 5x2-Au surfaces. *Surface Science* 34: 40-48.

Falta, J., A. Hille, D. Novikov, G. Materlik, L. Seehofer, G. Falkenberg, and R. L. Johnson. 1995. Domain wall structure of Si(111)($\sqrt{3}$x$\sqrt{3}$)R30°-Au. *Surface Science* 330:L673-L677.

Feenstra, R. M. and M. A. Lutz. 1990. Formation of the 5x5 reconstruction on cleaved Si(111) surfaces studied by scanning tunneling microscopy. *Physical Review B* 42:5391-5394.

_____. 1991. Kinetics of the Si(111)2x1 → 5x5 and 7x7 transformation studied by scanning tunneling microscopy. *Surface Science* 243:151-165.

Franklin, G. E, M. J. Bedzyk, J. C. Woicik, C. Liu, J. R. Patel, and J. A. Golovchenko. 1996. Order-to-disorder Phase Transition Study of Pb on Ge(111). *Physical Review B* 51:2440-2445.

Fuchigami K. and A. Ichimiya. 1996. Gold deposition on a Si(111)$\sqrt{3}$x$\sqrt{3}$-Au Surface. *Surface Science* in press.

Gabor, D. 1949. Microscopy by reconstructed wave-fronts. *Proceedings of the Royal Society A* 197:454-487.

Gibson, J. M., M. L. McDonald, and F. C. Unterwald. 1985. Direct imaging of a novel silicon surface reconstruction. *Physical Review Letters* 55:1765-1769.

Gibson, J. M. and M. Y. Lanzerotti. 1989. Silicon oxidation studied by in-situ TEM. *Ultramicroscopy* 31:29-35.

Goodman, P. and A. F. Moodie. 1974. Numerical evaluation of N-beam wave functions in electron scattering by the multislice method. *Acta Crystallographica A* 30:280-295.

Green, A. K. and E. Bauer. 1976. Formation, structure and orientation of gold silicide on gold surfaces. *Journal of Applied Physics* 47:1284-1291.

Hamers, R. J., U. K. Köhler, and J. E. Demuth. 1989. Nucleation and growth of epitaxial silicon on Si(001) and Si(111) surfaces by scanning tunneling microscopy. *Ultramicroscopy* 31:10-19.

Hana, Y. and K. Takayanagi. 1992. Single atom imaging in high-resolution UHV electron microscopy: Bi on Si(111) surface. *Ultramicroscopy* 45:95-101.

Hasegawa, S. and S. Ino. 1992. Surface structures and conductance at epitaxial growths of Ag and Au on the Si(111) surface. *Physical Review Letters* 68:1192-1195.

Hasegawa, S. and S. Ino. 1993. Correlation between atomic-scale structures and macroscopic electrical properties of metal covered Si(111) surfaces. *International Journal of Modern Physics B* 7:3817-3876.

Hasegawa, T., S. Hosaka, and S. Hosoki. 1992. In-situ observation of gold adsorption onto Si(111) 7x7 surface by scanning tunneling microscopy. *Japanese Journal of Applied Physics* 31: L1492-L1494.

_____. 1996. Domain growth of Si(111)-5x2 Au by high temperature STM. *Surface Science* in press.

Hasegawa, T., K. Takata, S. Hosaka, and S. Hosoki. 1990. Au-induced reconstructions of the Si(111) surface. *Journal of Vacuum Science and Technology A* 8:221-224.

_____. 1991. Initial stage of Au adsorption onto a Si(111) surface studied by scanning tunneling microscopy. *Journal of Vacuum Science and Technology B* 9:758-761.

Hazewindus, N. and J. Tooker. 1982. *The U.S. microelectronics industry: technical change, industrial growth and social impact.* New York: Pergamon Press.

Higashiyama, K., S. Kono, and T. Sagawa. 1986. Structural disorder of the Si(111)$\sqrt{3}$x$\sqrt{3}$-Au surface studied by LEED. *Japanese Journal of Applied Physics* 25:L117-L120.

Hiraki, A. 1984. Low temperature reactions at Si/metal interfaces: what is going on at the interfaces?. *Surface Science Reports* 3:357-412.

_____. 1986. Initial formation process of metal/silicon interfaces. *Surface Science* 168:74-99.

Hirsch, P., A. Howie, R. Nicholson, D. W. Pashley, and M. J. Whelan. 1977. *Electron microscopy of thin crystals.* 2nd rev. ed. Malabar, Florida: Robert E. Krieger.

Huang, J. H. and R. S. Williams. 1988a. Surface-structure analysis of Au overlayers on Si by impact-collision ion-scattering spectroscopy: $\sqrt{3}$x$\sqrt{3}$ and 6x6 Si(111)/Au. *Physical Review B* 38:4022-4033.

_____. 1988b. Surface structure of Si(111)-5x1-Au characterized by impact collision ion scattering spectroscopy. *Surface Science* 204:445-454.

Ichihashi, T. and S. Iijima. 1994. Surface structure of silicon observed by ultrahigh vacuum transmission electron microscopy at atomic level. *Proceedings of the 13th International Congress on Electron Microscopy* 2B:1013-1014.

Ichimiya, A., H. Nomura, Y. Ito, and H. Iwashige. 1995. Gold growth on Si(111)$\sqrt{3}$x$\sqrt{3}$ Ag and $\sqrt{3}$x$\sqrt{3}$ Au surfaces. *Journal of Crystal Growth* 150:1169-1174.

Ino, S. 1988. *Reflection high-energy electron diffraction and reflection electron imaging of surfaces.* Edited by P. K. Larson and P. J. Dobson. New York: Plenum.

Inoue, N., Y. Tanishiro, and K. Yagi. 1987. UHV-REM study of changes in the step structures on clean (100) silicon surfaces by annealing. *Japanese Journal of Applied Physics* 26:L293-295.

Itoh, M., H. Tanaka, Y. Watanabe, M. Udagawa, and I. Sumita. 1993. Classification and structure analyses of domain boundaries on Si(111). *Physical Review B* 47:2216-2227.

Jayaram, G., P. Xu, and L. D. Marks. 1993. Structure of Si(100)-(2x1) surface using UHV transmission electron diffraction. *Physical Review Letters* 71:3489-3492.

Jayaram, G. and L. D. Marks. 1995. Atomic structure of the Si(100)-(5x3)-Au surface. *Surface Review and Letters* 2:731-739.

Jia, J. F., R. G. Zhao, and W. S. Yang. 1993. Atomic structure of the Si(111)-($\sqrt{3}$x$\sqrt{3}$)R30°-Ag surface. *Physical Review B* 48:18109-18113.

Kambe, K. and G. Lehmpfuhl. 1975. Weak-beam technique for electron microscope observation of atomic steps on thin single-crystal surfaces. *Optik* 42:187-194.

Kamino, T., T. Yaguchi, M. Tomita, and H. Saka. 1996. In-situ HREM Study on a surface reconstruction of Au deposited Si at very high temperature. *Philosophical Magazine* in press.

Kasier, W. J. and L. D. Bell. 1988. Direct investigation of subsurface interface electronic structures by ballistic-electron-emission microscopy. *Physical Review Letters*. 60:1406-1410.

Karlsson, C. J., E. Landemark, L. S. O. Johansson, and R. I. G. Uhrberg. 1990. Experimental surface-state band structure of the Si(111)-($\sqrt{3}$x$\sqrt{3}$)-Au surface. *Physical Review B* 42:9546-9551.

Keating, P. N. 1966. Effect of invariance requirements on the elastic strain energy of crystals with application to the diamond structure. *Physical Review* 145:637-645.

Kimura, Y.and K. Takayanagi. 1992. Freezing of the 2x1 structure at commensurate Ag(100)-Si(100) interface. *Surface Science* 276:166-173.

Koch, R. 1994. The intrinsic stress of polycrystalline and epitaxial thin metal films. *Journal of Physical Condensed Matter* 6:95519-9550.

Koch, R., D. Winau, and K. H. Rieder. 1993. Intrinsic stress of epitaxial thin films. *Physica Scripta T* 49:539-543.

Koshikawa, T., T. Yasue, H. Tanaka, I. Sumata, and Y.Kido. 1995. Surface Structure of Cu/Si(111) at high temperature. *Surface Science* 331:506-510.

Kuwahara, Y., S. Nakatani, M. Takahasi, M. Aono, and T. Takahashi. 1994. X-ray diffraction study of Si(111)$\sqrt{3}$x$\sqrt{3}$-Au. *Surface Science* 310:226-230.

LaFemina, J. P. 1992. Total-energy calculations of semiconductor surface reconstructions. *Surface Science Reports* 16:133-260.

Lander, J. J. 1964. Chemisorption and ordered surface structures. *Surface Science* 1:125-164.

Latyshev A., H. Minoda, Y. Tanishiro, and K. Yagi. 1995. Ultra-high-vacuum reflection electron microscopy study of step-dislocation interaction on Si(111) surface. *Japanese Journal of Applied Physics* 34:5768-5773.

Lehmpfuhl, G. and Y. Uchida. 1979. Dark-field and bright-field techniques for electron microscopic observation of atomic steps on MgO single crystal surfaces. *Ultramicroscopy* 4; 275-287.

Lelay, G. 1981. The Au/Si(111) interface: growth mode, energetics, structural and electronic properties. *Journal of Crystal Growth* 54:551-557.

_____. 1983. Physics and electronics of the noble-metal / elemental-semiconductor interface formation: a status report. *Surface Science* 132:169-204.

Lelay, G. and J. P. Faurie. 1977. AES study of the very first stages of condensation of gold films on silicon (111) surfaces. *Surface Science* 69:295-300.

Lelay, G., M. Manneville, and R. Kern. 1977. Isothermal desorption spectroscopy for the study of two-dimensional condensed phases. *Surface Science* 65:261-276.

Lelay, G., V. Yu., T. Aristov, L. Seehofer, T. Buslaps, R. L. Johnson, M. Gothlied, M. Hammer, U. O. Kasson, S. A. Fodström, R. Feidenhans'l, M. Nielsen, E. Findeisen, and R. I. G. Uhrberg. 1994. STM and synchrotron radiation studies of "prototypical" metal/semiconductor systems. *Surface Science* 307:280-294.

Lin, X. F., K. J. Wan, J. C. Glueckstein, and J. Nogami. 1993. Gold-induced reconstructions of the Si(001) surface: the 5x5 and $\sqrt{26}$x3 phases. *Physical Review B* 47:3671-3676.

Lipson, H. and K. E. Singer. 1974. Disorder in a film of gold deposited on silicon: investigation by low-energy electron diffraction. *Journal of Physics C* 7:12-14.

Lupis, C. P. H. 1983. *Chemical Thermodynamics of Materials.* New York: North-Holland.

Ma, Y., S. Lordi, and J. A. Eades. 1994. Dynamic analysis of a RHEED pattern from the Si(111)-7x7 surface. *Surface Science* 313:317-334.

Marks, L. D. 1992. Registry and UHV transmission electron diffraction of surfaces. *Ultramicroscopy* 45:145-154.

_____. 1995. Mutual coherence treatment of HREM imaging. Northwestern University, Department of Material Science and Engineering, D65 class notes.

_____. 1996. Weiner-filter enhancement of noisy HREM images. *Ultramicroscopy* in press.

Marks, L. D., R. Ai, J. E. Bonevich, M. I. Buckett, D. Dunn, and J. P. Zhang. 1991. UHV microscopy of surfaces. *Ultramicroscopy* 37:90-102.

Marks, L. D. and R. Plass. 1994. Partially coherent and holographic contrast transfer theory. *Ultramicroscopy* 55:165-170.

_____. 1995. Atomic structure of Si(111)-(5x2) Au from high resolution electron microscopy and heavy-atom holography. *Physical Review Letters* 75:2172-2175.

Marks, L. D., R. Plass, and D. L. Dorset. 1996. Imaging surface structures by direct phasing. forthcoming.

Marks. L. D., T. S. Savage, J. P. Zhang, and R. Ai. 1991. Validity of the kinematical approximation in transmission electron diffraction from surfaces, revisited. *Ultramicroscopy* 38:343-347.

McComb, D. W., R. A. Wolkow, and P. A. Hackett. 1994. Defects on the Ag/Si(111)-($\sqrt{3}$x$\sqrt{3}$) surface. *Physical Review B* 50:18268-18274.

Meinel, K. and D. Katzer. 1992. Modes of growth of Au films on Si(111) and the mechanism of the silicide formation. *Applied Surface Science* 56:514-519.

Miki, K., Y. Morita, H. Tokumoto, T. Sato, M. Iwatsuki, M. Suzuki, and T. Fukuda. 1992. Real-time observation of the Si(111):(7x7)-(1x1) phase transition by scanning tunneling microscopy. *Ultramicroscopy* 42:851-857.

Milnes, A. G. 1973. *Deep Impurities in Semiconductors.* New York: Wiley.

Minoda, H., Y. Tanishiro, N. Yamamoto, and K. Yagi. 1992. Growth of Si on Au deposited Si(111) surfaces studied by UHV-REM. *Applied Surface Science* 60:107-111.

Mollenstedt, G. and H. Duker. 1954. Fresnelscher interferzversuch mit einem biprisma fur elektronenwellen. *Naturwissenschaften* 42:41.

Morooka, M., M. Takahashi, and F. Hasimoto. 1992. Stacking fault induced by gold diffusion in silicon. *Japanese Journal of Applied Physics* 31:2327-2332.

Morris, P. R. 1990. *A history of the world semiconductor industry.* London: Peter Peregrinus Ltd.

Mouttet, C. 1981. Electronic structure of the Si-Au surface. *Surface Science Letters* 111:L755-L758.

Murarka, S. P. and S. W. Hymes. 1995. Copper Metallization for ULSI and beyond. *Critical Reviews in Solid State and Materials Sciences* 20:87-124.

Nakayama, T., S. Watanabe, and M. Aono. 1995. Structure and stability of the out-of-phase boundary in a surface superlattice, Si(111)$\sqrt{3}$x$\sqrt{3}$R30°-Ag. *Surface Science* 344:143-148.

Nihoul, G., K. Abdelmoula, and J. J. Metois. 1984. High-resolution images of a reconstructed surface structure on (111) gold platelets: interpretation and comparison with theoretical models. *Ultramicroscopy* 12:353-359.

Nogami, J., A. A. Baski, and C. F. Quate. 1990. $\sqrt{3}$x$\sqrt{3} \rightarrow$ 6x6 phase transition on the Au/Si(111) surface. *Physical Review Letters* 65:1611-1614.

Northrup, J.E. and M.L. Cohen. 1982. Reconstruction mechanism and surface state dispersion for Si(111)-(2x1). *Physical Review Letters* 49:1349-1353.

Ohnishi, H., K. Itsuo, Y. Ohba and K. Oura. 1994. Scanning Tunneling Microscope Observation of Si(111)-3x1-Ag structure. *Japanese Journal of Applies Physics* 33:3683-3687.

O'Mahony, J. D., J. F. McGilp, C. F. J. Flipse, P. Weightman, and F. M. Leibsle. 1994. Nucleation and evolution of the Au-induced 5x2 structure on vicinal Si(111). *Physical Review B* 49:2527-2535.

O'Mahony, J. D., C. H. Patterson, J. F. McGilp, F. M. Leibsle, P. Weightman, and C. F. J. Flipse. 1992. The Au-induced 5x2 reconstruction on Si(111). *Surface Science Letters* 277:L57-L62.

Osakabe, N., Y. Tanishiro, K. Yagi, and G. Honjo. 1980. Reflection electron microscopy of clean and gold deposited (111) silicon surfaces. *Surface Science* 97:393-408.

Oura, K., M. Katyama, J. Shoju, and T. Hanawa. 1985. Real-space determination of atomic structure of the Si(111)-$\sqrt{3}$x$\sqrt{3}$ R30°-Au surface by low-energy alkali-ion scattering. *Physical Review Letters* 55:1486-1489.

Pandey, K. C. 1981. New π-bonded chain model for the Si(111)-(2x1) surface. *Physical Review Letters* 47:1913-1917.

Parikh, S. A., M. Y. Lee, and P. A. Bennett. 1995. Transition metal induced ring-cluster structures on Si(111). *Journal of Vacuum Science and Technology A* 13:1589-1594.

Plass, R. and L. D. Marks. 1995. UHV transmission electron microscopy structure determination of the Si(111)-($\sqrt{3}$x$\sqrt{3}$)R30°Au surface. *Surface Science* 342:233-249.

_____. 1996. Room temperature deposition of gold onto the diffuse and sharp diffraction spot Si(111)-($\sqrt{3}$x$\sqrt{3}$)R30° Au surfaces. *Surface Science* in press.

Plass, R., L. D. Marks, and D. L. Dorset. 1996. Adsorption site of Au on the Si(111)-($\sqrt{3}$x$\sqrt{3}$)R30° Au surface. forthcoming.

Qian, G. X. and D. J. Chadi. 1987. Si(111)-7x7 surface: energy-minimization calculation for the dimer-adatom-stacking-fault model. *Physical Review B* 35:1288-1293.

Quinn, J., F. Jona, and P. M. Marcus. 1992. Atomic structure of Si{111}($\sqrt{3}$x$\sqrt{3}$)R30°-Au. *Physical Review B* 46:7288-7291.

Robinson I. K., W. K. Waskiewicz, P. H. Fuoss, and L. J. Norton. 1988. Observation of strain in the 7x7 surface. *Physical Review B* 37:4325-4328.

Salvan, F., H. Fuchs, A. Baratoff, and G. Binning. 1985. Au/Si(111) overlayer: characterization by tunneling microscopy and spectroscopy. *Surface Science* 162:634-639.

Saxton, W. O. 1994. Accurate alignment of sets of images. *Journal of Microscopy* 174:61-68.

Sayer, D. 1952. The squaring method: a new method for phase determination. *Acta Crystallographica* 5:60-65.

Self, P. and M. A. O'Keefe. 1988. *High-resolution transmission electron microscopy.* Edited by P. Busek, J. Cowely, and L. Eyring. Oxford: Oxford University Press.

Schamper, Ch., W. Moritz, H. Schluz, R. Feidenhans'l, M. Nielsen, F. Grey, and R. L. Johnson. 1991. Static lattice distortions and the structure of Au/Si(111)-(5x1): an X-ray diffraction study. *Physical Review B* 43:12130-12133.

Schell-Sorodin, A. J. and R. M. Tromp. 1990. Mechanical stresses in (sub)monolayer epitaxial films. *Physical Review Letters* 64:1039-1042.

Schwartz, L. H. and J. B. Cohen. 1987. *Diffraction from Materials*. 2nd ed. Berlin: Springer-Verlag.

Seehofer, L., S. Huhs, G. Falkenberg, and R. L. Johnson. 1995. Gold-induced faceting of Si(111). *Surface Science* 329:157-166.

Shibata, A., Y. Kimura, and K. Takayanagi. 1992. Si(111)$\sqrt{3}$x$\sqrt{3}$-Au growing on a 7x7 surface. *Surface Science Letters* 273:L430-L434.

Spence, J. C. 1983. High-energy transmission electron diffraction and imaging studies of the silicon (111) 7x7 surface structure. *Ultramicroscopy* 11:117-123.

_____. 1988. *Experimental high-resolution electron microscopy*. Oxford: Oxford University Press.

Srolovitz, D. G. and S. A. Safran. 1986. Capillary instabilities in thin films. II. kinetics. *Journal of Applied Physics* 60:255-267.

Struthers, J. D. 1956. Solubility and diffusivity of gold, iron, and copper in silicon. *Journal of Applied Physics* 27:1560.

Suzuki, T., H. Minoda, Y. Tanishiro, K. Yagi, H. Kitada, and N. Shimizu. 1996. STM studies of Si(hhm) surfaces with m/h=1.4-1.5. forthcoming.

Sweich, W., E. Bauer, and M. Mundschau. 1991. A low-energy electron microscopy study of the system Si(111)-Au. *Surface Science* 253:283-296.

Takahashi, S., Y. Tanishiro, and K. Takayanagi. 1991. Short range orders of an adsorbed layer: gold on the Si(111)7x7 surface. *Surface Science* 242:73-80.

Takahashi, T. and S. Nakatani. 1993. Refinement of the Si(111)$\sqrt{3}$x$\sqrt{3}$-Ag structure by surface X-ray diffraction. *Surface Science* 282:17-32.

Takahashi, T., S. Nakatani, N. Okamoto, T. Ishikawa and S. Kikuta. 1991. A study of the Si(111)$\sqrt{3}$x$\sqrt{3}$-Ag surface by transmission X-ray diffraction and X-ray diffraction topography. *Surface Science* 242:54-58.

Takami, T., D. Fukushi, T. Nakayama, M. Uda, and M. Aono. 1994. Structural correlation among different phases in the initial stage of epitaxial growth of Au on Si(111). *Japanese Journal of Applied Physics* 33:3688-3695.

Takayanagi, K., Y. Tanishiro, S. Takahashi, and M. Takahashi. 1985. Structure analysis of Si(111)-7x7 reconstructed surface by transmission electron diffraction. *Surface Science* 164:367-392.

Tanaka, H., M. Udagawa, M. Itoh, T. Uchiyama, Y. Watanabe, T. Yokotsuka, and I. Sumita. 1992. Si(111) 7x7 domain boundaries on vicinal surfaces. *Ultramicroscopy* 42:864-870.

Tanishiro, Y. and K. Takayanagi. 1989a. Validity of the kinematical approximation in transmission electron diffraction for the analysis of surface structures. *Ultramicroscopy* 27:1-8.

_____. 1989b. Dynamic observation of gold adsorption on Si(111) 7x7 surface by high-resolution reflection electron microscopy. *Ultramicroscopy* 31:20-28.

Telieps, W. and E. Bauer. 1985. An analytical reflection and emission UHV surface electron microscope. *Ultramicroscopy*. 17:57-65.

Tonomura, A., T. Matsuda, J. Endo, H. Todokoro, and T. Komoda. 1979. Development of a field emission electron microscope. *Journal of Electron Microscopy* 28:1-11.

Tsaur, B. Y. and J. W. Mayer. 1981. Metastable Au-Si alloy formation induced by ion-beam interface mixing. *Philosophical Magazine A* 43:345-361.

Twesten, R. D. and J. M. Gibson. 1995. Kinematic analysis of transmission electron diffraction data from Si(111)-7x7. *Ultramicroscopy* 53:223-235.

Valentine. P. 1995. Electronics, basic analysis. *Standard and Poor's industry surveys.* 163:E1-E32.

Van Hove, M. A., W. Moritz, H. Over, P. J. Rous, A. Wander, A. Barieri, N. Materer, U. Starke, and G. A. Somorjai. 1993. Automated determination of complex surface structures by LEED. *Surface Science Reports* 19:191-229.

Vanderbilt D. 1987a. Absence of Large Compressive Stress on Si(111). *Physical Review Letters* 59:1456-1459.

_____. 1987b. Model for the energetics of Si and Ge (111) surfaces. *Physical Review B* 36:6209-6212.

Venables, J. A., G. D. T. Spiller, and M. Hanbucken. 1984. Nucleation and Growth of Thin Films. *Report of Progress in Physics* 47:400-459.

Wan, K. J., X. F. Lin, and J. Nogami. 1993. Surface Reconstructions in the Ag/Si(111) system. *Physical Review B* 47:13700-13712.

Weisbuch, C. 1991. *Quantum Semiconductor Structures: Fundamentals and Applications.* Boston: Academic Press.

Wiener, N. 1942. *Extrapolation, Interpolation, and Smoothing of Stationary Time Series.* Cambridge, Massachusetts: MIT Press.

Wilk, G. D., R. E. Martinez, J. F. Chervinsky, F. Spaepen, and J. A. Golovchenko. 1994. Low-temperature homoepitaxial growth on Si(111) mediated by thin overlayers of Au. *Applied Physics Letters* 65:866-868.

Woolfson, M. M. 1987. Direct methods - from birth to maturity. *Acta Crystallographica A* 43:593-612.

Wong, H., M. J. Miksis, P. W. Voorhees, and S. H. Davis. 1996. forthcoming.

Wong-Leung, J., J. S. Williams, R. G. Elliman, E. Nygren, D. L. Eaglesham, D. C. Jacobson, and J. M. Poate. 1995. Proximity gettering of Au to ion beam induced defects in silicon. *Nuclear Instruments and Methods in Physics Research B* 96:253-256.

Xu, P., D. Dunn, J. P. Zhang, and L. D. Marks. 1993. Atomic imaging of surfaces in plan view. *Surface Science Letters* 285:L479-L485.

Xu, P., G. Jayaram, and L. D. Marks. 1994. Cross-correlation method for intensity measurement of transmission electron diffraction patterns. *Ultramicroscopy Letters* 53:15-18.

Xu, P. and L. D. Marks. 1992. Intensity of surface diffraction spots in plan view. *Ultramicroscopy* 45:155-157.

Yabuuchi, Y., F. Shoji, K. Oura, and T. Hanawa. 1983. Surface structure of the Si(111)-5x1-Au studied by low-energy ion scattering spectroscopy. *Surface Science Letters* 131:L412-L415.

Yagi, Y., K. Kakitani, and A. Yoshimori. 1996. Correlation function of adsorbed Au chain on Si(111) surface. *Surface Science* in press.

Yang, Y. N. and E. D. Williams. 1994a. High atom density in the "1x1" phase and origin of the metastable reconstructions on Si(111). *Physical Review Letters* 72:1862-1865.

_____. 1994b. Metastable Reconstructions on Si(111). *Scanning Microscopy* 8:781-794.

Yeh, J. J., J. Hwang, K. Bertness, D. J. Friedman, R. Cao, and I. Lindau. 1993. Growth of the room temperature of Au/Si(111)-(7x7) interface. *Physical Review Letters* 70:3768-3771.

Yuhara J., M. Inoue, and K. Morita. 1992a. Phase transition of the Si(111)-Au surface from $\sqrt{3}$x$\sqrt{3}$ to 5x1 structure studied by means of the low-energy electron diffraction, Auger electron spectroscopy, and Rutherford backscattering spectroscopy techniques. *Journal of Vacuum Science and Technology A* 10:334-338.

_____. 1992b. Commensurate-incommensurate phase transition between 6x6 and $\sqrt{3}$x$\sqrt{3}$ + satellite structures of the Au/Si(111) surface. *Journal of Vacuum Science and Technology A* 10:3486-3492.

Zangwill, A. 1988. *Physics at Surfaces*. Cambridge: Cambridge University Press.

# APPENDIX A MURPHY WAS RIGHT CONTINUED

# (What John Didn't Mention)

Speaking as someone who has had a few run-ins with Murphy while maintaining empty steel and glass boxes, I have a few comments to add to the John Bonevich list of ultrahigh vacuum do's and don'ts.

## A.1 General UHV Suggestions

Don't spray Dust Off into or anywhere near a UHV chamber unless you want to study fluorine. If you do manage this feat (you wouldn't be the first), the quickest way to get rid of it is with an oxygen plasma, be sure to outgas EVERYTHING properly ($F_2$ gets into everything and sticks there).

Although Laurie seems to be getting less concerned about people wrapping the objective aperture around the pole piece, DON'T GANESH THE MICROSCOPE! Stay awake before, during, and after moving the cartridge. DO THE CHECKLIST EVERY TIME.

To put an old rule into writing: if you really FEEL too tired to use the system, you ARE too tired to use the system, go home and get some sleep. Dropping the sample or damaging something will DEFINITELY make you miss your deadline.

Power failures are a pain in the neck.

Floods are an even bigger pain in the neck.

## A.2 Bakeout Suggestions

Why bother trying to push the base pressure down when mid $1x10^{-10}$ Torr pressures seem good enough? The base pressure, in itself, isn't important (mostly hydrogen and argon in a clean system usually) the partial pressures of water, hydrocarbons, and the like, that come off the walls during various operations such as sample heating and metal evaporation are what are important. Pushing the base pressure down helps ensure that the system will stay at least in the high tens during these operations by minimizing the water and hydrocarbons on the walls.

In terms of general bakeout philosophy, it is more important to eliminate all cold spots than to get parts of the system superhot. What determines your final pressure (aside from leaks) is the presence or absence of cold spots, although higher temperatures crack water and hydrocarbons more efficiently. After an overhaul, always leak check before a bake. Now some components such as closed gate valves have definite temperature limits so use a bakeout log to monitor the initial stages of the bake and to track from one bake to the next heater tape voltages applied versus temperatures achieved versus the final pressures obtained. In addition to critical components this log should also track general chamber temperatures and the ion gauge and ion pump readings of the different chambers. (A discrepancy in the movement of these two pressure readings is usually the first sign a big leak has opened up, opened large flanges often "walk" during their first bake and will need retightening.) Track these different values with time in horizontal log entries until the bake temperatures have stabilized and the pressures have started falling, usually check temperatures and

pressures once every half hour for four to eight hours. If a component is within 10°F or so of its temperature limit, lower its heating (lower the applied voltage or remove some aluminum foil). If it seems too cold, heat it more. Besides the critical components also check different locations around the chamber once the temperature is stable to look for cold spots. Heaters sometimes break in the initial heatups leading to big cold spots. Depending on the operating temperature limit of the residual gas analyzer (RGA) it is often very instructive to partially shut off the bake around the RGA, enough to allow it to operate, then actually look at what is coming off the walls.

### A.3 How to Read a Residual Gas Analyzer / Leak Checking

If you have only one RGA it should be installed in the chamber where you expect the most trouble since the analyzer is most sensitive to the chamber it is in. NOTE, most RGAs (radio frequency quadropole mass spectrometers) need periodic tuning and calibration in the high and low mass ranges for optimum sensitivity. You will get nowhere with an out of tune RGA.

A really big leak, a hisser, won't allow the RGA or the ion pumps to come on. After a big overhaul, check all the opened flanges since some KLUTZ probably didn't tighten a flange properly, or forgot to. If that isn't it use the cheap stethoscope test, a tube in the ear, but remember that a welded bellows will always sound like it is leaking. Alternatively, come to air and swap out suspicious new components (whenever possible check the vacuum integrity of new components BEFORE putting them on the main system).

A big leak ($10^{-6}$ to $10^{-9}$ Torr) is characterized in the RGA mass spectrum by a dominant 28 mass nitrogen peak which grows linearly if all the chamber pumping is shut off. The presence of the 32 oxygen peak is not to be expected ($O_2$ can react before reaching the RGA) but if present, it confirms the presence of the leak.

Judging the presence of a small leak ($10^{-10}$ to $10^{-11}$), especially in a dirty chamber, is where life gets interesting since $N_2$ and CO can both cause the 28 peak. Watching for a linear increase in this peak is now useless since the walls can be outgassing CO as fast a small leak introduces $N_2$. In this case watch the 14, 15, and 16 peaks carefully. If 14 slowly increases above 15 and 16 with reduced or no pumping then its a leak ($N_2$ cracking in the RGA). If 15 and 16 (carbon peaks) stay ahead of 14 its time to bake. Another, less reliable, way to distinguish CO from $N_2$ is that CO will have isotope satellite peaks on either side while $N_2$ has a very sharp peak.

Actually finding the leak is done by setting the RGA to continuously scan the 3, 4, and 5 peaks while injecting a slow helium flow into every nook and cranny of the chamber. I start the check with recently opened flanges, old leaks, and perennial trouble spots, then large flanges, all other flanges, (including gate valve bonnets), bagged mechanical (including gate valves) and electrical feedthroughs (bagging means covering the part with a glove, etc..., sealing with electric tape and filling with He), and finally window seals and chamber welds. Be on guard for a virtual leak, a pocket of air trapped in a line "sealed off" by a valve but slowly leaking through the valve's gasket, or a pocket of air trapped in a newly added component.

Once a leak is found, if its from a flange, the flange is tightened. If the flange is already steel to steel or if the leak is some where else its best to replace the gasket or the part, respectively. Vac-seal, a high vacuum sealing compound, is a good alternative. It works best for smaller leaks up to about $10^{-8}$ Torr but it is tough to clean off once baked.

Leak checking is an art, I recommend that with a rising nitrogen spectrum, if a relatively quick check for big leaks fails, it is better to carefully watch the nitrogen peak increase under various pumping configurations and think about the results. This often allows you to localize where the leak is first, which is better than just blasting He at the chamber arbitrarily.

The water mass peak, 18, is usually the dominant peak of a leak tight unbaked chamber. If it is still the dominant peak after the bake then something in the chamber was below 100°C during the bake and the bake should be repeated fixing the cold spot.

Lots of higher mass peaks, sort of forming hills and valleys, most visible when the chamber is still hot are usually from some type of oil, either hand oil (a new Varian gate valve was filthy internally), or backstreamed roughing pump oil. Oil can only be removed by prolonged baking or baking cycles under clean (ion pumping only) pumping conditions. It is better to cycle a bake on and off, with outgassing of major components on the cooldowns, rather than to bake forever since the cool downs allow the areas with limited conductance to outgas into the main chamber.

## A.4 Suggestions in doing the SPEAR Dance

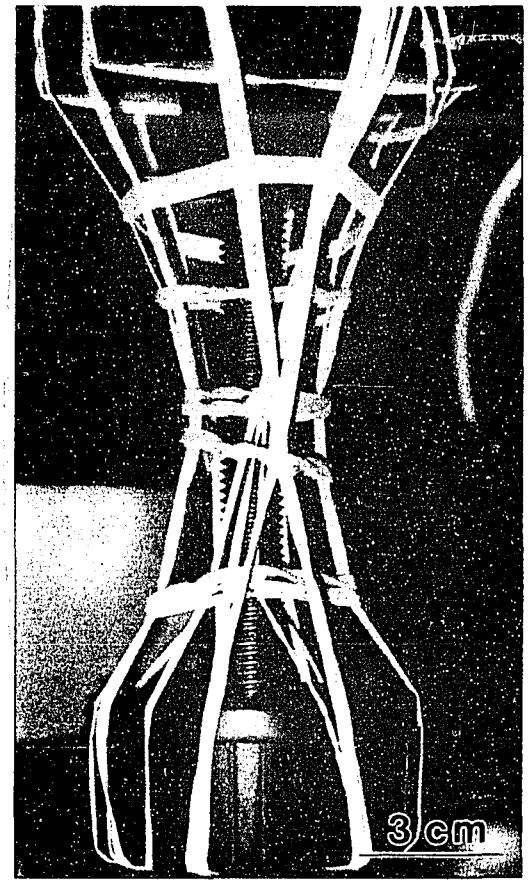


Figure A.1. Doing UHV-HREM sometimes requires unique solutions: rubber bands on its handle stabilize an open gate valve.

In moving the elevator gripper up and down, don't open the gripper if a sample is in it. If the transfer boom's mechanical feedthrough gets stiff the boom will shake up and down if extended or retracted quickly, and thus send samples flying. Patience is needed in moving bulk samples anywhere, thin areas cleave away nicely with impatient behavior.

When you put a sample ring into a microscope cartridge, close the elevator gripper and gently press it against the top of the ring to ensure that it is flat against the bottom of the block or resolution may suffer. Remember to open the gripper again.

If someone complains excessively about SPEAR sample transfers their punishment should be to reseal and rough evacuate the Museum of UHV Microscopy (the old side chamber) with the two rods in place and a cartridge on one rod. Then, using John's gripper, he or she should get the cartridge from one rod to the other and back again unassisted.

# APPENDIX B EVAPORATOR SYSTEM DESIGN

Building and installing reliable, controllable evaporators and thickness monitors into the UHV-TEM (Figure 2.6) was one of the key factors in collecting the data presented and will be vital in future studies as well.

## B.1 General Maintenance Points

Remember these cone type evaporators weren't easy to build (i.e., won't be easy to replace) and tungsten is very brittle once fired. Therefore use extreme care when removing, loading more metal into, and reinstalling the evaporators. (Yes, you can get the microscope evaporator and crystal monitor out without breaking the column. It just takes some gentle maneuvering, use plenty of light to see what you are doing. Breaking the column will not make the extraction process any easier).

If a vital evaporator does break, take the thing apart completely and rebuilt it with new evaporators. You can't "repair" an evaporator element reliably.

It may seem obvious, but all evaporators are designed to be refilled with the same metal, keep track of which metal was in which evaporator unless you want arbitrary alloys.

Do not try to adjust the locations of evaporators by bending the filaments, they will break. Rather build a new evaporator with the desired changes on another electrical feedthrough while keeping the original evaporator intact.

## B.2 Evaporator Design Philosophy

In designing any type of UHV component follow the three Russian design rules: make it simple, make it strong, make it work. Also try to make your parts redundant and easy to remove and reinstall while always following the UHV material selection rules. Zinc in a chamber is not pretty.

Forget about using molybdenum (moly) boats for typical UHV work, they are too difficult to control for submonolayer depositions. The moly cone and tungsten filament combination is the best evaporator design for our work since it has the controllability of a tungsten loop filament and most of the metal capacity of a boat. Its only drawback is that loaded metal may sometimes not easily reach the tip of the cone. If this occurs the required short, high current spike to "refresh" the evaporator could either burn out the filament or suddenly deposit too much metal.

Always, always, always test a new evaporation metal / evaporator material combination in a regular evaporator system such as our Denton first, before proceeding to build a full evaporator assembly. As examples: aluminum and moly make an alloyed gooey mess when heated in the presence of each other, thin tungsten filaments will burn out long before you deposit any nickel with them. These are very unpleasant surprises if first discovered in a UHV chamber just before an experiment.

Given the limited space involved in getting something through a 2 and 3/4" flange, design the cross deposition shields between the evaporators carefully. During a bake and especially during first firing the wires will tend to bend, sag, or otherwise move around. Therefore make sure the shields are firmly mounted and all wire

connections are tightly fixed to prevent shorting or blockage of the deposition paths.

Lastly, do not design evaporators to be too complex. These things may look stable and easy to make once the metal has run into the cone tips. What is not obvious is that when a new evaporator is installed, the moly cone is just caught between the tungsten elements, which is a very rickety assembly. The metal fuses these elements together in the outgassing / first firing step after the bake. If you think you can first carry out this fusing process in the Denton evaporator then assemble the rest, do not bother, the tungsten becomes too brittle to work with.

## B.3 Using the Thickness Monitor

Never disconnect or connect the crystal cables with the crystal monitor power on, you can easily blow the sensitive comparators in the first stage amplifier circuits.

The coax jack near the crystal inputs is an audio output that directly taps the signal feeding the internal frequency counter. This is the signal that is connected to the audio input of a VCR during deposition experiments. It can also be used with a frequency counter for more accurate measures of the beat frequency. If the internal frequency counter reads 0 use a frequency counter to check the signal from this line before servicing, sometimes the amplifiers aren't strong enough to drive the internal counter.

# APPENDIX C HOW TO MAKE A BIPRISM FILAMENT

Very thin gold coated quartz filaments are needed to assemble a Mollenstedt (Mollenstedt and Duker 1954) type electron biprism which, along with a bright coherent electron source, are required to do electron holography. The thinner (preferably less than 400 nm in diameter) and tauter (for stability and long life) this filament is, the better.

## C.1 Initial steps

Become good friends with the Chemistry Department glassblower.

Don't drink coffee or any other caffeinated beverage for a month before starting. Seriously, you may want to practice to get steady hands.

Equipment needed, glass shop:

-$H_2$ and $O_2$ Tanks

-Medium to large torch

-High purity quartz rod, about 1/4" thick

-6 to 8 catchers (Figure C.1), adhesive coating on the tines

-Compartmented plastic carrier for the catchers

Equipment needed, Darkroom:

-Slit light source: florescent shop lamp in its original box with a long (as

narrow as possible) slit running down the length of the box over one bulb (remove the other bulb). Put black paper on the top of the light box just next to the slit to minimize light scattering.

-Appropriate filament mounts for the biprism assembly (from the microscope manufacturer).

-Transparent, short "table" made from a 15"x15" piece of plexiglass with 4" long legs (tall enough to clear the slit light source). (Try to minimize the scratches to the plexiglass).

-Piece of 14 gauge Cu wire with an alligator clip attached to one end and bent to act as a holder for the filament mounts (Figure C.1).

-10x magnifier with the lower recticle holding portion removed so that the magnifier can be brought close to objects.

-Reasonably fresh and fluid Silver Dag, or comparable conductive mounting paint.

## C.2 Glass blowing procedure

Just before starting put spray adhesive on the catcher tines. If the filaments don't seem to be sticking put more adhesive on.

Set up a $H_2$ jet flame, blue-white hot, about 2 to 2.5" in diameter (as wide as the mouth of the torch), and about 6" long. It will be making quite a roar and heating the room nicely. ($H_2$ is used instead of acetylene to minimize filament carbon residue).

Grabbing the end of the rod with the tongs, heat the quartz in the center of the

flame and pull it to thin it slowly. Best results were obtained by pulling the two ends of the rod apart moderately sharply just as the rod becomes too thin to see in the flame. The jet drives the resulting two thin quartz filaments or "streamers" (6" to 12" in length) into the air.

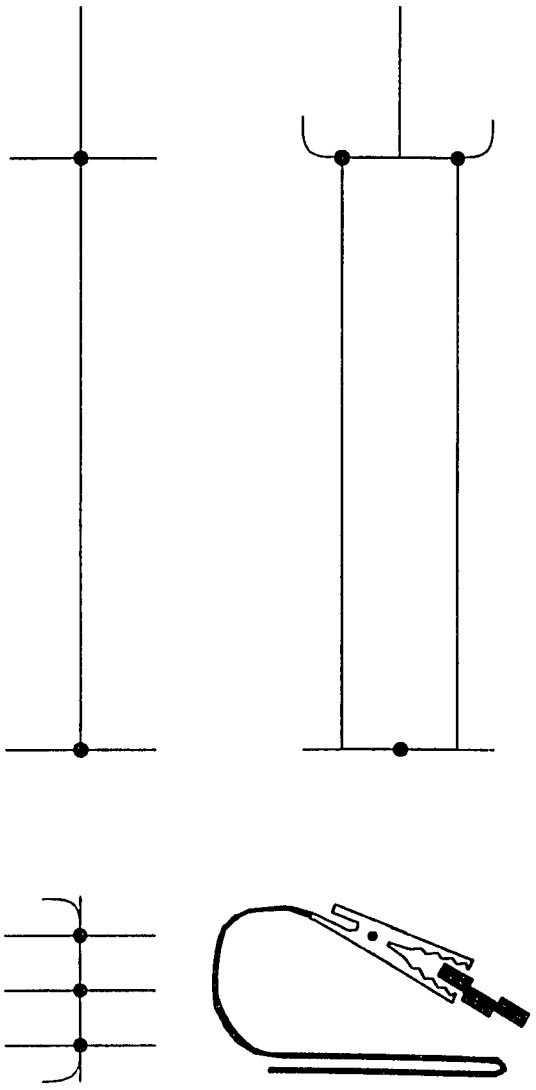

Figure C.1. Top, front, and side view schematics of a biprism filament catcher which is, overall, about 22 cm long, 4 to 5 cm wide. To the lower right is a side view schematic of a filament mount holder with a mount in its jaws.

Keep a sharp eye on the thinner part of the streamer, it is easy to loose track of (minimize air turbulence). With some of the lights off, slowly pull the thick end of the streamer through the air horizontally (easier to see that way, hold the streamer parallel to lights and look down its length). Try to spot where the streamer becomes invisible. "Flying the kite" with one hand and with a catcher in the other hand pull the thinnest section of the streamer you can see over and against a tine of the catcher so the invisible part of the streamer catches the other tine. Then wrap the thicker portion of the streamer around the tines a few times and carefully try to snap it off. If it does not snap off readily, cut

it, quartz can be surprisingly tough.

Make and catch at least as many filaments as you have catchers. You can usually get two filaments per catcher. Do not try to get more that two filaments on a catcher; you will not have enough room to maneuver the mount holder later. If no part of a caught streamer looks thin (i.e., part of the streamer seems to trail off to nothing with the visible part caught in mid air) clean that streamer off and start over. You need lot of filaments because some won't be thin enough. But mainly you will need plenty of filaments because (just like bulk sample prep.) you will end up breaking most them in the next step unless you have a lot of practice.

## C.3 Mounting Procedure

(Practice this procedure several times with thicker filament portions to get the feel of it before trying to mount a usable filament.)

Get a good night's sleep and calm your mind.

As with all vacuum parts thoroughly clean the filament mounts in ultrasonic baths of acetone and methanol, dry with a heat gun, after which handle them only with gloves.

Set up the slit light source with the clear table over it in a darkroom. Wear a disposable mask to deflect your breath. For safety, do not leave the light on too long or it could set the box on fire (a cooling fan causes too much air turbulence). Place a loaded catcher on the clear table and using the "sawed off" magnifier examine the filaments on the catcher. They are seen most clearly when the filament of interest is

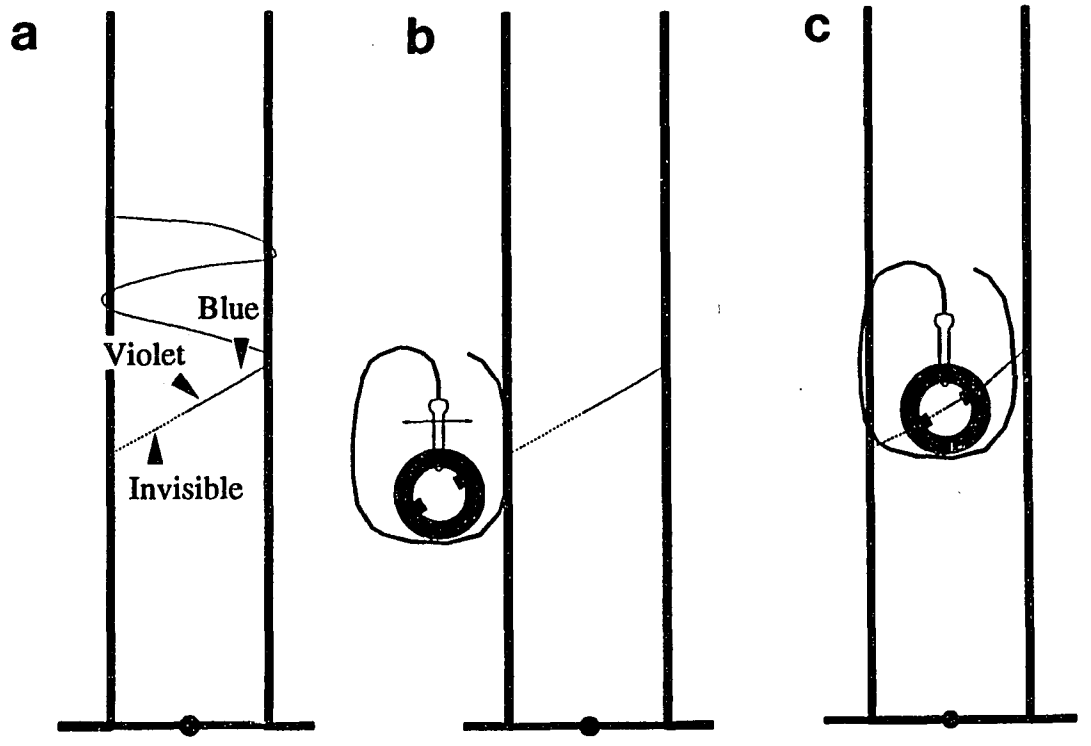


Figure C.2. Top view illustrations of a) the front of a catcher with a filament around it, b) the same catcher with the thicker portions of the filament cut away and the filament mount / mount holder positioned for mount height adjustment, and c) the final position just before application of the Silver Dag.

parallel to the light slit, directly over it, and you angle the magnifier about 30° away from the illumination plane. In the darkroom there is much less background light around so you should be able to see farther along the thinnest filaments than in regular lighting. You should also see a rainbow effect from the scattering of the filament (Figure C.2a), this will tell you how thick a section is. Only the blue to purple to invisible portions of a filament are worth mounting, with a sharp scissors carefully cut away all thicker filament sections to clear room for the mount and mount holder.

The first step in mounting the filament is to align the mount in the alligator clip jaws to be parallel to the filament. Keeping the alligator clip body parallel to the

catcher tines grab the circular mount in the clip so that the mount tabs run exactly parallel to the filament. Check to make sure the base of the mount holder does not wobble. Adjust the wire behind the alligator clip so that the mount is inclined 20° to 30° from horizontal and that the points where you want the filament to run over the mount are at EXACTLY the same height as the filament in the catcher. This will also mean twisting the alligator clip about its axis a bit to get the two sides of the mount to the EXACT same height. This step is THE most critical! With a properly set height mounting will be relatively easy, without it you will end up with a badly off center filament or (more likely) a broken filament. (The filament needs to be very close to the center of the mount or the image of the filament will move a lot as the biprism is rotated. Worse the filament may be well out of microscope's beam path.) One trick in getting the mount's height right is to put the mount holder next to the catcher so that the mount is aligned with the filament (Figure C.2b) and then sight along the filament from either direction to be sure the height is correct. It is better to fiddle with the mount holder for half an hour to get this step right than to go on incorrectly.

Once you are satisfied with the height, position the mount holder so that the center axis of the mount is illuminated by the slit. Place the catcher over the mount well away from the filament so the mount is between the tines and start slowly pushing the filament towards the mount. In the "final approach" move the filament straight at the mount. If you try to slide the filament over the mount it will get snagged on an edge and break. You will know that the filament is touching the mount when there is a slight angle between the portion of the filament over the center of the

mount and the portion from the mount to the catcher tine. If the filament touches the mount too far away from the mount's center axis slowly back the catcher away from the mount holder and lift it clear, then readjust the mount holder. Don't try to adjust the mount's height with the filament nearby.

Once the filament is touching the mount at the correct height you need to push the catcher slightly farther to put some tension on the filament. This is where experience, practice, nerves of steel, and a steady hand come in. You want things to look something like Figure C.2c. Ideally the filament is pulled taut against the center axis of the mount with as much of the invisible portion of the filament in the mount's center region as possible. (You must leave enough clearance between the mount and either tine to get a scissors in.) How much tension you put on the filament depends on how much filament slack there was initially and how thin you feel the wire is. Quartz is surprisingly tough, therefore I would tend to err on the side of pushing too far since you can only tell that a mounted wire isn't taut enough in the SEM or worse, finally mounted in the TEM.

After applying tension, if the filament is still intact, then congratulations: the worst part is over. Inspect the situation with the magnifier to check that the filament is touching both sides of the mount. This may be tricky for the invisible side, you have to extrapolate from the visible portion. Shake the silver dag well and get a small droplet on the brush (or toothpick). LIGHTLY touch the brush against one side of the mount just above the filament, allowing the silver dag to run down and wet the filament. Don't apply too much silver dag, it can interfere with assembling the

biprism later and would then have to be scraped off, likely breaking the filament. Do the same on the other side, then GO AWAY... Get something to drink, snap your neck back into place, etc...; but stay away long enough to let the silver dag dry COMPLETELY. You are almost done, don't mess things up by fiddling around with it now.

Once the silver dag is fully dry use scissors to cut the filament free from the catcher; ripping the filament free can break the center portion. The filament is now ready for gold coating (just enough to make it conductive, the amount needed varies). Subsequent inspection in a high resolution SEM is highly recommended before mounting in the TEM biprism. Once on its mount the filament is fairly robust as long as nothing touches it directly.

### C.4 Final tips

Try to minimize the amount of time a filament is outside of a closed container. This minimizes the amount of dust that adheres to the filament, especially in the steps before gold coating. Don't wave filaments in the air more than needed.

To steady your hand, brace the heel of your hand against the clear table or something solid as you move parts or hold the silver dag brush.

Above all, BE VERY PATIENT! Go slow when you need to, this procedure isn't easy.